Università degli Studi di Genova

SCUOLA DI SCIENZE MATEMATICHE, FISICHE E NATURALI

DIPARTIMENTO DI FISICA

Corso di Laurea Magistrale in Fisica

Tesi di Laurea Magistrale

Drag Reduction Over Rough Permeable Surfaces: A Homogenized-Based Approach

Relatori:
Prof. Alessandro Bottaro
Prof. Andrea Mazzino

Correlatore:
Prof. Corrado Boragno

Candidato:
Lorenzo Buda

Anno Accademico:
2020-2021

22 Settembre 2021

Contents

Abstract

We study the interaction of a fluid with a permeable surface by using the homogenisation theory. Thus, we are able to substitute the permeable surface with a smooth one, at which we apply an effective *slip* condition, written in terms of effective coefficients, whose numerical values directly come from the numerical solution of microscopic problems.

We use a 3D description and consider inertia already at microscopic level, by means of a so-called *Oseen* approximation, recovering the Stokes' limit for $Re_\tau \to 0$. We characterise as well the behaviour of the microscopic parameters by computing them for both spanwise and streamwise aligned cylindrical inclusions, for several different values of porosity θ and of Re_τ, for both inline and staggered arrangements, and proposing also a fit law.

Then, we try to test our effective condition by numerically studying a macroscopic case (a fully developed turbulent channel flow with one permeable wall of spanwise inclusions) and comparing our solutions with a fully-feature resolving DNS present in literature. However, very recently we found that our reference presented different values of some important parameters, thus making a quantitative comparison ineffective and leaving us with only the possibility of a qualitative one. Although we must suspend the judgment about our solutions, some indications make us still confident about our own development.

Finally, simulating again the same macroscopic case but with longitudinal inclusions, we find drag-reduction with respect to the case of smooth wall and are able to reconstruct the drag-curve.

Chapter 1

Introduction

There are several reasons for which one may choose to investigate the motion of a fluid near a permeable surface.

First of all, there is a fundamental reason. At the present time, the full description of the interaction that develops at the boundary wall between the fluid and the surface itself is not clear: if one tries to apply the usual no-slip condition for the case of such a permeable surface, experimental data are not recovered. Over time, some *ad hoc* semi-empirical laws have been found (e.g. by Navier 1823, Beavers and Joseph 1967 and Saffman 1971) to be in good agreement with data. In our framework, instead, such laws and conditions (better and better refined over time) directly come from the theoretical framework. However, it has to be clear that we are still using a theory with effective parameters to model the interaction, so that also this cannot be the ultimate theory.

Secondly, the method we propose allows us to describe the motion in such a way that it is possible to numerically investigate the problem for a reasonably large spatio-temporal scale and with a good resolution (mediating the degrees of freedom of the problem), something which otherwise requires very high computational resources with a fully-feature resolving DNS (direct numerical simulation).

Finally, there are also many practical applications, mostly in the field of the so called bio-mimetic. Indeed, among nature, rough surfaces are the majority, as they can confer incredible properties. For example, the well known hydrodynamical performance of sharks results from dermal tooth-like denticles that cover their bodies, together with their flexibility. Moreover, the plumage of birds plays an important role in their aerodynamic characteristics. Further, in the plant world, micro-roughness surface element may provide for the existence of superhydrophobic surfaces. Man can try to reproduce these particular properties of the natural world by developing engineering surfaces that mimic (or that are inspired by) the natural ones. For example, the design of passive and active flow actuation system could lead to drag reduction or to

mitigate noise. The self cleaning ability of super-hydrophobic surfaces can be used against the formation of bio-fueling on ships. These are only few of the many examples we could cite. Among these, we will focus our attention on the case of drag reduction in a turbulent flow, which is a particularly sensible topic in aerodynamics, since it could lead to a significant economic saving for aircraft societies.

The present thesis is organised as follows. In 1, we give an overview on biomimetics and recall important concepts of fluid dynamics, such as turbulent boundary layer. In 2, we present a literature review about the topic of drag-reduction over rough surfaces, with particular regard to riblets, anisotropic permeable substrates and one experimental result. Then, 3 and 4 are my original thesis project, in which we will use homogenisation theory to properly study the motion of a fluid near a permeable surface. In order to study this configuration, both microscopic and macroscopic problems will be taken into account. In the former (3), we will characterise the effective coefficients that models the fluid-surface interaction for a variety of cases (main numerical results are reported in 4.2, to facilitate any consultation for future work). In the latter (4), we will at first try to test the homogenised conditions against a fully-feature DNS present in literature, then we will search for a drag-reducing surface, aiming to optimise this reduction changing geometrical and dynamical parameters. Finally, in 4.2 conclusions are reported.

1.1   Biomimetics

In this section we present an overview on biomimetics, with references to Luminari 2018; Pauthenet 2018; Alinovi 2018; Zampogna 2018.

1.1.1   Natural Surfaces

While trying to develop synthetic surfaces, one may think that the goal is to make them as smooth as possible, minimizing all the microscopic asperities that are naturally present (for example, think about the incredibly smooth sphere of silicon for the Avogadro Project, which has been a proposal to reach a sample-independent definition of kilogram). However, this is not always true, since rough surfaces, possibly with micro-structured asperities, can exhibit incredible properties with respect to the perfectly smooth ones. This is particularly true for the cases of natural/biological surfaces, for which millions of years of natural evolution have selected the ones that, due to casually altered/mutated treats, allowed the owner organisms to better survive and adapt to external conditions, thus resulting in the optimized ones for those

specific functions. We are going to present some examples of this kind of surfaces. All of these studies go under the name of *biomimetics* (term coined by Otto Schmitt in 1974), which means that man observes natural surfaces and tries to take advantage from them, trying to bio-mimic or bio-adapting into new useful technology (see the example of Velcro in fig. 1.1.1).
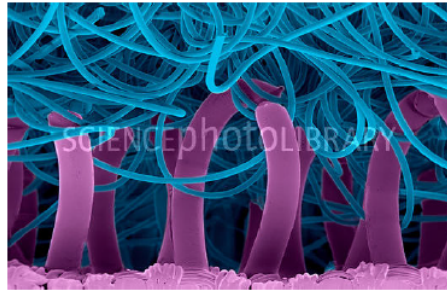
Figure 1.1.1: Velcro device at the microscope, where two different parts have been highlighted: (below) a strip with tiny hooks (spacings $\sim 200\,\mu m$) coupling with another strip with smaller loops (upper). Its inventor, George de Mestral, took inspiration from some burdock seeds which were clung to his coat after a walk in the wood. (The figure is taken from Zampogna 2018).

We have to underline that the "microscopic" length scale through which we are going to see and analyze the asperities is not certainly the atomic scale nor exactly the μm; one may think to define adjective "microscopic", but, generally referring to the internal scale of the medium, we can say the range of its order of magnitude to be almost $\sim (1 \div 10^2)\,\mu m$ and sometimes also $\sim 1\,mm$ (depending on the actual case of interest). On the contrary, with "macroscopic" scale we will always refer with good approximation to $\sim 1\,m$, as order of magnitude. Thus, it will be clear that quantum effects will not be seen at either scales. Furthermore, the velocities involved are very much lower than the speed of light, being the highest macroscopic velocity considered an airplane velocity. Thus, we definitely are in the non-relativistic regime. This enables us to use classical physics (in particular, classical fluid-dynamics) with excellent approximation throughout our discussion.

The first example we cite is the shark skin. As one can see in figure 1.1.2, the surface is made up by a series of overlapped flexible denticles, which can interact with the flow, operating separation control during the periodic oscillating flow generated while swimming and ultimately reducing drag. Moreover, different geometries of denticles can be found in various parts of the shark body, since also flow conditions can differ from part to part. Many engineered surfaces have been developed taking inspiration from the shark skin: NASA V-shaped riblets for improving airplane fuel efficiency, others in aeronautical and naval field, and more recently swimming suits by Speedo.

Another example is the owl, who is known for its silent flight, in order to increase the chances to capture preys. Indeed, the feathers on its wings, which can be treated as a poroelastic surface (see fig. 1.1.3), can suppress noise and

4
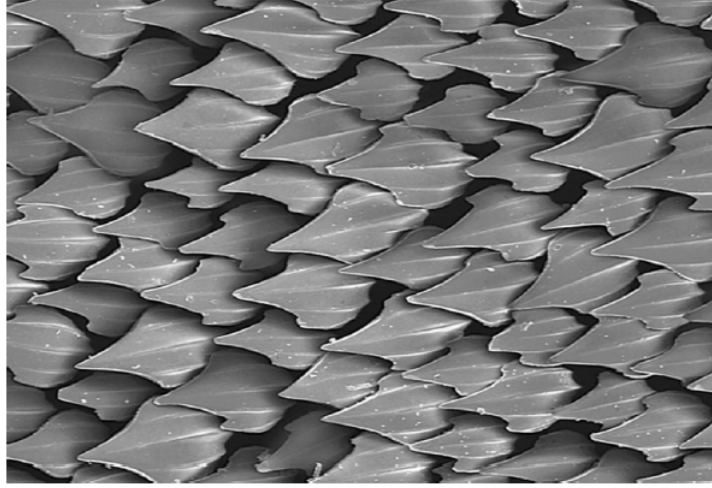
Figure 1.1.2: Shark skin at the microscope. Note the placoid scales, or dermal teeth (denticles), which can reduce drag. The spacing between them is $\approx (10 \div 100)\,\mu m$, similar to the the case of drag reducing riblets. (The figure is taken from Luminari 2018).

Figure 1.1.3: Owl feathers: note filamentous extensions (separations less than $\sim 100\,\mu m$), which can confer them a silent flight. (The figure is taken from Zampogna 2018).

enhance the lift generation. This is due to the combining effect of elasticity and porosity, which can produce a weaker noise amplification. There are current studies in aeroacustic aiming to characterize the problem.

Moreover, we can cite the case of the wing of the butterfly, where multiple scales are involved: there is a first series of overlapped scales and further zooming we can see that each scale has a complicate permeable structure (see fig. 1.1.4). These porous structures give a boost in climbing efficiency of 30%. Moreover, this surface was useful to produce antireflective polyethilene sheets.

Furthermore, one biological example can be made in the world of super-hydrophobic surfaces (for which we will give a few details later). It is known that the lotus leaf is water-repellent: water slides over them because of the low wettability of the surface. This is due to the presence of periodic microscopic protrusions on the surface (see fig. 1.1.5), that, capturing air pockets and changing the contact angle of the water droplets, provoke an effective slip of the liquid, thus reducing drag. The production of self-cleaning surfaces is bio-inspired by the so called *lotus-effect*.
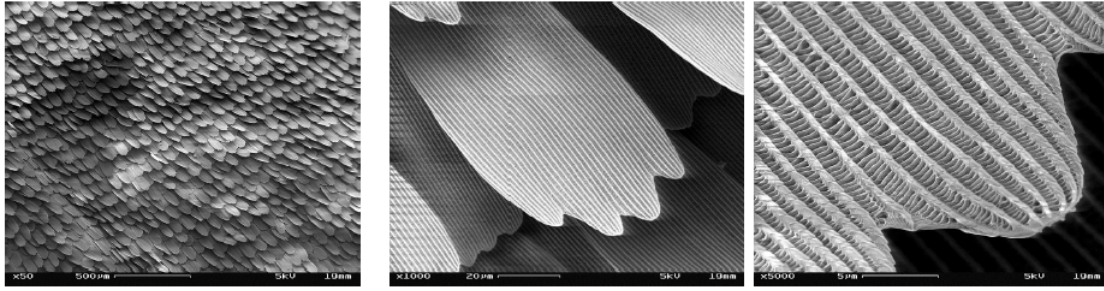
Figure 1.1.4: Electron microscopic images (SEM) of the scales of a peacock butterfly. The multiple scales involved are porous, through which air can flow below the outer lamina, reaching the inner surface. The spacing of the ridges in the outer lamina (separated from the inner one thanks to structures called *trabeculae*) is $\sim 1\,\mu m$. (The figure is taken from Luminari 2018).
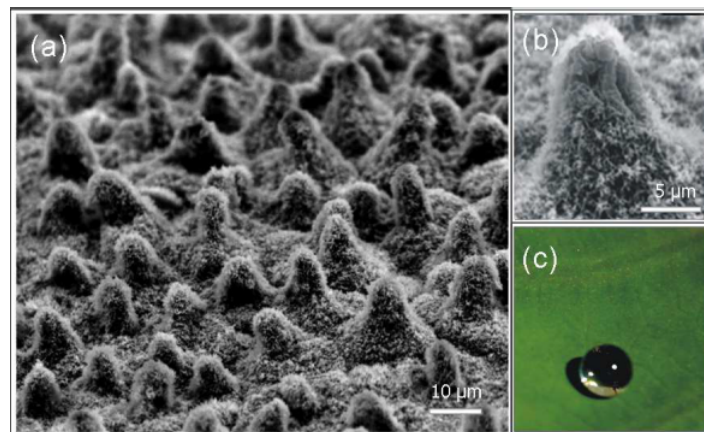
Figure 1.1.5: Lotus effect. (a) SEM image of a lotus leaf. (b) Magnification showing one of the protrusions that cover the surface. (c) Water drop on a lotus leaf. Note the high contact angle (defined later), that allows to maintain a spherical shape. (The figure is taken from Luminari 2018).

Another well known effect is the *gecko effect*: without any kind of chemical addictive, the gecko adhere to several kinds of surfaces, including hydrophobic and hydrophilic ones, thanks to the micro-structures on its foot (see fig. 1.1.6). Its synthetic counterpart are dry adhesive tapes, obviously inspired by the natural ones.

The last example we would cite is the development of microflyers, ornithopters or appendices inspired by wings and feathers or, more generally, by *canopies* which might optimize the flight of traditional airplanes and operate an active or passive control of the flight. So, in the future planes might be hairy (see fig. 1.1.7), allowing to manipulate the flow by appropriately tuning the fur.

Figure 1.1.6: Microscopic view of the feet of the gecko (level of adhesive lamellae). They are covered with microscopic adhesive toe pads (formed by spatula-shaped *setae* arranged in *lamellae*), through which gecko can adhere to smooth surfaces via Van der Waal's interactions. Separations for lamellae is $\approx 200\,\mu m$, for setae is $\approx 20\,\mu m$ and for spatulae is $\approx 5\,\mu m$. (The figure is taken from Zampogna 2018).
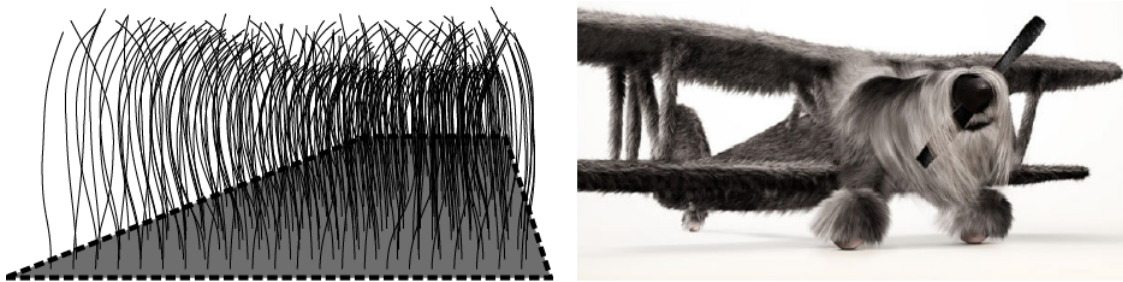
Figure 1.1.7: (a) Schematics of a passive canopy: an ensemble of fibres upon an impermeable wall. (b) An airplane in the future, since a hairy surface provides better aerodynamic performances. (The figure is taken from Pauthenet 2018).

1.1.2 Drag Reduction
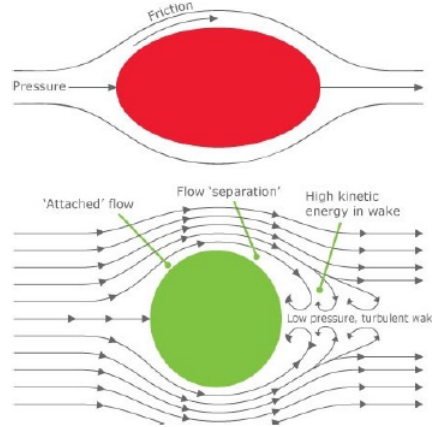
Figure 1.1.8: Drag force for two objects with different shape, separating skin friction drag from form drag (or drag pressure drag) contribution. (a) Oblated section (streamwise body), where pressure drag is negligible and skin friction is prevalent. (b) Circular section, with $\sim 90\,\%$ form drag and $\sim 10\,\%$ skin friction. (The figure is taken from Alinovi 2018).

Let us think of a body moving through a fluid (fig. 1.1.8). The body experiences a mechanical force against its motion (i.e. in the negative direction of the vector velocity of the body) called *drag force*. Usually, one separates the drag force into two main contribution: the pressure drag and the viscous drag (or skin friction). The former is due to the pressure difference between the front and the end side of the body, while the latter is the effective, macroscopic result of the microscopic interaction between the viscous fluid particles and the body with which the fluid is in contact. The viscous forces are dominant in the *boundary layer*, i.e. in a very thin region near the body, where the velocity varies quickly from the surface value to the free stream value. The decomposition is the following:

$$\int_{A_\sigma} [\underbrace{(-p\mathbf{I} \cdot \mathbf{n}_\sigma) \cdot \mathbf{n}_\parallel}_{\text{pressure drag}} + \underbrace{\boldsymbol{\tau} \cdot \mathbf{n}_\parallel}_{\text{viscous drag}}]dA \tag{1.1.1}$$

where p is the pressure, A_σ is the solid interface of the body where a no-slip condition is usually applied, $\mathbf{n}_\sigma$ is its outward normal unit vector, $\mathbf{n}_\parallel$ is the unit vector parallel to the fluid direction and τ is the shear stress for an incompressible and newtonian fluid flow, defined as

$$\tau = \mu \left(\nabla\mathbf{u} + \nabla^T\mathbf{u}\right) \cdot \mathbf{n}_\sigma \tag{1.1.2}$$

where μ is the dynamic viscosity and $\boldsymbol{u}$ is the flow velocity vector.

Reducing drag, and in particular viscous drag, is one of the main goals in many aerodynamic and hydrodynamic applications, since it can lead to significantly reduce fuel consumption and, consequently, to save money (as well

as to achieve better performances). Examples include aircraft, tankers, underwater bodies, pipelines for oil and gas transport. In order to do this, there are fundamentally two approach: active control and passive control. As far as active control is concerned, it involves moving control surfaces, managed by a feedback system made of sensors and actuators. Instead, the passive method does not need an external control, and thus is financially competitive. It requires a modification of the rheological properties of the fluid or an appropriate design of the surface. The first option can be achieved by injecting an appropriate second fluid in the main stream, for example polymers, which form long chains of small molecules called *micelles*. An 80 % drag reduction is found. However, this procedure can be realised only in the case of closed domains, such as pipelines, and the working mechanism has not been fully understood yet. For the second option (design of the surface) one can use riblets to modify the surface, which is our next topic.

1.1.3   Main Surfaces

Riblets

One may think that a rough surface would *increase* drag compared to a smooth one. However, this is not true for cleverly designed rough surfaces, as the ones we are going to consider. But one may still wonder why it could possibly *reduce* drag. We can anticipate that, since the rough wall is equivalent to a plane wall at an effective distance, the resistance to the main flow is not automatically increased by the protusions, as one may think. In particular, if the indentations actually damp cross-flow, and thus secondary streamwise vortices, the resistance may even be reduced, as it is in certain conditions. Now we describe the case of riblets.

(a) Triangular riblet.   *(b)* Spaced triangular riblet.

(c) U-shaped riblet.   *(d)* Blade riblet.
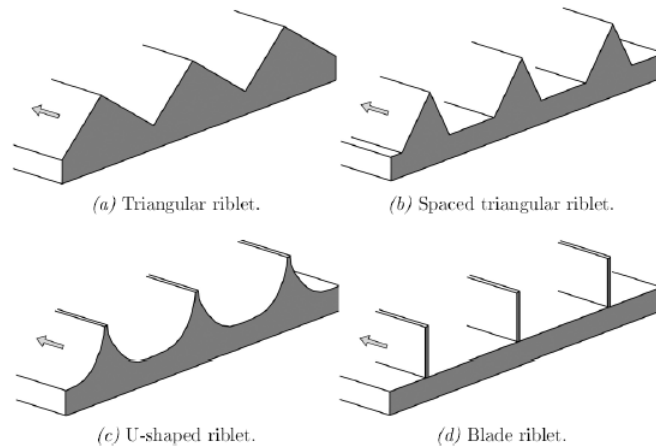
Figure 1.1.9: Several examples of different riblets geometries. Typical spacing values are in the range $(10 \div 100)\,\mu m$. (The figure is taken from Alinovi 2018).
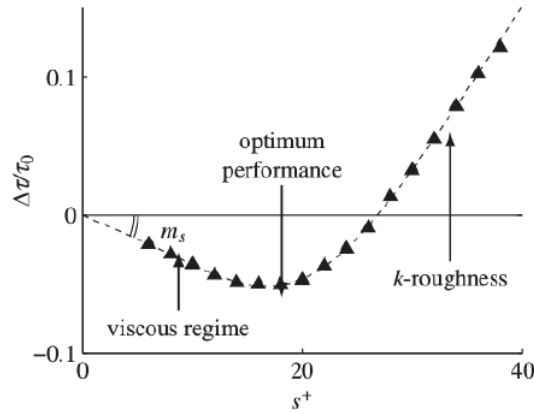
Figure 1.1.10: Drag curve plotted against riblets size s^+. Drag optimum is for $s^+ \approx 15$, while there is drag increase beyond $s^+ \approx 25$. Usually, the variable s^+ has to be substituted with other geometrical lengths, as we will see later. (The figure is taken from Luminari 2018).
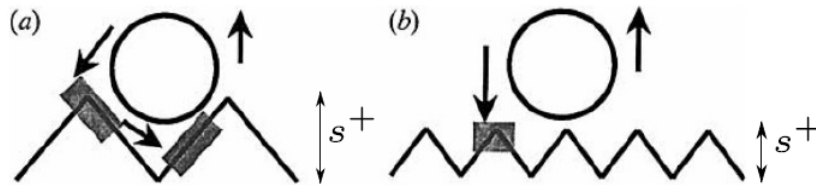
Figure 1.1.11: Behaviour of an eddy over riblets: for (a) small riblets size the eddy does not penetrate (drag reduction) (b) large riblets size the eddy does penetrate (drag increase). The gray area is where friction is dominant. (The figure is taken from Luminari 2018).

Riblets are tiny streamwise-aligned surface grooves (see fig. 1.1.9 for a schematic). They inhibit the lateral turbulent motion and smooth the fluctuations of the cross-flow in the viscous sublayer close to the surface, aligning it along the mean flow direction and thus reducing the turbulent momentum transfer towards the surface, which in the end leads to viscous drag reduction. This reduction correlates well with the spacing between each riblet, s^+ (see fig. 1.1.10): skin friction first decreases for small s^+, reaching drag optimum, and then increases until it surpasses the smooth surface value, ultimately leading to drag increase for large s^+. This trend reflects the competition between the obstructing lateral fluid flow and the increase of penetration of high speed vortices inside the protrusions. In other words (with reference to fig. 1.1.11), when the riblets are closely spaced, the turbulent vortices are pushed away and a small local area of the surface experiences high-shear stresses (and skin friction is reduced), whereas, when the space between them is too large, the vortices can penetrate inside the grooves and a larger area is exposed to the local velocity (and skin friction is increased). A large scale employment of this technology is limited by the fact that the production and maintenance costs surpass the economic saving from drag reduction. This is due to the fact that the riblets size needs to be very small to work properly and that they accumulate dust, ice and other external agents that have to be removed after every single use.

SHS and LIS

In order to realise a superhydrophobic surface (SHS), one has to couple the regular micro-asperities of a surface with a gas, thus creating gaseous pockets over which a liquid simply flows with less friction.
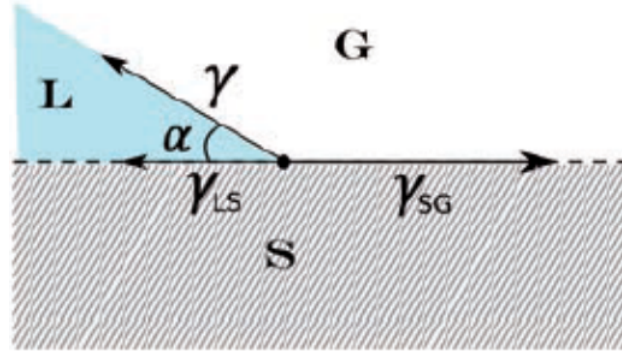
Figure 1.1.12: Schematics of a triple point with geometrical parameters. The phases at the triple point are a liquid (L), a solid (S) and a gas (G). α is the contact angle, while γ is the interfacial energy, i.e the work per unit of area required to increase the surface area of a substance in contact with another one (with obvious meaning of the subscripts). (The figure, originally made by Bottaro, is taken from Alinovi 2018).

In this framework, a surface is classified by means of the contact angle α that a water droplet assumes over it (fig. 1.1.12):

- hydrophilic: $0° < \alpha < 90°$

- hydrophobic: $90° < \alpha < 150°$

- superhydrophobic: $\alpha > 150°$

The material involved are three: the surface, the liquid and the gas.
Wenzel demonstrated that, for a rough surface, the wetting angle increases as

$$\cos(\alpha_w) = r \cos(\alpha) \tag{1.1.3}$$

where α_w is the effective angle on a rough surface and r is a parameter, to be determined experimentally, that is related to the effective surface at the interface. Since $r \geqslant 1$, micro-structures actually increase the hydrophobicity of a surface, explaining the microscopical pattern geometry of the lotus leaf (1.1.13).
If the gas is air, ultra- or super-hydrophobicity can be reached, with the drop sitting on an air cushion.
However, the problem of SHS is that the gaseous pockets are not robust and they can easily collapse. An alternative is to substitute the gas with oils, obtaining a liquid-impregnated-surface (LIS). The working mechanism is very similar to the case of SHS: the relative slip between the two fluids leads to a skin friction drag reduction. LIS have a more stable fluid-fluid interface and

Figure 1.1.13: Lotus effect. (a) a water droplet on a lotus leaf. (b) electron microscope image of the leaf top showing the microstructures that form its surface. The separations are $\sim 10\,\mu m$. (The figure is taken from Alinovi 2018).

also show interesting properties in terms of biofouling and ice-phobicity. However, drag reduction deteriorates if the oil viscosity is large with respect to the other fluid one.

Poroelastic media

The poroelastic theory analyses an elastic porous medium containing interconnected fluid-saturated pores. The fluid interacts with the solid, modifying its mechanical properties: it stiffens the material and, if there is a gradient of pore pressure, it applies a stress on the solid, deforming it and leading to volumetric changes in the pores. This ultimately changes the fluid pressure itself. Thus, one has to look for a relationship between solid stress and fluid pressure. The main applications deals with hydrogeology, geomechanics, petroleum engineering, but also with biomechanics. We are going to present the cases of permeable surfaces and of canopies.

Permeable surfaces A permeable surface is a permeable covering with a non negligible thickness, in contrast to riblets.

In the laminar regime, the actual *slip* velocity at the interface can lower the skin friction, whereas in the turbulent case there is a net drag increase due to the instabilities at the boundary. Let us see the mechanism. The slip velocity alters the boundary layer and, consequently, the stability condition of the flow, producing less shear and vorticity and finally leading to the formation of a shear layer in the front of the body, which shows a KH instability that develops in the Von Karman street.

Regarding the change in pressure (see fig. 1.1.14), we can say that the pressure increases in the back part since, as a result of the strong dissipation provoked by the medium, the flow coming out from the body is laminar and very slow.
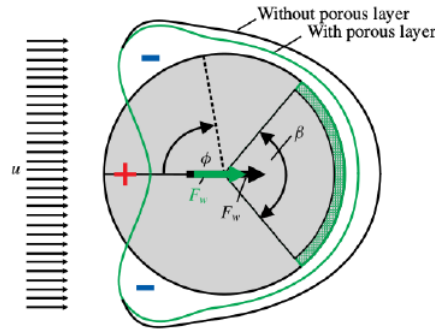
Figure 1.1.14: The picture shows the angular distribution of pressure for a cylinder, highlighting the case with the porous layer (green line) and without it (black line). Note the increase of pressure in the rear point. (The figure is taken from Luminari 2018).

Canopy flows We now mention the case of the canopy flows. They can be seen as flows over elastic slim shapes, such as trees and aquatic vegetation. As application we can mention the case of wind over plants, which plays a crucial role in lots of situation, for example in the transport molecules as CO_2 and nutrients.
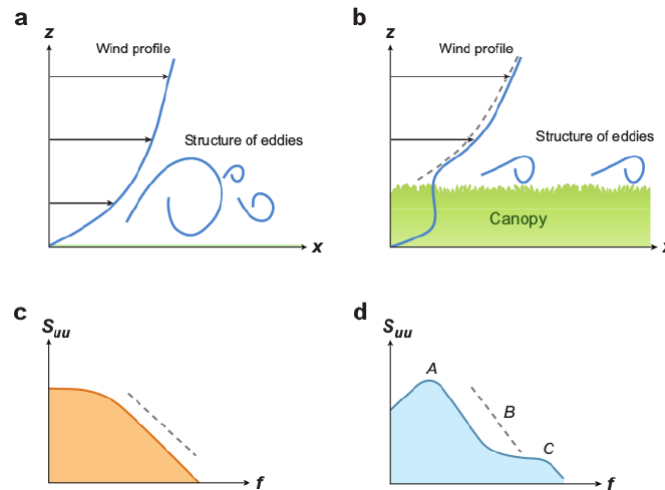
Figure 1.1.15: Velocity profile (a,b) and spectrum (b,c) for a rough wall and a canopy flow. (a,b) Note the difference in the eddy size and the inflection point in the canopy flow. (c,d) Note the larger peak in the frequency of the mixing layer instability, a steeper slope in the energy cascade part and the high frequency peaks at high frequencies. (The figure is taken from Luminari 2018).

There are clear differences in the boundary layer profile between canopy and of the rough wall (see fig. 1.1.15). In the former there is an inflection point that leads to KH instabilities. Furthermore, also the spectra are different, since for a rough wall a Kolmogorov energy spectrum can be recovered, while for canopy flow we can observe a larger peak in the frequency of the mixing layer instability, a more abrupt slope in the energy cascade part and high frequency peaks.

Canopies can also inhibit separation when there is an unpleasant pressure gradient, as in the case of the flow over a hill.

1.2 Turbulent Boundary layer
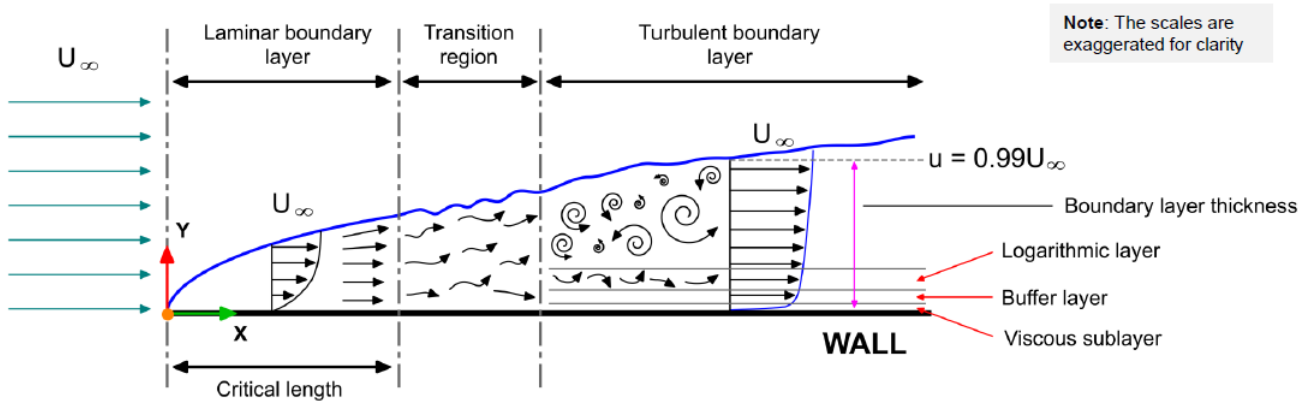
Figure 1.2.1: Boundary layer for Laminar-Transitional-Turbulent flows. (The figure is taken from Guerrero 2021).
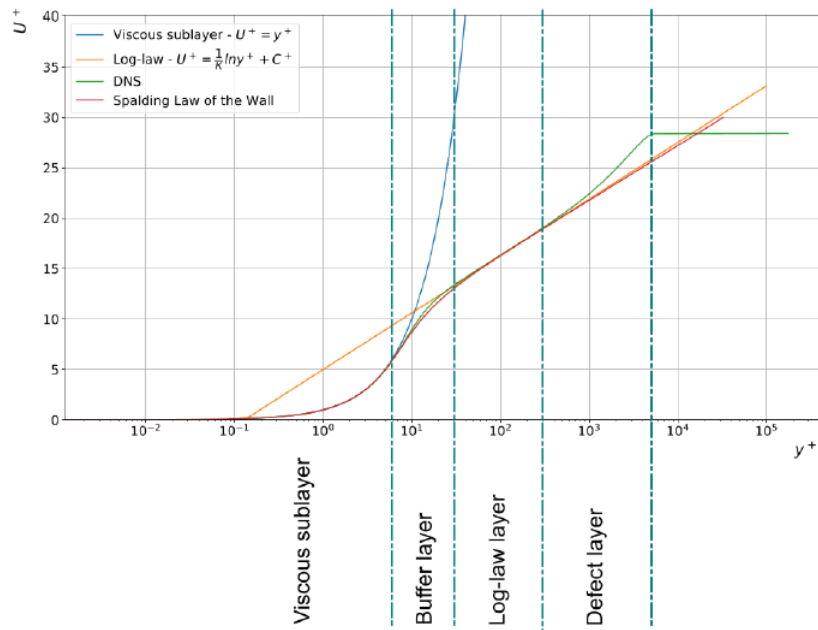
Figure 1.2.2: Law of the wall in the different regions (non-dimensional profile). (The figure is taken from Guerrero 2021).

The velocity profile in the turbulent boundary layer (see fig. 1.2.1) has been deeply studied, leading to a good knowledge of what happens in this thin but important region. One usually subdivides it into different zones (see fig. 1.2.2, 1.2.3, 1.2.4). Before doing that, it is useful to define the main quantities we are going to deal with. If y is the wall normal coordinate, we render it a-dimensional defining $y^+ = \frac{u_\tau y}{\nu}$, with $u_\tau = \sqrt{\frac{\tau_w}{\rho}}$ the shear velocity, and τ_w the wall shear stress. Furthermore, we also scale the mean velocity U with respect to the shear velocity: $u^+ = U/u_\tau$. Now, we illustrate the law of the wall and the subdivision of the turbulent boundary layer.
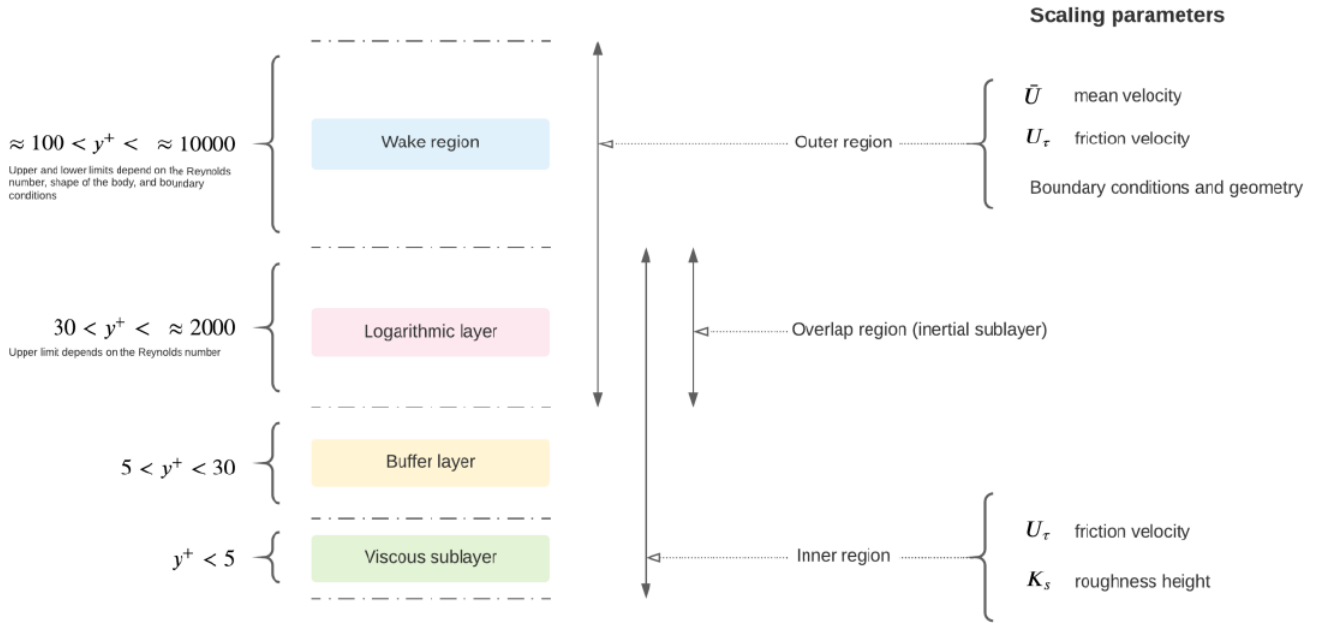
Figure 1.2.3: Different regions in the turbulent boundary layer. (The figure is taken from Guerrero 2021).
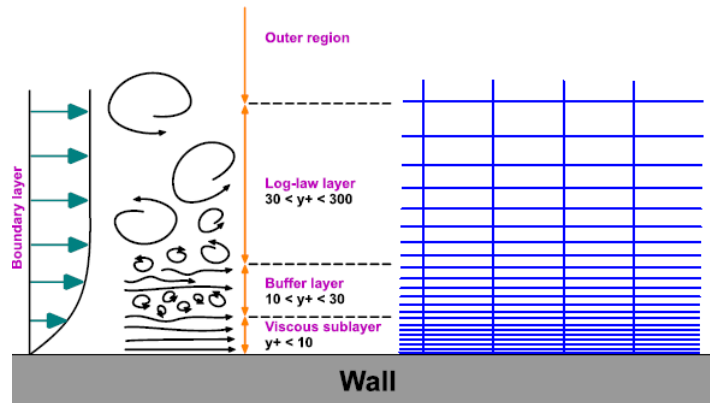
Figure 1.2.4: Near wall turbulence, highlighting, from (sx) to (dx), the mean velocity profile, the energy cascade, the different regions of the boundary layer and an hypothetical grid/mesh level of refinement comparison for the different regions (near wall treatment). (The figure is taken from Guerrero 2021).

- The **law of the wall**, is one of the cornerstones of fluid dynamics and turbulence modeling. Basically it describes the mean velocity distribution close to the wall. It is based on the early works of Prandtl, Von Karman, Nikuratze, and Millikan. Many other authors have derived/confirmed the law of the wall using experimental or numerical measurements. We will not follow the derivation, limiting ourselves to only quote the main result. By using dimensional analysis and taking the right assumptions, the following expression can be derived

$$\frac{U}{u_\tau} = f\left(\frac{y u_\tau}{\nu}\right) \tag{1.2.1}$$

or, by using non-dimensional variables,

$$u^+ = f\left(y^+\right) \tag{1.2.2}$$

- **viscous sublayer**: The viscous sublayer is the inner-region of the boundary layer, very close to the wall ($y^+ \lesssim 5$), where the flow is laminar and viscous effects are dominant. Here the flow mean velocity is linear with respect to the wall normal coordinate:

$$u^+ = y^+ \tag{1.2.3}$$

- **buffer layer**: In the buffer layer ($5 \lesssim y^+ \lesssim 30$), where the flow transitions from laminar to turbulent, no analytical laws are defined. The viscous and inertial forces are of the same order and, in the middle of this region, the peak production and dissipation of the turbulent energy is known to occur.

- **log-law region**: The logarithmic law refers to the outer-region of the boundary layer ($30 \lesssim y^+ \lesssim 300$). Measurements show that, for both internal and external flows, the streamwise velocity in the flow near the wall varies logarithmically with distance from the surface:

$$u^+ = \frac{1}{\kappa} \log(y^+) + C^+ \tag{1.2.4}$$

where $\kappa \approx 0.4$ is the Von Karman's constant and $C^+ \approx 5$. This is one of the most famous empirically determined relationships in turbulent flows near solid boundaries. From the non dimensional u^+ vs y^+ plots, it is possible to fit a function that covers the entire laminar and turbulent regimes. The most widely known velocity profile is Spalding's law, which is essentially a fit of the laminar, buffer and logarithmic regions of the boundary layer:

$$y^+ = u^+ + \frac{1}{E}\left[e^{\kappa u^+} - 1 - \frac{\kappa u^+}{1!} - \frac{\left(\kappa u^+\right)^2}{2!} - \frac{\left(\kappa u^+\right)^3}{3!} - \frac{\left(\kappa u^+\right)^4}{4!} \right] \tag{1.2.5}$$
$$\frac{1}{E} = e^{-\kappa C^+}$$

Here E is another a-dimensional fit constant, whose typical value is $E \approx 9$.

For decades, there were no mean velocity data close enough to the wall. One of the first works to measure data very close to the wall and in the inner region is that of Lindgren in 1965. The agreement of these measurements with Spalding's formula is excellent (see fig. 1.2.5).
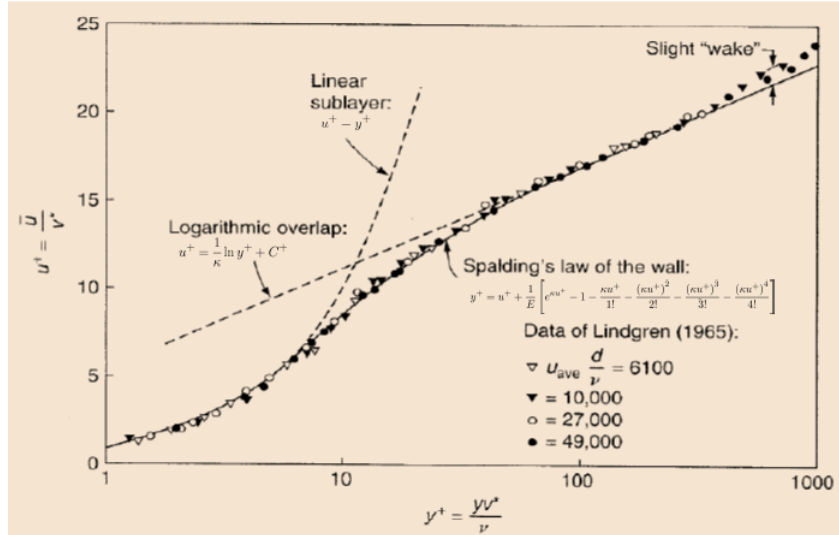
Figure 1.2.5: Comparison of Spalding's inner law expression with pipe flow data of Lindgren, showing an excellent agreement. (The figure is taken from Guerrero 2021).
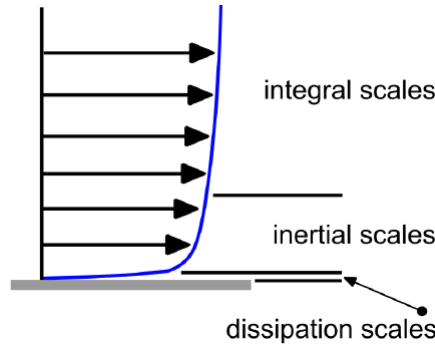
Figure 1.2.6: Qualitative velocity profile, highlighting the different scales of motion. (The figure is taken from Guerrero 2021).

The use of the non-dimensional velocity u^+ and non-dimensional distance from the wall y^+ results in a predictable boundary layer profile for a wide range of flows. Under standard working conditions this profile is the same. However, under non-equilibrium conditions (production and dissipation of turbulent kinetic energy not balanced), rough walls, porous media, buoyancy, viscous heating, strong pressure gradients, and so on, the profile might be different. While the non-dimensional velocity profile is the same for many flows (fig. 1.2.2), the physical velocity profile is different (fig. 1.2.6). This can be explained if we take into consideration the role of the turbulent fluctuations, as briefly indicated below.

Let us recall the definition of turbulence: unsteady, aperiodic motion in which all transported quantities fluctuate in space and time. Every transported quantity shows similar fluctuations (pressure, temperature, species, concentration, and so on). For most applications it is impractical to account for all these instantaneous fluctuations. Therefore, we need to somehow remove, avoid, or filter those small scales by using models (averaging or filtering the
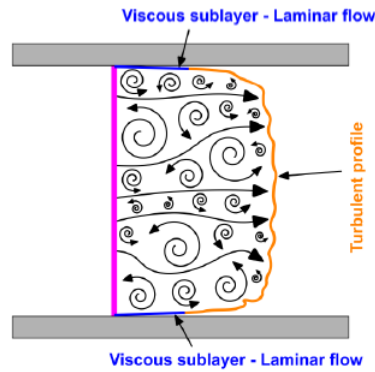
Figure 1.2.7: Turbulent flow representation, where the viscous sublayer is highlighted and the flow profile is the instantaneous one (i.e. it has not been averaged). (The figure is taken from Guerrero 2021).
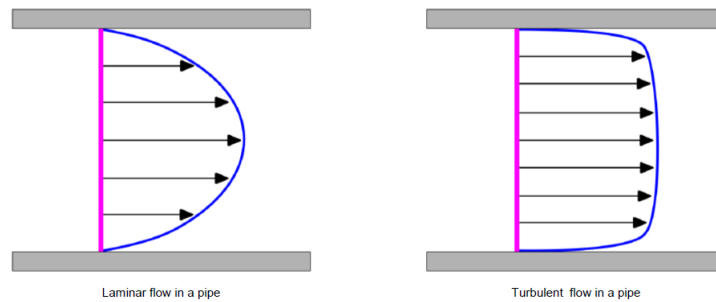
Figure 1.2.8: Picture of two different kind of mean/averaged flow profile: (sx) laminar flow, (dx) turbulent flow. (The figure is taken from Guerrero 2021).

governing equation). This gives rise to an averaged flow pattern, which is not the actual flow pattern.

- In the laminar case (fig. 1.2.8 sx), the velocity gradient close to the walls is small (therefore the shear stresses are lower).

- The turbulent case (fig. 1.2.8 dx) shows two regions. One thin region close to the walls with very large velocity gradients (hence large shear stresses) and is laminar, and a region far from the wall where the velocity profile is nearly uniform and the flow becomes turbulent (see also fig 1.2.7). Turbulence increases the wall shear stresses and enhances mixing. In the illustration, the velocity profile of the turbulent case has been averaged. In reality, random fluctuations of the velocity field and transported quantities are present (fig. 1.2.7).

Knudsen number

A useful adimensional number is the Knudsen number Kn, defined as Kn $= \frac{\lambda}{L}$, where λ is the mean free path of a fluid particle and L is a representative physical length scale. This parameter is used to determine when the continuum hypothesis is not valid anymore (see fig. 1.2.9). Although there is no definitive criterion, the continuum flow model starts to break down
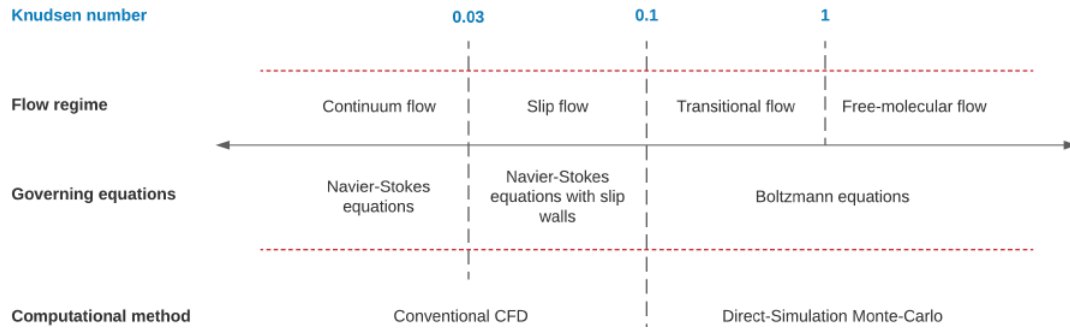
Figure 1.2.9: Description of the different models to correctly study a fluid-dynamical system for different values of the Knudsen number, which can indicate when the continuum approach is not valid anymore. (The figure is taken from Guerrero 2021).

when the Kn $\approx$ 0.1: the flow is rarefied and cannot be treated as a continuum and different equations need to be used (Boltzmann equations). For $0.03 \lesssim$ Kn $\lesssim 0.1$ (moderately rarefied gases), the Navier-Stokes equations are valid in the freestream, but we need to use *slip conditions* at the walls. Finally, for Kn $\approx$ 0.03 the continuum hypothesis is valid and we can use usual Navier-Stokes equations.

1.3 Homogenization Theory

We now give a very brief explanation of homogenisation theory, adapted by Bottaro 2019. We will see this technique in detail in 3.

The word *homogenization* was probably coined by Babuska 1976, who described it as "the approach which studies the macrobehaviour of a medium by its microproperties" by replacing the rapidly varying properties of a "heterogeneous material" with those of "an equivalent homogeneous one".
A heterogeneous material is one which is composed of domains made by different materials or phases, such as a composite or a porous matrix.

Homogenization theory applies to different field in physics, first of all in solid state physics, where one needs to homogenize material properties, also when local properties have a random distribution: just think of the thermal conductivity, the permeability of a porous matrix, the magnetic conductivity of electrically conducting media, the elastic modulus of a solid.

Continuum mechanics is a prime example of homogenization; it employs homogenized coefficients, e.g. the *viscosity* of a fluid which characterizes momentum transport within a fluid: macroscopic quantities are employed while ideas related to molecular interactions are left aside.

We limit our discussion to the case where a repetitive pattern of the microstructure of the media emerges: the goal is thus to replace the effect of the small scale features with macroscopic effective properties, arising from the so-called *auxiliary problems* defined in the *microscopic domains*.
Let us assume that the surface is formed by small indentations. The indentations have a characteristic length scale l, much smaller than the characteristic length scale L of the medium. Thus, the existence of these two separate length scales renders the problem amenable to a formal asymptotic expansion in terms of a small parameter $\epsilon \equiv l/L \ll 1$ (multiple scale expansion), looking for a solution up to any order of accuracy in ϵ.

1.3.1 Slip-condition

The problem to find the correct boundary condition for the case of a viscous fluid above a solid surface interested researchers even before the Navier-Stokes equations were derived.
Indeed, Navier himself (Navier 1823) stated that "the molecules in the proximity of solid walls can only move in the plane of the walls" and argued that the resistance of the wall, balancing the force exerted by the fluid onto it, was proportional to a *slip velocity*, founding a boundary condition that we can write as

$$U = \epsilon \lambda^x U_Y \tag{1.3.1}$$

where Y denotes the wall-normal direction, U the wall-tangent velocity. λ^x, the Navier constant, is an effective penetration depth and the subscript Y means partial derivative respect to Y.

Stokes, instead, started using a slip condition before changing for a no slip one.

The problem seemed to be definitely settled by Taylor, who, in a series of experiments on the flow between concentric cylinders, obtained perfect agreement between experimental measures and theoretical predictions using a no-slip condition at the wall (Taylor 1923).

However, still today the no-slip condition poses problems in all the situations where small-scale effects at the wall make the fluid-fluid or fluid-solid interaction non negligible. Examples of this include a liquid spreading down an incline, the flow of rarefied gases with $0.01 \lesssim Kn \lesssim 0.1$ (studied also by Maxwell 1879) and the flow over micro-corrugated surfaces, which can be either superhydrophobic or lubricant-impregnated. In all these cases, in order to achieve a correct description of the fluid, the homogenization strategy, with a conjugate microscopic/macroscopic view, is highly preferable to a pure computational approach, which would require refined meshes in order to account for all the small details. We would like to remember that in biomimetics irregular surfaces, possibly with regularly microstructured porous substrates, are the norm, not the exception.

Chapter 2

Drag reduction over rough surfaces: literature review

In the present section, we will give some details about the study of turbulent flow over rough surfaces, focusing on drag reduction and its optimisation.

The main references are Endrikat 2020; Chavarin et al. 2021; Luchini, Manzo, and Pozzi 1991; Zhou et al. 2021.

2.1 Riblets

Here we consider the case of riblets, following the discussion by Endrikat 2020 and, subsequently, by Endrikat, Modesti, et al. 2020; Endrikat, Modesti, et al. 2021.

2.1.1 Skin friction

Skin-friction drag is caused by a viscous fluid rubbing against the surface, it is proportional to the surface area and it increases while increasing velocity. Roughly, half of the drag transport aircraft experienced in cruise conditions results from skin-friction, making its reduction financially and environmentally attractive for aeronautical and maritime applications. The skin-friction coefficient $C_f = \frac{2}{U_\delta^{+2}}$ is defined by the friction-scaled mean streamwise velocity $U^+ = U/u_\tau$ at the half-channel or boundary-layer height δ. The symbol $+$ denotes viscous scaling with ν (the kinematic fluid viscosity) and friction velocity $u_\tau = \sqrt{\tau_w/\rho}$ (with ρ the fluid density and τ_w the wall shear stress - drag per unit area), such that $C_f = \frac{2\tau_w}{\rho U_\delta^2}$. Drag reduction of a riblet surface (compared to the smooth case) is given by the relative change of the skin-friction coefficient: $DR = 1 - \frac{C_f}{C_{f,smooth}}$. However, the coefficients degrade as Re increases. So, a Re independent parameter that quantifies drag reduc-

tion is given by the decrease of the viscous-scaled mean streamwise velocity at matched heights in the outer layer of two flows with the same friction Reynolds number ($Re_\tau = \delta^+ = \delta u_\tau/\nu$): $\Delta U^+ = U^+_{smooth} - U^+$. Note that there is drag reduction when $\Delta U^+ < 0$. For example, $DR \approx -0.1\Delta U^+$ at $Re_\tau = 395$ (accessible through DNS) and $DR \approx -0.06\Delta U^+$ at $Re_\tau = 50 \cdot 10^3$ (flight conditions).

2.1.2 Small and Large Riblets

Riblets are tiny streamwise-aligned surface grooves with spacings $s \approx (10 \div 100)\,\mu m$ (as a order of magnitude) that have the potential to reduce skin-friction drag compared to a smooth wall, by displacing turbulent motions upwards in the boundary layer.

They are classified as passive flow-control devices, as no energy input is required to favourably alter the flow field, making them attractive for aeronautical and maritime applications as well as for pipes.

Laboratory tests of riblets have reduced skin-friction drag by up to 8.2% for $Re_\tau < 700$. The reduction goes to approximately 5.5% for flight conditions at $Re_\tau \approx 48 \cdot 10^3$. However, at present they are not used on commercial flights because their costs (installation and maintenance) surpasses the current drag-reduction benefits.

We can figure the action of riblets in the following way: they displace small turbulent eddies present in the flow upwards and out of the grooves, limiting the mixing of streamwise momentum in the vicinity of the surface (Luchini, Manzo, and Pozzi 1991), and thus reducing drag. We must consider separately the case of small and large riblets, since the actual drag curve shows a dependence on riblets size (fig. 2.1.1).
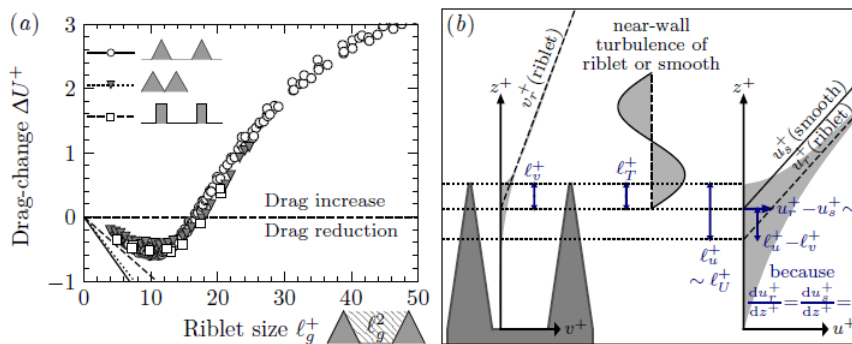
Figure 2.1.1: (a) Drag-change between a smooth and a riblet surface. (b) Near-wall portion of streamwise (u_r^+) and spanwise (v_r^+) Stokes flow profiles for a riblet. (The figure is taken from Endrikat 2020).
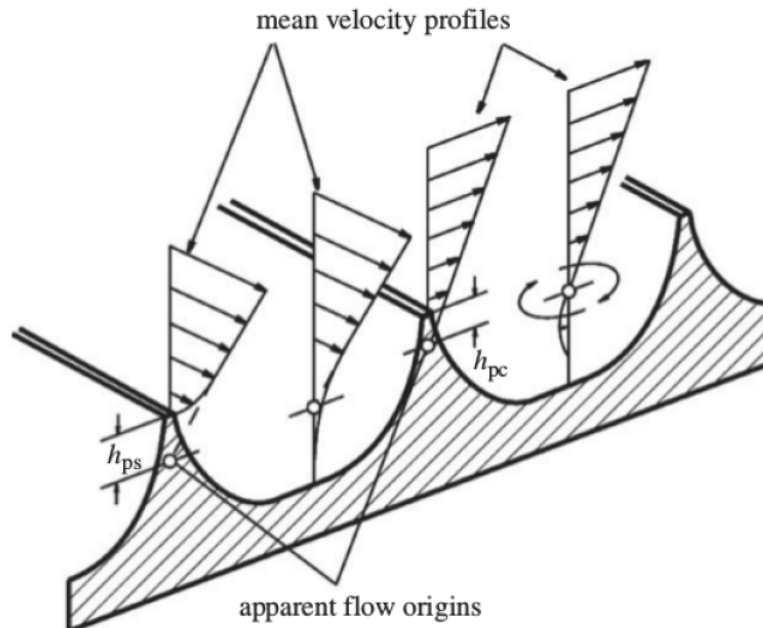
Figure 2.1.2: Geometrical visualization of the concept of protrusion height for the streamwise (h_{ps}) and cross-flow velocity (h_{pc}). (The figure is taken from Luminari 2018).

Small Riblets

In more detail, in the limit of vanishingly small riblets, the mechanism through which riblets reduce drag can be rationalised in terms of the offset in the virtual origin felt by the mean flow and the virtual origin felt by the turbulent fluctuations (Chavarin et al. 2021). Indeed, the velocity profiles appears as if it is originated from an equivalent plane wall, located below the riblet tips (Luchini, Manzo, and Pozzi 1991). In order to understand this concept, it can be useful to introduce the concept of protrusion height (see fig. 2.1.2). The *protrusion height* is defined as the vertical distance between the riblet top ridge and the point of zero velocity (extrapolated from the constant velocity gradient outside above the protrusions). For the streamwise and crossflow velocities, one finds, respectively, the streamwise protrusion height h_{ps} and the cross-flow protrusion height h_{pc}. They can both be computed with a simple Stokes problem over the local geometry of the grooves. Actually, the difference of two protrusion heights ($h_{ps} - h_{pc}$) is related to the difference between two virtual plane walls.

We remember that the typical size of riblets is approximately given by the height of the viscous sub-layer, where convective terms are negligible. So one can use the much simpler (steady) Stokes equations, rather than the full Navier-Stokes equations.

This is why small riblets with spacings of typically less than 30 viscous units ($\mathcal{O}(10\,\mu m)$ on aircraft fuselage in cruise conditions) reduce skin-friction drag compared to a smooth wall.

In even more detail (see fig. 2.1.1 b), the streamwise mean-flow reaches an average depth below the riblet crest given by the longitudinal protusion height l_U^+, that depends on the groove shape and size. Turbulent lateral flow is obstructed by the riblets and therefore only penetrates the groove to a depth given by $l_T^+ < l_U^+$. A reference smooth wall should be considered at the height given by l_T^+ for the two flows to be similar, i.e. that their total stresses match at every height. This placement of the reference wall therefore provides the correct measure of the drag- change ΔU^+. At the height of the reference smooth-wall, the riblet flow has the velocity $U^+ = l_U^+ - l_T^+$, because the slope $dU^+/dz^+ \approx 1$ in the viscous sublayer. The velocity difference compared to the smooth wall flow extends into the logarithmic layer, where it describes the drag-change $\Delta U^+ = l_U^+ - l_T^+$.

The drag-change optimum of traditional riblet shapes was empirically shown to scale with the viscous-scaled groove cross-section A_g^+ and is obtained for riblet sizes $l_g^+ = \sqrt{A_g^+} \approx 10.7$.

Large Riblets and KH instability
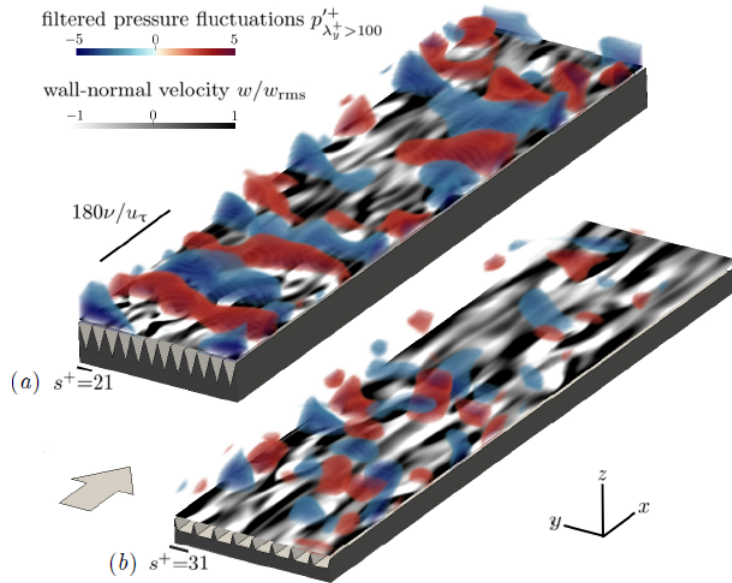
Figure 2.1.3: (a) Visualisation of Kelvin Helmholtz rollers above drag-increasing triangular riblets. (b) KH rollers are absent above trapezoidal riblets of similar groove size. (The figure is taken from Endrikat 2020).

For larger riblets ($l_g^+ \gtrsim 10.7$), instead, drag increases and ultimately surpasses smooth-wall drag (for $l_g^+ \gtrsim 17$), because the flow in and around the grooves becomes less dominated by viscosity as different inertial flow effects contribute to drag.

Three main mechanisms have been proposed to explain the details of this increment.

As the spacing of triangular riblets becomes large enough for streamwise vortices to descend into the groove, they sweep high-speed fluid towards an increased wetted area and thus enhance skin-friction drag.

The spanwise component of streamwise vortices is deflected downward by the riblet tips, creating secondary flows that transport momentum towards the wall.

Furthermore, Kelvin-Helmholtz rollers (fig. 2.1.3) have been shown to augment wall-normal momentum transport towards the wall above blade riblets, leading to increased drag. These rollers evolve around an inflection point in the profile of mean streamwise velocity that is created between the slower flow in the groove and the faster bulk flow above. However, KH rollers can also appear without an inflection point, because in the limit of infinite permeability, the impedance boundary condition mimics a free shear layer.

It has been observed that KH rollers becomes more significant with increasing size of blade riblets, which coincides with the breakdown of drag reduction for $l_g^+ \gtrsim 11$.

Kelvin-Helmholtz rollers are well known in free shear flows, but have also been observed in wall-bounded flows over porous surfaces and vegetation canopies.

2.1.3   Numerical simulations and KH instability
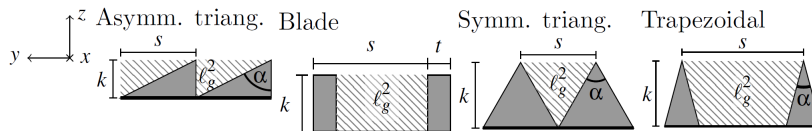
Figure 2.1.4: Schematic of different riblets geometries (asymmetric triangular, blade, simmetric triangular and trapezoidal). (The figure is taken from Endrikat 2020).

In order to evaluate KH instability dependence on riblets shape (fig. 2.1.4, 2.1.5), authors investigated the velocity spectrum at different scales and different wall-normal distances for a total of 29 configurations (seven different shapes and various viscous-scaled size) through DNS in minimal-span channels ($L_y \ll \delta$), which reduces the computational cost in exchange for unphysical results towards the top of the domain. Indeed, changing the riblets geometry has the potential to alter not only the wall-normal permeability of the plane at the riblet crest, but also the mixing layer around the riblet tips from which KH rollers develop.

Minimal-span channels and Geometry

The width $L_y < \delta$ of minimal-span channel (fig. 2.1.6) is small enough to constrict large eddies in the flow. This leads to a significantly altered flow
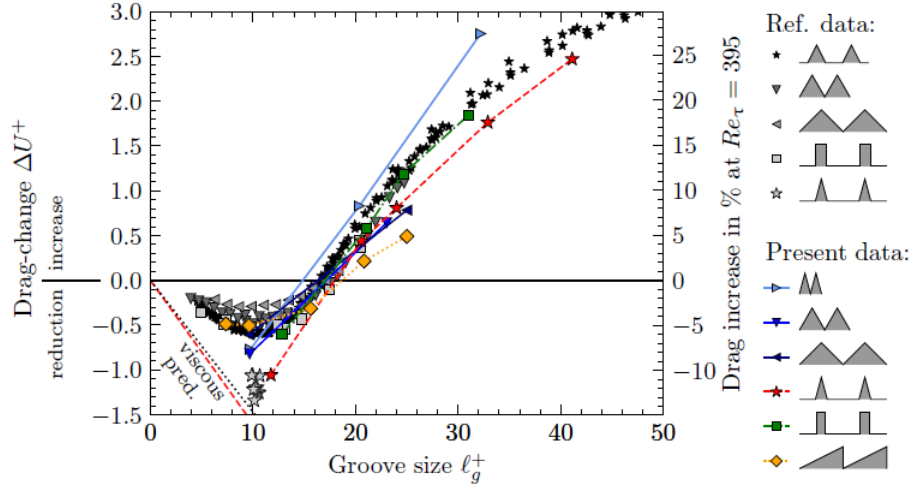
Figure 2.1.5: Drag curve against l_g^+ for different riblets shapes. (The figure is taken from Endrikat 2020).
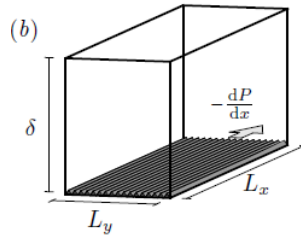
Figure 2.1.6: Unit cell of the computational domain of the simulation for minimal-span open channels. δ is the half-channel height. (The figure is taken from Endrikat 2020).

field in the outer layer, but, below a critical height z_c^+, average velocities (fig. 2.1.7) and turbulent statistics match experimental results (fig. 2.1.8). Constraining the flow in the spanwise direction unphysically alters the flow in the outer layer, while the near-wall region remains unchanged (fig. 2.1.9).

If the wavelength is $L_y^+ \gtrsim 250$, turbulence in the first 30 viscous units above the riblet crest is not affected by the channel width, and both the mean and the turbulent flow they simulated in that region reflect the true physics of the problem (fig. 2.1.7, 2.1.8). Therefore, their minimal-span channels with $L_y^+ \approx 250$ allow to investigate fluctuations due to KH rollers. Even more narrow domain could be used ($L_y^+ \approx 150$), but their choice allows to better filter fluctuations with sufficient spanwise spectral separation between KH rollers and other near-wall turbulence. This is because KH instability affects a distinct spectral region in the flow over riblets: the lower bound for the spanwise extent of KH rollers should be in the range $125 \lesssim \lambda_y^+ \lesssim 250$, with a threshold closer to $\lambda_y^+ \approx 250$, in order to exclude turbulence from the near-wall (NW) cycle (fig. 2.1.10). In this way, they only let fluctuations due to KH instability pass, discarding the ones associated with the NW cycle that characterises both the smooth and the riblets wall flaws.
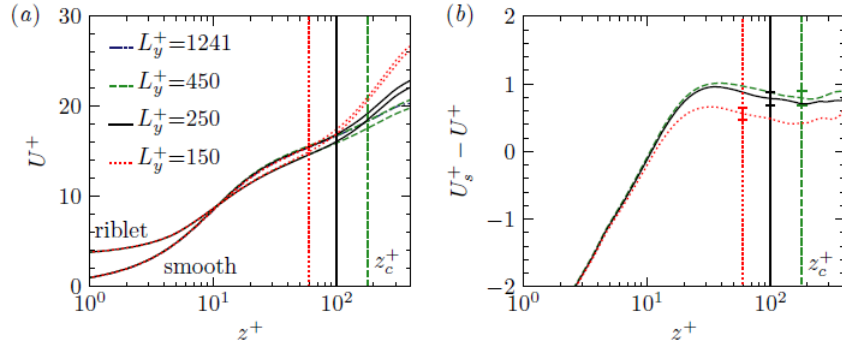
Figure 2.1.7: Unphysical results for average velocity. Note that they are present only for $z^+ > z_c^+$ (vertical lines). (a) Velocity profiles of smooth-walls and triangular riblets for different widths. (b) The roughness function $U_s^+ - U^+$ for the three cases. (The figure is taken from Endrikat 2020).
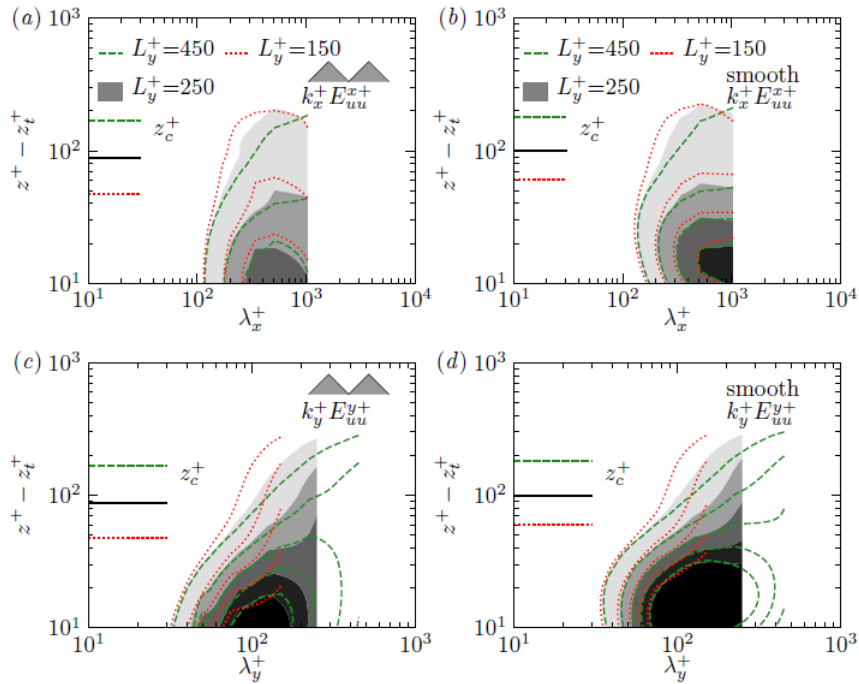
Figure 2.1.8: Unphysical results for turbulent fluctuations in high energy above the height z_c^+. Triangular riblets with three different channel widths and corresponding smooth walls were considered. Pictures are pre-multiplied streamwise (a, b) and spanwise (c, d) spectra of streamwise velocity against distance from the wall with contours from light to dark. (The figure is taken from Endrikat 2020).

28
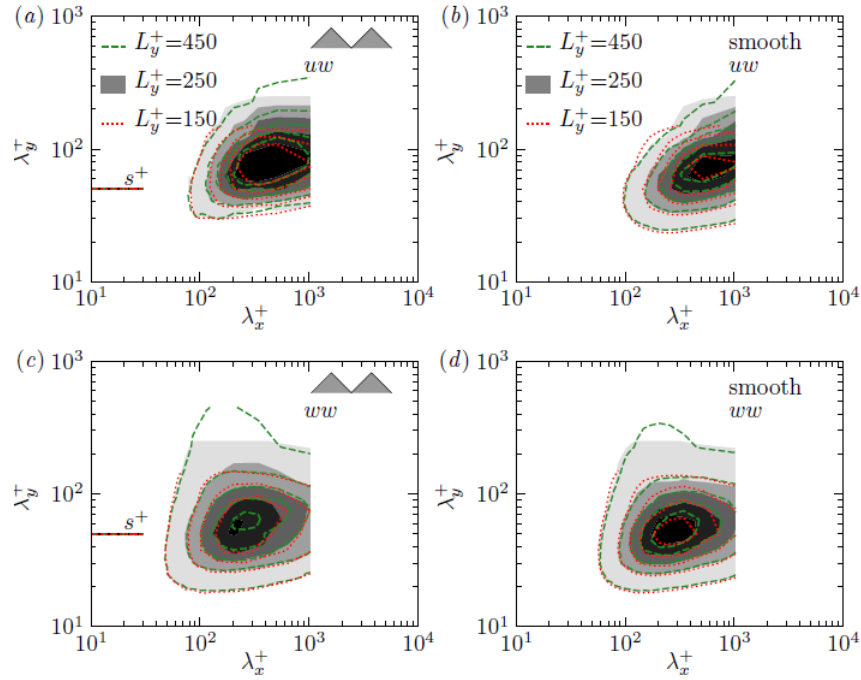
Figure 2.1.9: Pre-multiplied 2D spectra. Triangular riblets for three different channel width and corresponding smooth walls were considered. As a result, velocity fluctuations close to the wall are not affected by the spanwise constraint. (The figure is taken from Endrikat 2020).
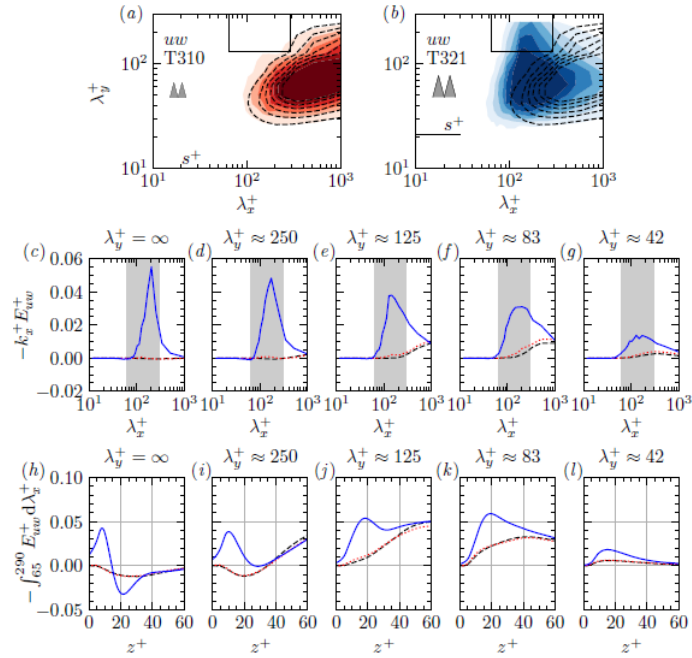
Figure 2.1.10: Spanwise wavelengths affected by KH rollers. We use drag increasing/reducing sharp triangular riblets and smooth walls. (a,b) Pre-multiplied 2D cospectra of Reynolds shear stress in a plane. Open boxes near the top delimit the region of KH rollers ($65 < \lambda_x^+ < 290$, $\lambda_y^+ > 130$). (c-g) Pre-multiplied 1D cospectra of Reynolds shear stress at different spanwise wavelengths. (h-l) Profiles of Reynolds shear stress at different spanwise wavelengths after integrating across the λ_x^+ that are framed in (a,b) and shaded in (c,g). (The figure is taken from Endrikat 2020).

KH dependence on riblet shape
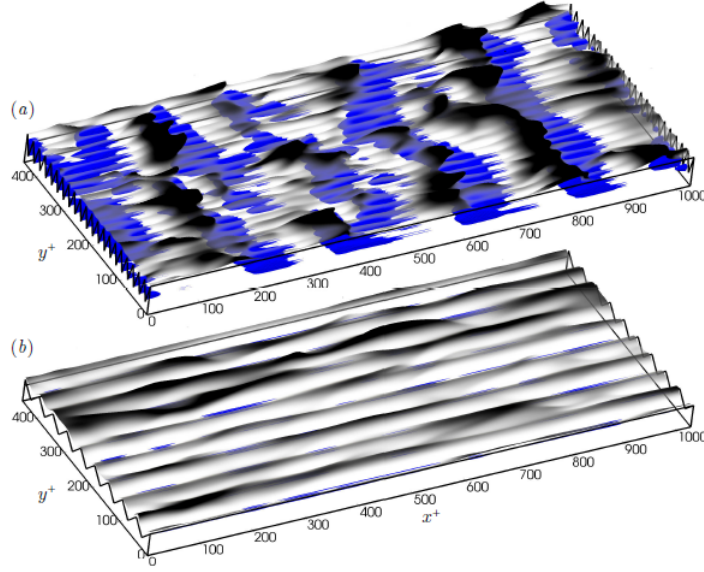
Figure 2.1.11: Flow visualization for two different riblets shape with similar size. KH rollers develop over the triangular riblet with tip angle $\alpha = 30°$ (a) but not over blunt triangular riblets with $\alpha = 90°$ (b). (The figure is taken from Endrikat 2020).

Endrikat 2020 revealed that drag-reducing riblets of any shape have almost the same profile as the smooth wall, because they lack KH rollers. For larger, drag-increasing riblets, differences emerge among riblet shapes. They found that only large sharp-triangular and blade riblets have a KH drag penalty and that they are absent for blunt-triangular and trapezoidal riblets of any size (fig. 2.1.11, 2.1.12). Thus, there is a real dependence of KH rollers on the shape of the riblets.

Furthermore, they considered a momentum integral to decompose the drag-change, in order to quantify if and how KH rollers affect the drag characteristics of a riblet surface:

$$\Delta U^+ = U_s^+ - U^+ = \Delta U_t^+ + \underbrace{\Delta U_{uw}^+}_{\Delta U_{KH}^+ + \Delta U_R^+} \qquad (2.1.1)$$

where

$$
\begin{aligned}
\Delta U_t^+ &= U_s^+\left(z_t^+\right) - U^+\left(z_t^+\right) \\
\Delta U_{uw}^+ &= \int_{z_t^+}^{z_c^+}\left(\frac{\delta_s^+ - z^+}{\delta_s^+} - \frac{\delta'^+ - z^+}{\delta^+}\right) \mathrm{d}z^+ + \int_{z_t^+}^{z_c^+}\left(\overline{u'w'}_s^+ - \overline{u'w'} - \overline{\widetilde{u}\widetilde{w}}^+\right) \mathrm{d}z^+ \\
\Delta U_{KH}^+ &= \int_{z_t^+}^{z_c^+}\left(\overline{u'w'}_{KH,s}^+ - \overline{u'w'}_{KH}^+\right) \mathrm{d}z^+
\end{aligned}
\qquad (2.1.2)
$$

Here, with reference to fig. 2.1.13 z_t^+ is the height of the riblet tips and z_c^+ is the height up to which data are representative of full-span channel flow. The
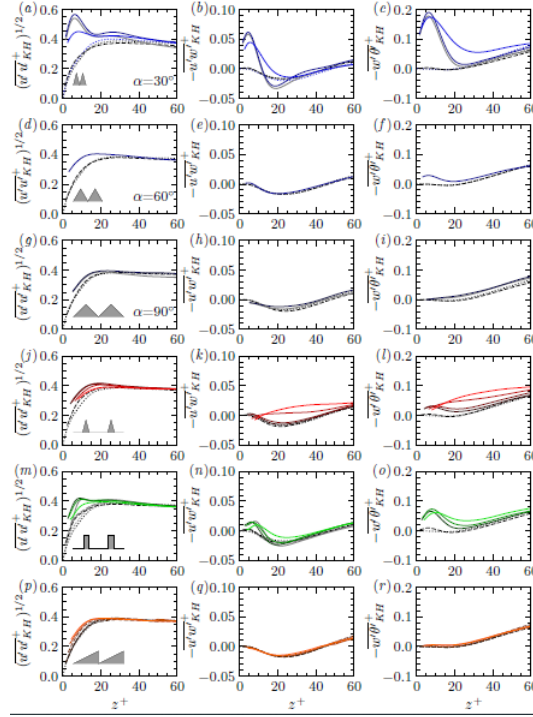
Figure 2.1.12: KH rollers dependence on riblets shape. Profiles of streamwise velocity fluctuations (left), Reynolds shear stress (centre) and the wall-normal transport of θ, i.e. a scalar passive quantity, the temperature, used to visualize turbulent fluctuations (right). KH rollers strongly affect fluctuations in (a-c), (m-o) but not in (p-r). (The figure is taken from Endrikat 2020).
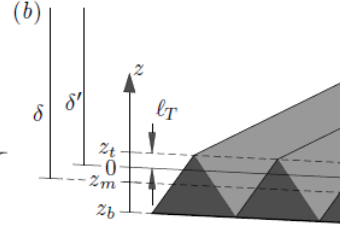
Figure 2.1.13: Geometry of minimal-span ($L_y \ll \delta$) open-channel with triangular riblets close up to the surface. δ is measured from the mean-height z_m and δ' from the virtual origin for turbulence at $z = 0$. Riblet tips are at z_t and the groove bottom is at z_b. (The figure is taken from Endrikat 2020).

subscript s stands for the smooth case. The term ΔU_{uw}^+ includes the difference of total stresses after adjusting the origin. They only considered (fluctuated) Reynold stresses $\overline{u'w'}$ and split them in spectral space into those due to KH rollers $(\overline{u'w'}_{KH}^+)$ and a remainder (subscript R). $\overline{\widetilde{u}\widetilde{w}}^+$ are the dispersive Reynold stresses, that are stremwise invariant for 2D riblets. δ measures the distance between the riblet mean-height and the top of the open channel to match the cross-sectional areas of smooth-wall and riblet channels. δ' is the effective half-channel height, i.e. the distance between the virtual origin and the top of the domain. z is the wall normal direction, where the integration is performed.

Thus, one has to find the drag-change due solely to KH rollers, namely ΔU_{KH}^+.
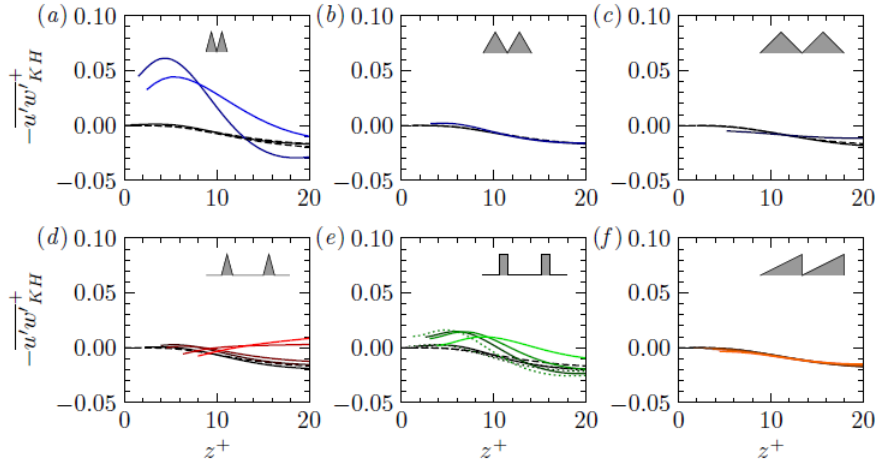
Figure 2.1.14: Profiles of Reynolds shear stress associated with Kelvin Helmholtz rollers as riblet size increases (lighter colours). Smooth-wall profile is dashed. (The figure is taken from Endrikat 2020).
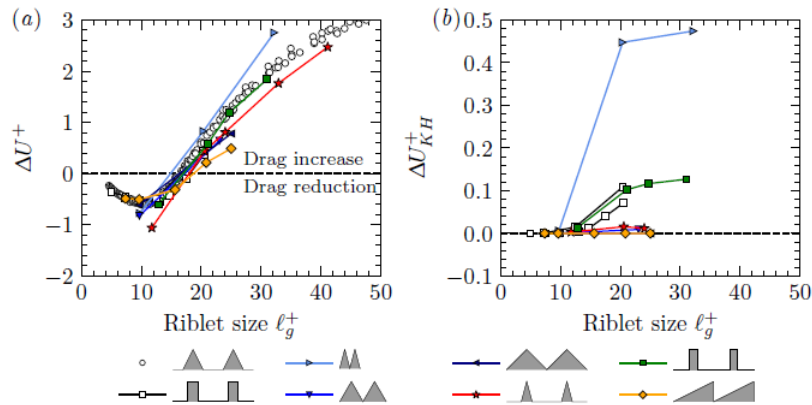
Figure 2.1.15: (a) Total drag-change. (b) Contribution of Kelvin Helmholtz rollers to the drag-change. (The figure is taken from Endrikat 2020).

The flow over blunt triangular and trapezoidal riblets resembles that over a smooth wall in the spectral region associated with KH rollers (fig. 2.1.14). Therefore, there is a negligible drag change (fig. 2.1.15). For sharp triangular and blade riblets, instead, the instability contributes significantly to the drag-change. In particular, drag penalty of KH roller is larger for sharp triangular riblets than for blade riblets. Nevertheless, $\Delta U_{KH}^+ < \Delta U^+$, which means that large riblets increase drag even without KH instability. This suggests the presence of other flow mechanism (maybe groove geometry dependent), like dispersive stresses from secondary flows, that can also contribute to the drag-increase.

Two parameters for KH instability
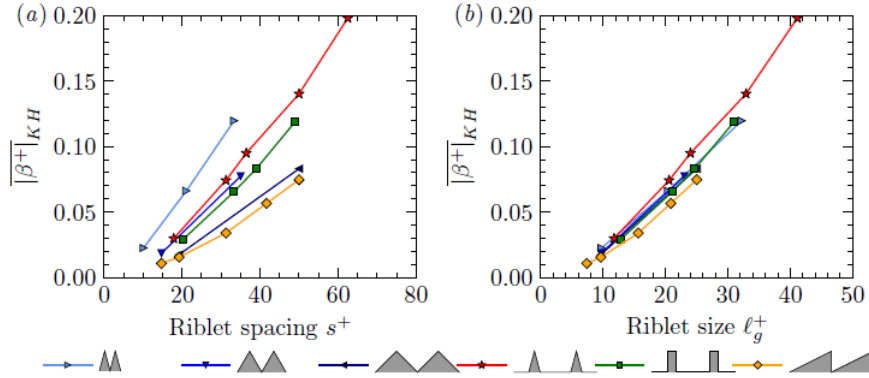
Figure 2.1.16: Porosity/permeability (β) trend against (a) the riblets spacing and (b) the groove size. (The figure is taken from Endrikat 2020).
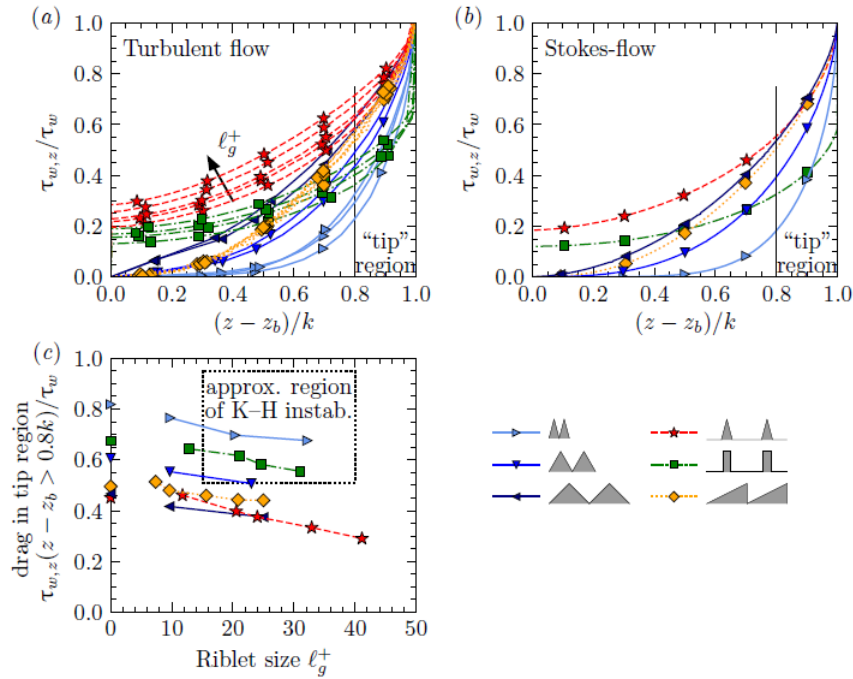
Figure 2.1.17: Wall-shear stress (drag per unit plan area) accumulated from below given heights z relative to the total wall-shear stress, for (a) a turbulent flow (b) 2D Stokes-flows. (c) Fraction of wall-shear stress that acts only on the top 20 % of the riblets. (The figure is taken from Endrikat 2020).

Endrikat 2020 looked for two quantitative parameters:

- for every shapes, the groove area serves as a proxy for wall-normal permeability (which is necessary for KH to develop). This resembles the fact that there is no KH instability for $l_g^+ \lesssim 11$.

  Thus, one parameter is the groove size l_g^+ (fig. 2.1.16).

- A mixing layer with an inflection point of mean-streamwise velocity may be created between slow flow around the roughness elements and

the faster stream above, driving the instability. Only riblet shapes with high momentum absorption at the riblet tips (predicted using Stokes flow) seem to create such a mixing-layer profile. So, wall-shear stress in the tip region describes the ability of the riblet shapes to support KH rollers.

The other parameter is thus 2D Stokes-flow wall-shear stress in the tip region (fig. 2.1.17).

Impermeable boundary   KH rollers do not develop if the plane at the riblet crest is impermeable: shear forces the KH instability, but impermeability suppresses it.

2.1.4 Multi-scale riblets
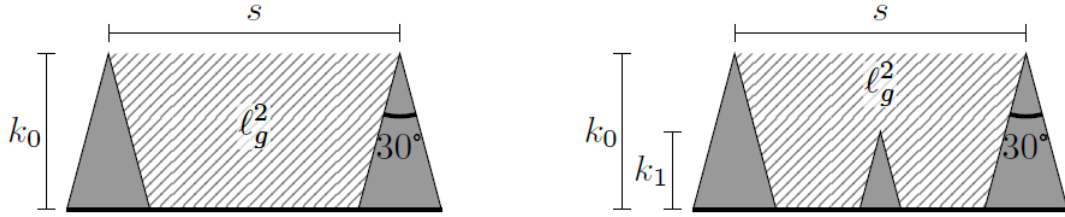
Figure 2.1.18: Schematic of the geometry of (a) the 1-scale trapezoidal riblet and (b) the 2-scale one, with a half height riblet in the centre. (The figure is taken from Endrikat 2020).
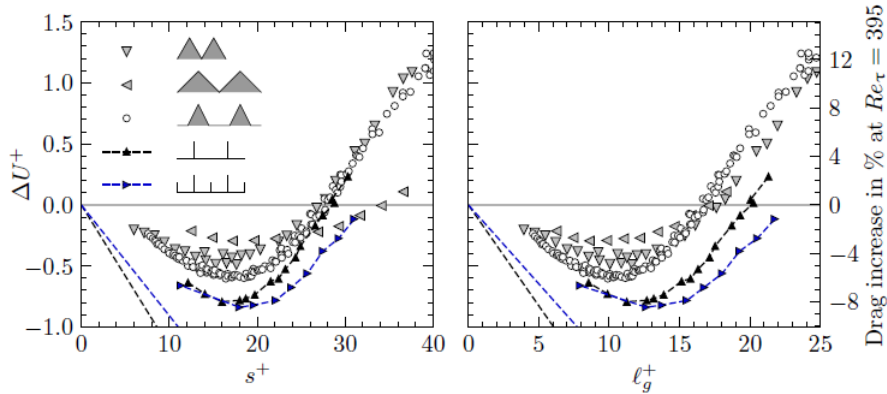
Figure 2.1.19: Drag change curve against both (a) the grooves lateral spacing and (b) the cross-sectional area square-root (b). (The figure is taken from Endrikat 2020).

Then, Endrikat 2020 tried to investigate the effect of multi-scale riblets (i.e. trapezoidal riblets with a half height riblet in the centre, see fig. 2.1.18), generalising the measure of the riblet size for multi scale surfaces.

This is an area that has been analysed also by previous authors. They found that, installing shorter secondary riblets between blades on the surface with the capability to repel eddies of smaller size, there was no significant difference for riblet sizes near the drag-optimum (Bruse et al. 1993) and that for riblet sizes below the optimum multi-scale riblets might degrade the drag-curve (Alinovi, Gribaudo, and Bottaro 2018). But for larger riblets with $l_g^+ \gtrsim 11$, the drag curve suggests a more gentle breakdown of drag reduction with riblet size (fig. 2.1.19).

So, they thought of multi-scale hoping to raise the threshold of s^+ above which there is drag increase, in order to be able to realise larger riblets which anyhow maintain drag reduction capabilities. This would be a great progress in riblet design, since we remember that one of the main fact that raises costs is that usually riblets sizes must be small.

First of all, they observed that s^+ and l_g^+ are not the most appropriate quantities for the size of multi-scale riblet. Indeed, as a "historical" notes, we

should mention that initial drag curves were shown against both the riblet height k^+ and the lateral spacing s^+ (e.g. in Walsh 1982), but soon the spacing prevailed when looking for a length that could describe the riblet size of optimal drag reduction (Bechert et al. 1997). Moreover, it had been found empirically that l_g^+ (the square root of the cross-sectional area of the groove, A_g^+) was a suitable measure of the riblet size, because it captured the size of minimum drag around $l_g^+ \approx 10.7 \pm 1.0$ for different geometries and even reproduced the drag-increasing regime (Garcìa-Mayoral and Jiménez 2011, fig. 2.1.19 b).
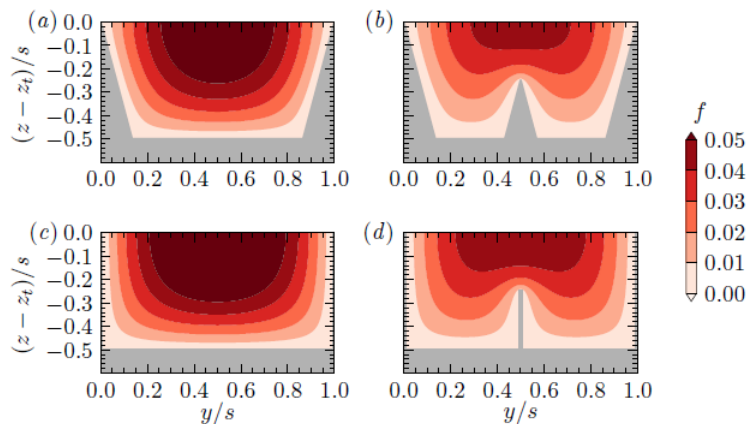
Figure 2.1.20: Visualization of the function f defining Poisson equation to compute L_w for single-scale and two-scale (a,b) trapezoidal riblets and (c,d) blade riblets. (The figure is taken from Endrikat 2020).

The first other quantity that Endrikat 2020 proposed to use is the penetration length L_w^+ that accounts for the groove shape and size. In order to find this length, one needs to solve a Poisson equation that models turbulent fluctuations in the cross-section of the riblet groove:

$$L_w^3 = \frac{1}{s} \int_{A_g} f \; \mathrm{d}A, \quad \text{where}$$

$$\nabla_{yz}^2 f = -1 \quad \text{with} \quad \left.\frac{\mathrm{d}f}{\mathrm{d}z}\right|_t = 0, \quad \text{and} \quad f_w = 0$$

(2.1.3)

Here, the subscripts t and w indicate, respectively, the riblet tips and the wall; s is the dimensional later spacing and f a function defining the problem (see fig. 2.1.20, where it is shown that secondary riblet reduces the values of f and therefore of L_w). We remember that the authors used x, y and z axes to denote, respectively, streamwise, spanwise and wall-normal directions. Endrikat 2020 solved this equation to find L_w in the groove of single-scale and two-scale riblets, as well as of the blade riblets. Endrikat 2020 found that drag curves are much closer when using the new parameter to describe the riblet size (fig. 2.1.21). So, this scale appears to be a suitable description of the riblet size in both the viscous drag-regime and in the post-breakdown regime
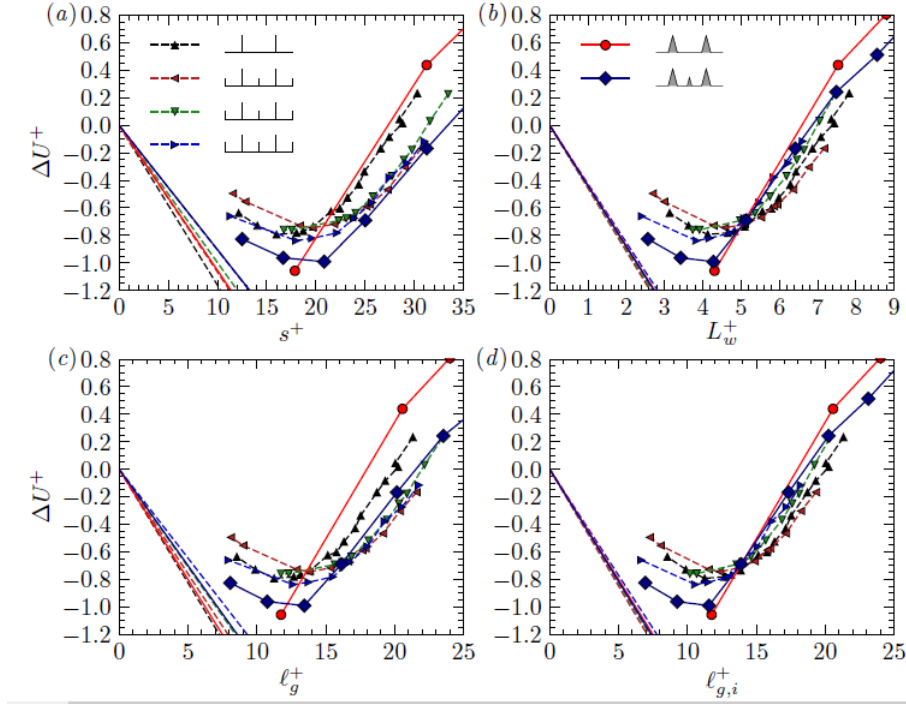
Figure 2.1.21: Drag curves for trapezoidal and blade riblets against different lengths: (a) the riblet spacing s^+, (b) the L_w^+ length, (c) the square-root of the whole groove cross-sectional area l_g^+, (d) the new geometrical length for multi-scale riblets $l_{g,i}^+$. (The figure is taken from Endrikat 2020).

(fig. 2.1.21). Endrikat 2020 also found that there could be a slightly higher drag at the optimum for the two-scale riblet, but the difference is on the same order of magnitude as the statistical uncertainty.

Endrikat 2020 also proposed a different generalisation of L_w^+ for two-scale riblets by interpolating between two extreme cases (without the 2nd riblet - $k_1 = 0$ - and when the 2nd riblet is as big as the 1st - $k_1 = k_0$ -, where k_i is the height of the i-th riblet, starting from 0) to define an interpolated version of the riblet size, namely $l_{g,i}^+$.

When $k_1 = 0$, one has $l_{g,i}^+ = \sqrt{A_g^+}$, whereas, when $k_1 = k_0$, one has $l_{g,i}^+ = \sqrt{A_g^+/2}$. For intermediate ratios of k_1/k_0, Endrikat 2020 linearly interpolated the radicand such that

$$\ell_{g,i} = \sqrt{sk_0 - k_0^2 \tan(\alpha/2) - sk_1/2} \tag{2.1.4}$$

where α is the tip angle of the trapezoidal riblet (authors fixed $\alpha = 30°$). Describing the size of two scale riblets by $l_{g,i}^+$ seems to capture their drag characteristic, because it closely approximates L_w^+ except for a constant factor (fig. 2.1.21). Conveniently, $l_{g,i}^+$ is a geometrical length found without having to solve the Poisson equation (fig. 2.1.21).

In the end, Endrikat 2020 finds that, despite half-sized riblets in the groove further reduce drag at a fixed riblet spacing, there is no real benefit in terms
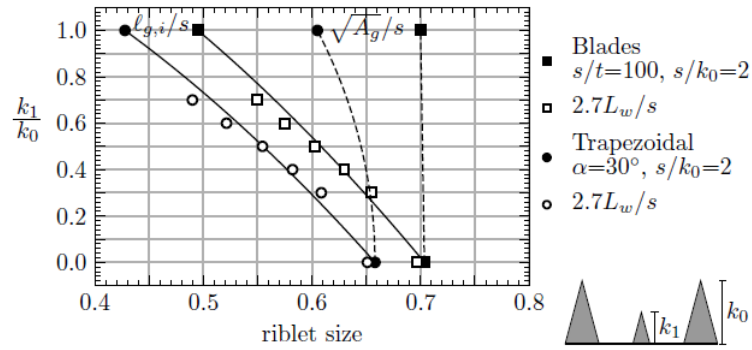
Figure 2.1.22: Definition of the riblet size $l_{g,i}$ for two-scale trapezoidal and blade riblets compared to l_g. (The figure is taken from Endrikat 2020).

of the lowest attainable drag in comparison to one-scale riblets, as they obtained the same drag curve in the post-optimum regime (once considered the appropriate length to define the riblet size, fig. 2.1.21).

Conclusion

In conclusion, since drag reduction breaks down for widely spaced riblets even in the absence of drag-increasing KH rollers, they suggested to delay the beginning of other mechanism that can raise drag (e.g. form-induced Reynold stresses due to secondary flows).

2.2   Anisotropic permeable substrates

We now describe the case of anisotropic permeable substrates, as treated by Chavarin et al. 2021. At first we will describe the general framework and quote the main results, then we will give some details about the approach used by the authors.

2.2.1   Main framework and results

There is evidence that anisotropic permeable substrates can suppress the dynamically-important near-wall (NW) cycle and consequently lead to drag reduction in wall-bounded turbulent flows (up to 25%) by correctly tuning streamwise and spanwise permeability.

The mechanism for such a reduction is the same that occurs for the riblets case, i.e. an offset in the virtual origin felt by the mean flow (due to the streamwise permeability) and by the turbulent fluctuations (due to the spanwise permeability). This offset weakens the quasi-streamwise vortices and further reduces turbulent momentum transfer, leading to a decrease in skin friction. Drag reduction is further limited by the appearance of KH rollers, due to a relaxation in the wall normal permeability.

Authors used a *resolvent formulation* (see McKeon and Sharma 2010; McKeon 2017) to study the effect of such substrates.

They considered the Fourier-Transformed Navier-Stokes equations as a linear forcing-response system, in which the non-linear terms represent an endogenous forcing that gives rise to a velocity and pressure response.

In order to correctly model the effect of the permeable substrates, they used a combination of the Volume-Averaged Navier-Stokes equations and of Darcy's law. As far as geometry is concerned, they chose a symmetric channel geometry at friction Reynold number $Re_\tau = 180$ and substrates with $K_y^+ = K_z^+$. Within this framework, they identified a *resolvent operator* (i.e. the forcing-response transfer function which maps non-linear forcing to the velocity and pressure response), whose gain-based decomposition leads to the identification of *response modes* across spectral space, which reproduce important structural and statistical features of the wall bounded turbulent flow. So, in first approximation, while trying to control the system, one can take into consideration only the variations of these resolvent modes instead of the ones experienced by the full turbulent flow field.

Substrates with high streamwise permeability and low spanwise permeability are found to suppress the mode gain, leading to a drag reduction, which is limited by the appearance of KH rollers beyond a threshold value of the wall-normal permeability (fig. 2.2.2, 2.2.3).
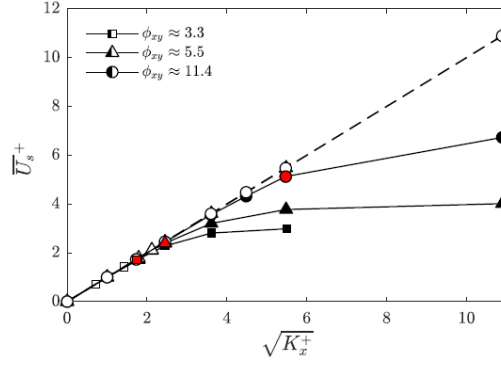
Figure 2.2.1: Predicted slip velocity as a function of streamwise permeability $\sqrt{K_x^+}$. Closed symbols are the DNS from Gòmez-de-Segura and Garcìa-Mayoral 2019. Open symbols are the resolvent prediction made by using a synthetic eddy viscosity model. (The figure is taken from Chavarin et al. 2021).
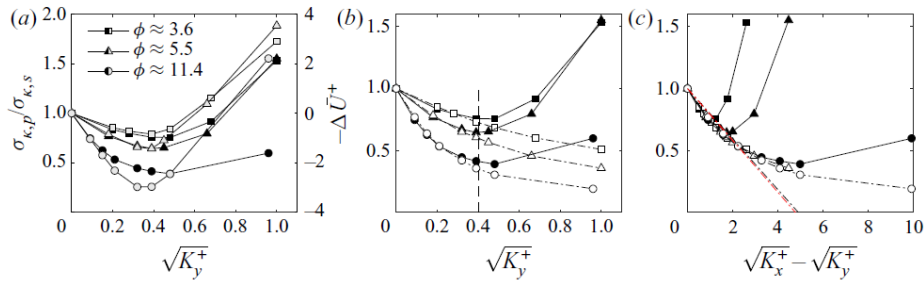
Figure 2.2.2: Predictions for the NW resolvent mode. (a) Normalized mode gains (velocity profile by DNS) vs DNS result from Gòmez-de-Segura and Garcìa-Mayoral 2019, as a function of $\sqrt{K_y^+}$. (b) Normalized mode gains with velocity profile by DNS vs synthetic velocity profile as a function of $\sqrt{K_y^+}$. (c) Normalized mode gains with velocity profile by DNS vs synthetic velocity profile as a function of $\sqrt{K_x^+} - \sqrt{K_y^+}$. Remember that in this model $\sqrt{K_y^+} = \sqrt{K_z^+}$, so that $\sqrt{K_x^+} - \sqrt{K_y^+} = \sqrt{K_x^+} - \sqrt{K_z^+}$. (The figure is taken from Chavarin et al. 2021).

In particular, the gain for the single resolvent mode reproduces the initial drag reduction trend, which is proportional to

$$\sqrt{K_x^+} - \sqrt{K_z^+} \tag{2.2.1}$$

where $\sqrt{K_x^+}$ and $\sqrt{K_z^+}$ are, respectively, the streamwise and spanwise permeability length scale (fig. 2.2.2).

Moreover, the resolvent-based formulation can predict conditions in which rollers emerge (complementary to the slip-length based arguments used in the previous section). This is because the gain for the resolvent mode can serve as a proxy for the total drag reduction. In particular, in previous studies riblet geometries reducing drag are found to reduce the forcing-response gain for the NW resolvent mode in comparison to the smooth wall case.

The resolvent-based prediction is the following:

- the difference between the two permeability length scale can lead to a
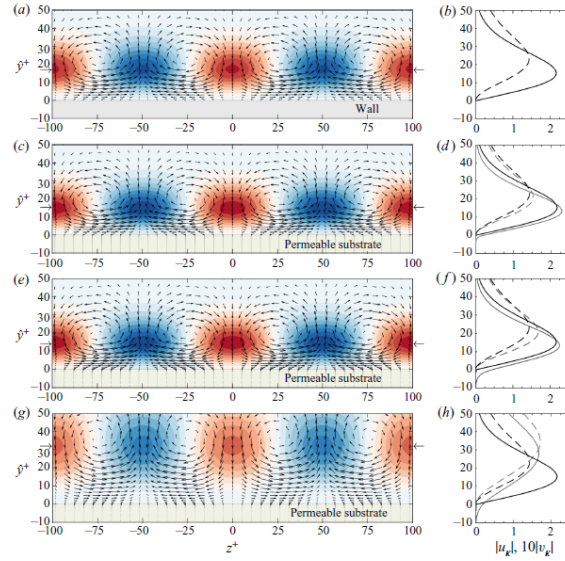
Figure 2.2.3: NW mode structure predictions made using the DNS velocity profiles for (a,b) the smooth-wall case and for (c,d,e,f) the substrates for different values of ϕ_{xy} and $\sqrt{K_y^+}$. ϕ_{xy} is the anisotropy ratio: $\phi_{xy} = \sqrt{K_x^+}/\sqrt{K_y^+}$. (sx) Red and blue contours are, respectively, positive and negative streamwise velocity. (dx) the solid lines is the streamwise velocity while the dashed lines is the wall-normal velocity. The black lines represent the smooth-wall case, while the gray lines represent the permeable substrates. (The figure is taken from Chavarin et al. 2021).

wall-normal compression of the streamwise vortices, which limits the energy extraction from the mean flow (fig. 2.2.3).

- for $\sqrt{K_y^+} \gtrsim 0.4$ energetic rollers with streamwise wavelenght $\lambda_x^+ \approx 150$ can emerge (fig. 2.2.4).

The main weakness of this model is the requirement of the mean velocity profile over the substrates, considering that no model or data is available for the case of such substrates.

In particular, the use of a different profile can significantly affect the gain prediction: when drag performance deteriorates ($\sqrt{K_y^+} \gtrsim 0.4$), important differences are present between the DNS by Gòmez-de-Segura and Garcìa-Mayoral 2019 and the resolvent prediction made by using a synthetic eddy viscosity model (fig. 2.2.1), since the latter assumes turbulence always to be smooth-wall like and not to penetrate the substrates (which, indeed, it does, with rollers that penetrate the rough wall).

However, it is important to notice that, even with the synthetic mean profile, resolvent analysis does show the emergence of KH rollers for $\sqrt{K_y^+} \gtrsim 0.4$, and thus it can generate useful *a priori* prediction even in this case (fig. 2.2.4, 2.2.5, 2.2.6).
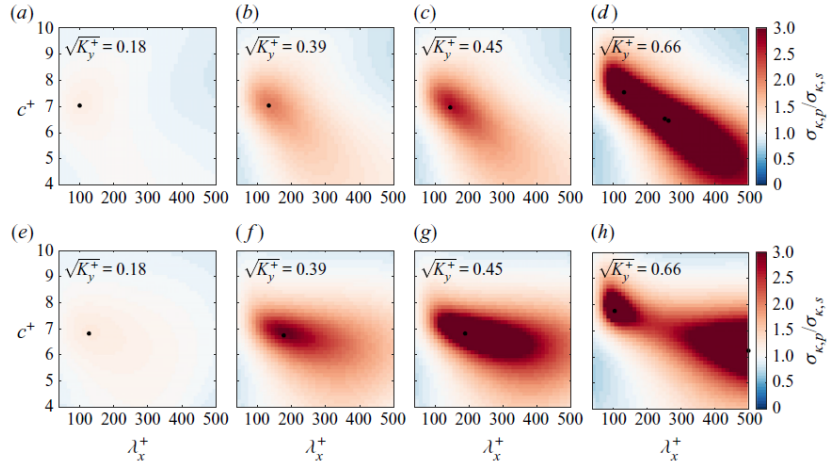
Figure 2.2.4: Normalized gain for spanwise-coherent structures plotted as a function of streamwise length λ_x^+ and wave speed c^+. These predictions make use of the synthetic mean profile. Red and blue shading respectively represent mode amplification and suppression. Structures with the largest amplification are labelled with a (●) marker (The figure is taken from Chavarin et al. 2021).
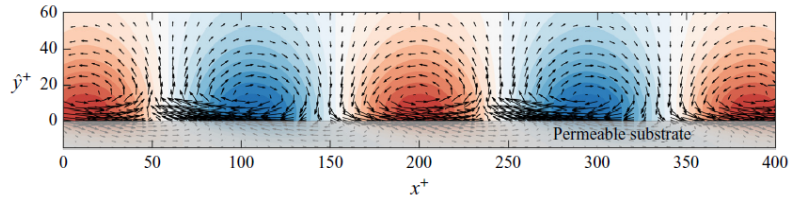
Figure 2.2.5: Flow structure associated with the most amplified spanwise-constant resolvent mode over the permeable substrate (see fig. 2.2.4). The red and blue shaded contours show regions of positive and negative pressure. (The figure is taken from Chavarin et al. 2021).
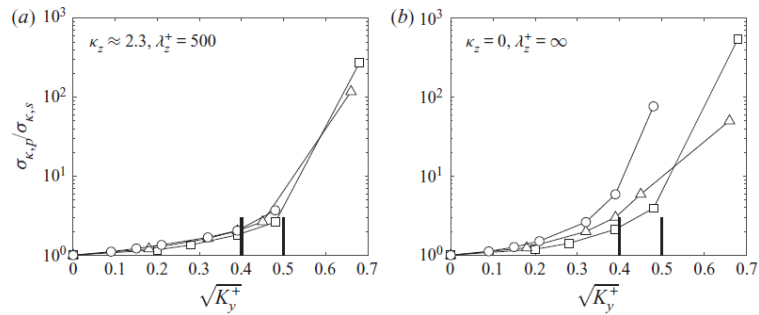
Figure 2.2.6: Comparison of resolvent-based gain predictions for spanwise-coherent structures with different anisotropy ratios: the maximum normalized gain obtained for resolvent modes is shown as a function of wall-normal permeability for different values of λ_z^+. All of these predictions were obtained using the synthetic mean profiles. (The figure is taken from Chavarin et al. 2021).

2.2.2 The Resolvent-Based Formulation

In this subsection, we provide a more deep explanation of the method used by Chavarin et al. 2021.

Permeable Substrates Chavarin et al. 2021 started from the Volume-Averaged (VA) Navier-Stokes (NS) equations, that give rise to two additional terms: the sub-filter scale stresses and a surface filter term. In order to find a suitable closure for the model, they parameterized the flow resistance using the Darcy permeability tensor (with the Forchheimer correction term for inertial effects). The equations governing the motion are thus

$$\frac{\partial \langle \boldsymbol{u} \rangle}{\partial t} + \frac{1}{\varepsilon} \boldsymbol{\nabla} \cdot (\varepsilon \langle \boldsymbol{u} \rangle \langle \boldsymbol{u} \rangle + \varepsilon \boldsymbol{\tau}) = -\frac{1}{\varepsilon} \boldsymbol{\nabla}(\varepsilon \langle p \rangle) + \frac{1}{\varepsilon Re_\tau} \boldsymbol{\nabla}^2 (\varepsilon \langle \boldsymbol{u} \rangle) - \frac{\varepsilon}{Re_\tau} \boldsymbol{K}^{-1} (\boldsymbol{I} + \boldsymbol{F}) \langle \boldsymbol{u} \rangle,$$

$$\boldsymbol{\nabla} \cdot (\varepsilon \langle \boldsymbol{u} \rangle) = 0$$

(2.2.2)

with ε the porosity of the medium, $\boldsymbol{K}$ the dimensionless permeability tensor, $\boldsymbol{F}$ the dimensionless Forchheimer resistance tensor, $\langle \cdot \rangle$ the volume averaging operation, $\langle \boldsymbol{u} \rangle$ the dimensionless velocity, $\langle p \rangle$ the dimensionless pressure and t the dimensionless time. The normalisation has been carried out with the channel half-height h and the friction velocity u_τ. The friction Reynold number is given by $Re_\tau = u_\tau h / \nu$ and $\boldsymbol{K}$ is defined by $\boldsymbol{K} = \boldsymbol{K}^\dagger / h^2$, with $\boldsymbol{K}^\dagger$ is the dimensional permeability. Finally, $\tau = \langle \boldsymbol{uu} \rangle - \langle \boldsymbol{u} \rangle \langle \boldsymbol{u} \rangle$ is the sub-filter scale stresses.

Than, they did the following simplifications:

- they considered a diagonal permeability tensor, $\boldsymbol{K} = diag(K_x, K_y, K_z)$, with equal wall-normal and spanwise permeability, $K_y = K_z$. This is equivalent to align the principal directions (or axes) of the tensor with the streamwise, wall-normal and spanwise directions of the flow.

- they omitted the non linear Forchheimer correction term. This is because inertial effect are small.

- in order to maximize any potential drag reduction, they set the porosity of permeable substrates to be $\varepsilon \approx 1$.

- they neglected the sub-filter scale stresses, since they are mainly interested in structures such as NW cycle and KH rollers, which are much larger than the characteristic length scale of the porous medium.

The equations thus reduce to

$$\frac{\partial \langle \boldsymbol{u} \rangle}{\partial t} + \boldsymbol{\nabla} \cdot (\boldsymbol{uu}) = -\boldsymbol{\nabla}(p) + \frac{1}{Re_\tau} \boldsymbol{\nabla}^2 (\boldsymbol{u}) - \frac{1}{Re_\tau} \boldsymbol{K}^{-1} \boldsymbol{u},$$
$$\boldsymbol{\nabla} \cdot \boldsymbol{u} = 0$$

(2.2.3)

where the $\langle \cdot \rangle$ symbol has been omitted.

Figure 2.2.7 shows the geometry of the system: the unobstructed region is for $y \in [-1, 1]$, the permeable substrates are for $y \in [-(1 + H), -1]$ and $y \in [1, 1 + H]$. The "height" of the permeable substrate is H, as all lengths have been normalized by the channel half-height h.
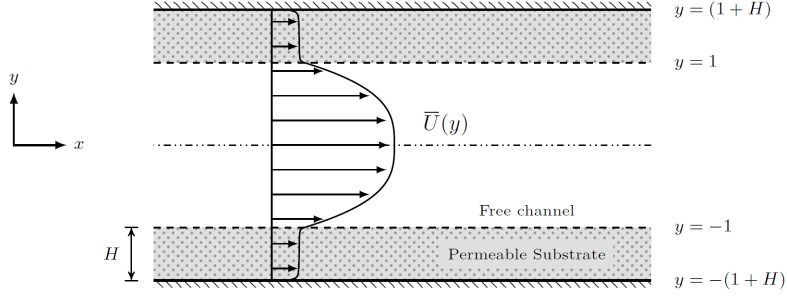
Figure 2.2.7: System geometry: symmetric channel flow configuration. (The figure is taken from Chavarin et al. 2021).

Resolvent Analysis Now, a standard Reynolds-decomposition is taken.

The velocity and the pressure field are decomposed into a time-averaged component and a fluctuating one: $\boldsymbol{u}(t, \mathbf{x}) = \overline{\boldsymbol{U}}(\mathbf{x}) + \boldsymbol{u}'(t, \mathbf{x})$ with $\overline{\boldsymbol{U}}(\mathbf{x}) = [\overline{U}(y), 0, 0]^T$ and $p(t, \mathbf{x}) = \overline{P}(\mathbf{x}) + p'(t, \mathbf{x})$.

Then, the velocity and pressure *fluctuation* are Fourier-transformed in streamwise and spanwise directions and in time:

$$\begin{bmatrix} \boldsymbol{u}'(t, \mathbf{x}) \\ p'(t, \mathbf{x}) \end{bmatrix} = \iiint \begin{bmatrix} \boldsymbol{u}_{\boldsymbol{\kappa}}(y) \\ p_{\boldsymbol{\kappa}}(y) \end{bmatrix} \exp\left(-\mathrm{i}\omega t + \mathrm{i}\kappa_x x + \mathrm{i}\kappa_z z\right) \mathrm{d}\omega \mathrm{d}\kappa_x \, \mathrm{d}\kappa_z \quad (2.2.4)$$

where κ_x is the streamwise wavenumber, κ_z the spanwise wavenumber and ω the frequency. $\boldsymbol{u}_{\boldsymbol{\kappa}}$ and $p_{\boldsymbol{\kappa}}$ are the Fourier coefficients for the velocity and pressure field at a given wavenumber-frequency combination $\boldsymbol{\kappa} = (\kappa_x, \kappa_z, \omega)$.

Doing this, the initial equations can be expressed as

$$\begin{bmatrix} \boldsymbol{u}_{\boldsymbol{\kappa}} \\ p_{\boldsymbol{\kappa}} \end{bmatrix} = \left(-\mathrm{i}\omega \begin{bmatrix} \boldsymbol{I} \\ 0 \end{bmatrix} - \begin{bmatrix} \boldsymbol{\mathcal{L}}_{\boldsymbol{\kappa}} & -\tilde{\nabla} \\ -\tilde{\nabla}^T & 0 \end{bmatrix}\right)^{-1} \begin{bmatrix} \boldsymbol{I} \\ 0 \end{bmatrix} \boldsymbol{f}_{\boldsymbol{\kappa}} = \boldsymbol{\mathcal{H}}_{\boldsymbol{\kappa}} \boldsymbol{f}_{\boldsymbol{\kappa}} \quad (2.2.5)$$

where the operator $\boldsymbol{\mathcal{L}}_{\boldsymbol{\kappa}}$ is shown below

$$\boldsymbol{\mathcal{L}}_{\boldsymbol{\kappa}} = \begin{bmatrix} -\mathrm{i}\kappa_x \overline{U} + Re_\tau^{-1}\left(\tilde{\nabla}^2 - \boldsymbol{K}^{-1}\right) & -\frac{\mathrm{d}\overline{U}}{\mathrm{d}y} & 0 \\ 0 & -\mathrm{i}\kappa_x \overline{U} + Re_\tau^{-1}\left(\tilde{\nabla}^2 - \boldsymbol{K}^{-1}\right) & 0 \\ 0 & 0 & -\mathrm{i}\kappa_x \overline{U} + Re_\tau^{-1}\left(\tilde{\nabla}^2 - \boldsymbol{K}^{-1}\right) \end{bmatrix}$$
$$(2.2.6)$$

In this definition, $\boldsymbol{f_\kappa}$ is the Fourier coefficient for the non-linear term and $\tilde{\boldsymbol{\nabla}} = (i\kappa_x, \frac{\partial}{\partial y}, i\kappa_z)$, $\tilde{\boldsymbol{\nabla}}^T$ and $\tilde{\boldsymbol{\nabla}}^2 = (-\kappa_x^2 - \kappa_z^2 + \frac{\partial^2}{\partial y^2})$ are the Fourier-transformed, respectively, gradient, divergence and laplacian operators. The velocity and pressure response at a given $\boldsymbol{\kappa}$ constitute a traveling wave flow field with, respectively, streamwise and spanwise wavelenght $\lambda_x = 2\pi/\kappa_x$ and $\lambda_z = 2\pi/\kappa_z$ that is moving downstream at speed $c = \omega/\kappa_x$.

The transfer function that maps the non linear forcing $\boldsymbol{f_\kappa}$ to the velocity and pressure response is the resolvent operator $\boldsymbol{\mathcal{H}_\kappa}$.

A SVD (singular value decomposition) of $\boldsymbol{\mathcal{H}_\kappa}$ is performed in order to find a set of orthonormal response modes, ordered based on their gain (under an L^2 energy norm). In order to do this, the resolvent operator is first scaled as

$$\boldsymbol{W_u u_\kappa} = \boldsymbol{\mathcal{H}_\kappa^w W_f f_\kappa} \tag{2.2.7}$$

where we have defined $\boldsymbol{\mathcal{H}_\kappa^w} = \boldsymbol{W_u \mathcal{H}_\kappa W_f^{-1}}$ (the superscript w is present to remind to $\boldsymbol{W_u}$ and to $\boldsymbol{W_f^{-1}}$), with $\boldsymbol{W_u}$ and $\boldsymbol{W_f}$ that incorporate numerical quadrature weights for the entire domain. Finally, the SVD leads to

$$\boldsymbol{\mathcal{H}_\kappa^w} = \sum_m \psi_{\boldsymbol{\kappa},m} \sigma_{\boldsymbol{\kappa},m} \phi_{\boldsymbol{\kappa},m}^\dagger \tag{2.2.8}$$

where

$$\sigma_{\boldsymbol{\kappa},1} > \sigma_{\boldsymbol{\kappa},2} > \cdots > 0, \quad \psi_{\boldsymbol{\kappa},l}^\dagger \psi_{\boldsymbol{\kappa},m} = \delta_{lm}, \quad \phi_{\boldsymbol{\kappa},l}^\dagger \phi_{\boldsymbol{\kappa},m} = \delta_{lm} \tag{2.2.9}$$

yielding forcing modes $\boldsymbol{f_{\kappa,m}} = \boldsymbol{W_f^{-1}} \phi_{\boldsymbol{\kappa},m}$ and velocity responses $\boldsymbol{u_{\kappa,m}} = \boldsymbol{W_u^{-1}} \psi_{\boldsymbol{\kappa},m}$ of unit total energy over the entire domain, i.e.

$$\int_{-(1+H)}^{(1+H)} \boldsymbol{u_{\kappa,l}^\dagger u_{\kappa,m}} dy = \delta_{lm}, \quad \int_{-(1+H)}^{(1+H)} \boldsymbol{f_{\kappa,l}^\dagger f_{\kappa,m}} dy = \delta_{lm} \tag{2.2.10}$$

The resolvent framework allows to find that $\boldsymbol{\mathcal{H}_\kappa}$ tends to low-rank at κ combinations that are energetic in wall-bounded turbulent flows. So, since usually the first singular value is an order of magnitude larger than subsequent singular values, i.e. $\sigma_{\boldsymbol{\kappa},1} \gg \sigma_{\boldsymbol{\kappa},2} > \cdots$, the resolvent operator can be well approximated using a rank-1 truncation:

$$\boldsymbol{\mathcal{H}_\kappa^w} \approx \psi_{\boldsymbol{\kappa},1} \sigma_{\boldsymbol{\kappa},1} \phi_{\boldsymbol{\kappa},1}^\dagger \tag{2.2.11}$$

Forcing in the direction of the first forcing mode $\boldsymbol{f_{\kappa,1}} = \boldsymbol{W_f^{-1}} \phi_{\boldsymbol{\kappa},1}$ generates a velocity response $\boldsymbol{u_{\kappa,1}} = \boldsymbol{W_u^{-1}} \psi_{\boldsymbol{\kappa},1}$ that is amplified by a factor $\sigma_{\boldsymbol{\kappa},1}$. So, under the L^2 norm, $\sigma_{\boldsymbol{\kappa},1}^2$ is a measure of energy amplification.

The authors now concentrate to evaluate the effect of anisotropic permeable substrates on the rank-1 resolvent mode that serves a proxy for the NW cycle. A reduction in gain is interpreted as mode suppression, indicating drag reduction. Furthermore, they also try to predict the appearing of KH rollers.

Boundary Conditions The resolvent operator is discretized using spectral discretization and rectangular block matrices.
We can thus use two different sets of equations in the unobstructed region and in porous domain and couple the two via appropriate interfacial conditions:

- no-slip boundary conditions at the lower and upper substrates wall, $y = \pm(1 + H)$

- continuity in the velocity and pressure field at the interfaces between the porous medium and the unobstructed flow, $y = \pm 1$

- continuity in the streamwise and spanwise shear at the interface

$$
\begin{aligned}
\boldsymbol{u} &= 0 && \text{at} \quad y = \pm(1 + H), \\
\boldsymbol{u}|_{y_+} &= \boldsymbol{u}|_{y_-} \quad \text{and} \quad p|_{y_+} = p|_{y_-} && \text{at} \quad y = \pm 1,
\end{aligned}
$$

$$
\left.\frac{\partial u}{\partial y}\right|_{y_+} = \left.\frac{1}{\varepsilon}\frac{\partial u}{\partial y}\right|_{y_-} \text{and} \left.\frac{\partial w}{\partial y}\right|_{y_+} = \left.\frac{1}{\varepsilon}\frac{\partial w}{\partial y}\right|_{y_-} \text{at} \quad y = -1, \tag{2.2.12}
$$

$$
\left.\frac{\partial u}{\partial y}\right|_{y_-} = \left.\frac{1}{\varepsilon}\frac{\partial u}{\partial y}\right|_{y_+} \quad \text{and} \quad \left.\frac{\partial w}{\partial y}\right|_{y_-} = \left.\frac{1}{\varepsilon}\frac{\partial w}{\partial y}\right|_{y_+} \quad \text{at} \quad y = 1,
$$

where y_+ and y_- denotes the values taken on either side of the porous substrate-unobstructed flow interface.

Mean Velocity Profile In order to use this construction, the knowledge of the mean profile velocity $\overline{U}(y)$ is required. Here, they used two different methods to generate the mean profile:

- using DNS results by Gòmez-de-Segura and Garcìa-Mayoral 2019

- using a synthetic eddy viscosity profile

As far as the second method is concerned, they proposed the following equation

$$
\frac{1}{Re_\tau}\left((1 + \nu_e)\frac{\mathrm{d}^2}{\mathrm{d}y^2} + \frac{\mathrm{d}\nu_e}{\mathrm{d}y}\frac{\mathrm{d}}{\mathrm{d}y} - \frac{1}{K_x}\right)\overline{U} = \frac{d\overline{p}}{dx} \tag{2.2.13}
$$

which was solved numerically to obtain $\overline{U}(y)$. Here, ν_e is the eddy viscosity, parametrized as

$$
\nu_e = \begin{cases} \frac{1}{2}\left[1 + \left\{\frac{c_2 Re_\tau}{3}\left(2y - y^2\right)\left(3 - 4y + 2y^2\right) \right. \right. \\ \qquad\qquad\qquad\qquad\qquad\qquad \left. \left. \times \left(1 - \exp\left((|y-1|-1)\frac{Re_\tau}{c_1}\right)\right)\right\}^2\right]^{1/2} - \frac{1}{2}, & |y| \leqslant 1 \\ 0, & |y| > 1 \end{cases}
$$

$$(2.2.14)$$

where they set $c_1 = 46.2$ and $c_2 = 0.61$.

This model assumes that turbulence does not penetrate into the porous medium. In reality, it does penetrate, depending on K_y and K_z.

Numerical Discretization The resolvent operator and the equations for the mean velocity profile are discretized in the wall-normal direction using spectral discretization and rectangular block matrices (i.e. using Chebyscev polynomials). We will not go into such details.

Conclusion Resolvent analysis is a useful design tool for pursuing formal optimisation of complex permeable substrates. The method could also be useful to evaluate the effect of porous materials for other applications than drag reduction or to provide insight into environmental flows over granular beds and vegetation canopies. In order to refine the model, one could see how the inclusion of inertial effect or more complex boundary conditions is likely to affect control performance.

2.3 An experiment inspired by pufferfish skin

Here we report an experiment made by Zhou et al. 2021 with the aim to investigate the drag reduction effects of pufferfish skin. We will not focus on the details of the experimental procedure, opting for briefly describing it and then mentioning the main results obtained by the authors.
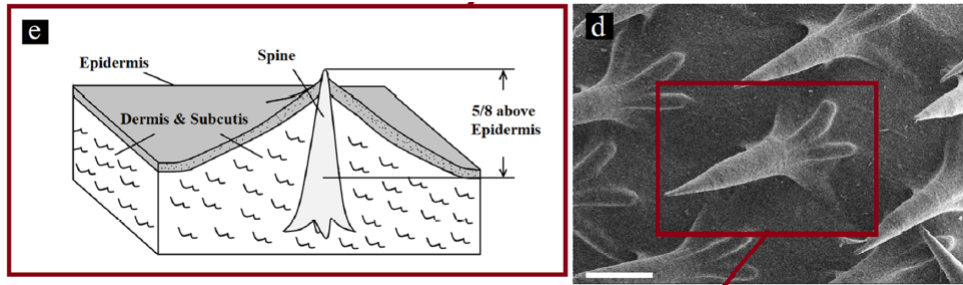
Figure 2.3.1: (sx) Schematic of the protusion. (dx) SEM image that shows the structure of typical spines of the pufferfish (the white scale bar represents $500\,\mu m$). (The figure is taken from Zhou et al. 2021).

Introduction As previously mentioned, perfectly smooth surfaces do not exist in nature. Indeed, rough surfaces are the norm, not the exception, since they can confer much benefit, including drag reduction capabilities. For example, it seems that the incredible hydro-dynamical performances of sharks, primarily their speed and flexibility, are in part due to the denticles covering their dermis, featuring riblet-like micro-indentations. As seen in the previous sections, riblet structures are considered an effective passive method of drag reduction. However, there are several practical issues that limit their applicability, such as the accumulation of ice or dirt. In this section, we will thus consider surfaces with protusions, which also possess drag reduction capabilities without the practical issues of riblets, since, for example, they can hinder dust accumulation provided to enlarge their size. However, one has to study carefully the general conditions of the flow and the geometry of such protusions in order to realize a rough surface with a good drag reduction power within the real fluid-dynamical conditions of interest.

The work we are going to expose proposes to identify and to highlight the role of the correct geometrical and fluid-dynamical parameters one has to take into consideration in order to achieve optimum drag reduction while developing a rough surface with protrusions. The natural counterpart they considered was pufferfish skin.

Pufferfish skin is known for its spine-covered (instead of scales) surface (see fig. 2.3.1). These unique protusions have not only a protective function but also an hydro-dynamical one, contributing to drag reduction. Indeed, this fish shows an excellent physical capability to survive in the ocean: its burst speed is of $\sim 3.5\,BL/s$ (body length per second) despite the difficulty for

a swimming fish to exceed $\sim 1\,BL/s$, thus suggesting for a drag reduction mechanism.
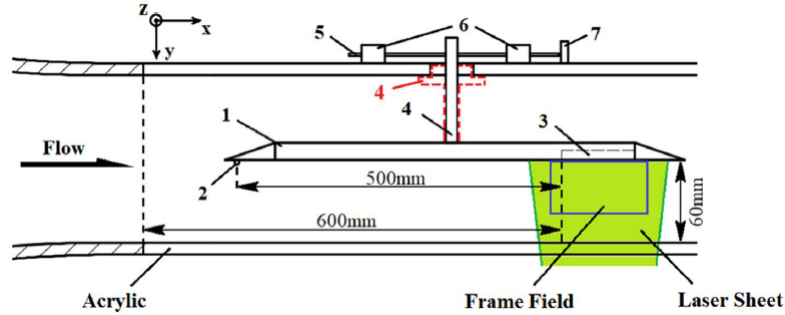
Figure 2.3.2: Schematic of the experimental apparatus. **1** Test plate; **2** steel trip; **3** sample; **4** connector; **5** slender rod; **6** sliders; **7** force sensor. (The figure is taken from Zhou et al. 2021).

(Brief) Description of the Experiment The authors designed and manufactured (by 3D printing) a flat sample and six samples featuring biomimetic spine-covered protusions (BSCPs) with combinations of three different protusion heights (0.2, 0.4, 0.8 mm) and two array patterns (averaged and staggered). In a circulating water tunnel laboratory they introduced force measurements and PIV (particle image velocimetry) with a free-stream velocity of $0.65\,m/s \approx 2.43\,km/h$, which is consisted with pufferfish swimming velocity (see fig. 2.3.2 for an idea). From the former they took drag reduction ratio (defined as $DR = \frac{D_{rough} - D_{flat}}{D_{flat}}$), while from the latter they considered Reynolds shear stress (RSS) and turbulent intensity (TKE). Further, they considered vortex structures within the turbulent boundary layer and then investigated coherent structures benefiting drag reduction.

Main results First of all, they identified two parameters that influences drag reduction power: height and array pattern. However, also Reynold number and the spacing scale were found to be influential factors, but the authors focused on the previous two.

Indeed, as far as the force measurements are concerned (see fig. 2.3.3), the staggered array was superior with respect to the averaged one because it showed a higher drag reduction ratio, with maximum drag reduction of 5.9 % for the sample with the shortest BSCPs (sample E). This agrees with the spine array of pufferfish skin. Furthermore, higher elements cause more drag. However, the growth rate was decreased, suggesting a limitation in this trend.

As far as PIV is concerned (see 2.3.4), the staggered array also achieved lower Reynolds shear stress and turbulence intensity than the averaged one. Sample E decelerates the development of turbulence in the wall-normal direction

49
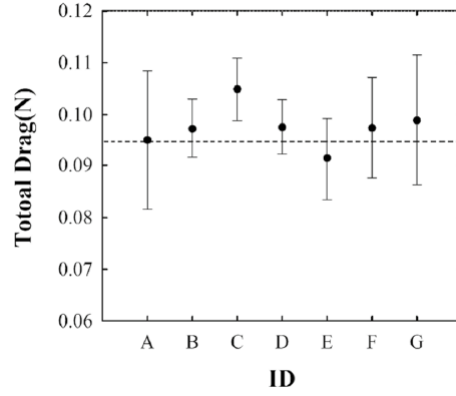
Figure 2.3.3: Total drag measurements for each sample. The error bars are quite large, in particular for the first one (smooth case) and the last three cases. (The figure is taken from Zhou et al. 2021).
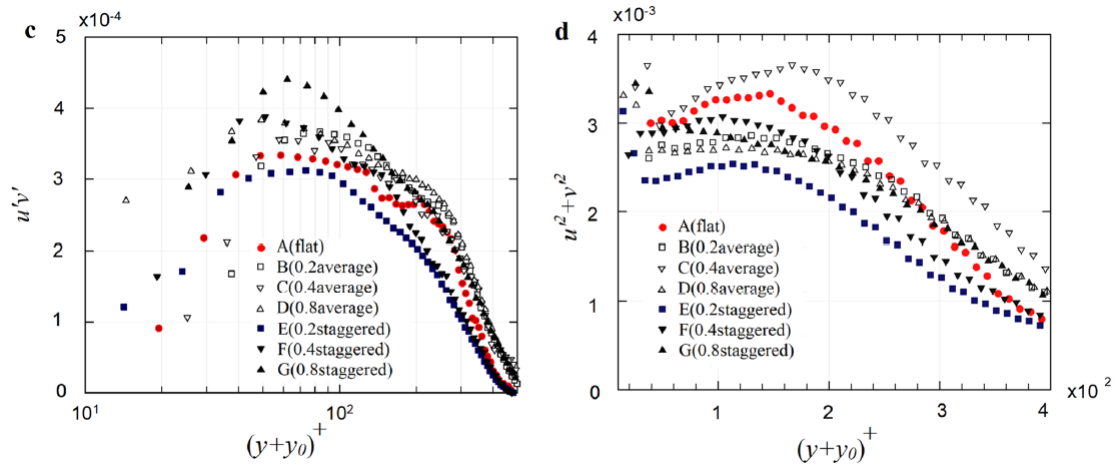
Figure 2.3.4: Time-averaged (sx) Reynolds shear stress (RSS) and (dx) turbulence intensity. (The figure is taken from Zhou et al. 2021).

with respect to the other samples. Indeed, it was found that higher roughness brings undesirable effects to turbulence, resulting in a direct production of larger RSS and TKE. However, the reason why the staggered pattern slows down turbulence within the boundary layer is still unknown.

The authors investigated several prograde (PV) and retrograde (RV) vortices in the instantaneous velocity fields using the ω and the Q-criterion (see fig. 2.3.5). The former had only slight impact while the latter had more negative influences. Sample E was found to create the most PV ($+5\%$) and the least RV ($-(20 \div 30)\%$) with respect to the flat case.

Finally, Sample E showed an extended coherent structure (multiscale hairpin vortex packets) in the streamwise direction, suggesting an orderly turbulence, resulting for benefit to drag reduction compared to the flat case.

50
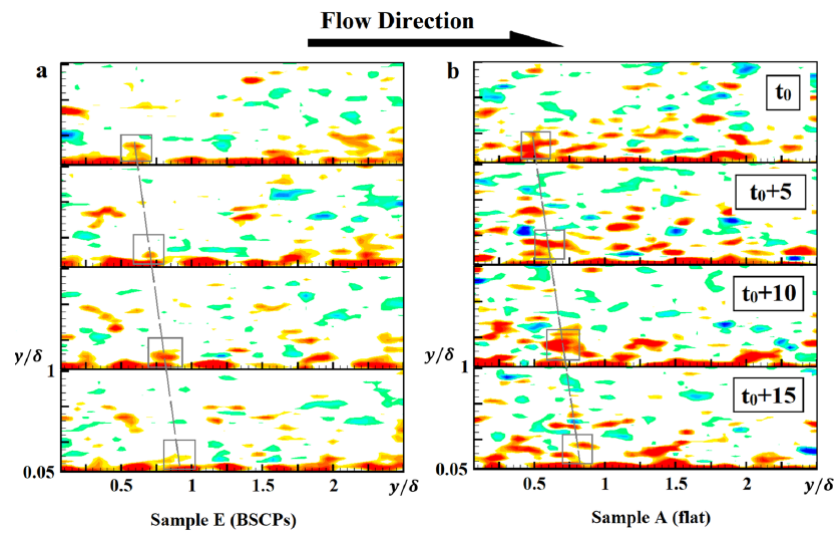
Figure 2.3.5: Temporary evolution of streamwise vorticity within the boundary layer. (a) Sample E. (b) Sample A (flat case). Red/orange=PV (prograde vortices) & Blue/green=RV (retrograde vortices). (The figure is taken from Zhou et al. 2021).

Chapter 3

Interaction of a fluid with a porous medium: microscopic homogenised formulation

This chapter represents the first part of the original project of my thesis, being it an extension of the article by Naqvi and Bottaro 2021 to a three-dimensional and moderately turbulent flow, also with a search for drag-reducing features of the permeable layer.

In this section, we treat the boundary problem for the motion of a 3D fluid near and throughout a porous medium, exploiting the separation of scales: the characteristic microscopic length scale, l, is much smaller than the characteristic macroscopic length scale of the outer flow, L. Thus the problem is amenable to a multiple scale expansion, in terms of a small parameter $\epsilon \equiv l/L \ll 1$. Furthermore, the full domain is split up into three parts (see fig. 3.1.1): a free-fluid region (superscript $^{+}$), a central, thin boundary region (superscript $^{=}$) and a third region governed by Darcy's equation (superscript $^{-}$). $\hat{}$ variables denote dimensional quantities.

We will directly present the 3D theory when inertia is non negligible, performing an Oseen approximation. The coefficients present in the macroscopic interface condition directly arise from the solution of several microscopic problems, which we will numerically solve with inclusions directed both spanwise and streamwise and for several values of both porosity and friction Reynolds number (main useful results are reported in tabular form in 4.2 for any quick consultations). Furthermore, we will also propose a 3D description of the same problem in the limit of small Reynolds number. This time, the coefficients are found by numerically solving Stokes' problems in the microscopic

domain. Then, we will also propose fitting curves in order to find how these coefficients change with porosity, for both inline and staggered configurations (again, main useful results are reported in tabular form in 4.2 for any quick consultations).

Finally, in 4, we will try to test and to use these effective coefficients by simulating macroscopic cases.

3.1 Mathematical Formulation for the Turbulent Case
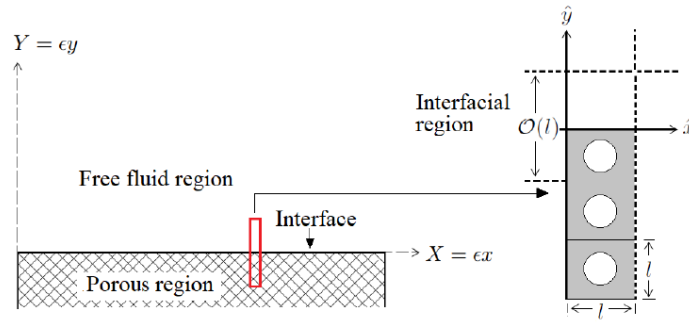
Figure 3.1.1: Schematic of the domain: (sx) macroscopic view highlighting a microscopic cell in red, (dx) microscopic view with dimensional settings. (The figure is taken from Naqvi and Bottaro 2021).

Scaling and equations in the three regions   In the free-fluid region, L, $L/\mathcal{U}$, $\mathcal{U}$ and $\rho\mathcal{U}^2$ (with $\mathcal{U}$ the characteristic free stream velocity and ρ the fluid density) are taken to scale, respectively, length, time, velocity and pressure. The macroscopic Reynolds number is thus $Re = \rho\mathcal{U}L/\mu$. Moreover, we define $X_1 = X = \hat{x}/L$, $X_2 = Y = \hat{y}/L$, $X_3 = Z = \hat{z}/L$, $U_1^+ = U^+ = \hat{u}/\mathcal{U}$, $U_2^+ = V^+ = \hat{v}/\mathcal{U}$ and $U_3^+ = W^+ = \hat{w}/\mathcal{U}$. This leads to the following dimensionless system in the $^+$ region

$$\frac{\partial U_i^+}{\partial X_i} = 0, \quad \frac{\partial U_i^+}{\partial t} + U_j^+ \frac{\partial U_i^+}{\partial X_j} = -\frac{\partial P^+}{\partial X_i} + \frac{1}{Re}\frac{\partial^2 U_i^+}{\partial X_j^2} \tag{3.1.1}$$

Here, the dependent variables are function of only the macroscopic coordinates.

For the intermediate region, we use $l = \epsilon L$, $L/\mathcal{U}$, $\epsilon\mathcal{U}$ and $\mu\mathcal{U}/L$ to scale, respectively, length, time, velocity and pressure. Similarly, we define $x_1 = x = \hat{x}/l$, $x_2 = y = \hat{y}/l$, $x_3 = z = \hat{z}/l$, $U_1 = U = \epsilon^{-1}\hat{u}/\mathcal{U}$, $U_2^= = V^= = \epsilon^{-1}\hat{v}/\mathcal{U}$ and $U_3^= = W^= = \epsilon^{-1}\hat{w}/\mathcal{U}$. The dimensionless equations in the y-elongated microscopic cell are thus

$$\frac{\partial U_i^=}{\partial x_i} = 0, \quad \epsilon^2 \, Re\left(\frac{\partial U_i^=}{\partial t} + U_j^= \frac{\partial U_i^=}{\partial x_j}\right) = -\frac{\partial P^=}{\partial x_i} + \frac{\partial^2 U_i^=}{\partial x_j^2} \tag{3.1.2}$$

Here, the dependent variables are periodic along x and z and they depend on both microscale and macroscale coordinates. This can be seen by matching velocity and traction vectors at the boundary:

$$\lim_{y \to +\infty} \left(U^=, V^=, W^= \right) = \frac{1}{\epsilon} \lim_{Y \to 0^+} \left(U^+, V^+, W^+ \right) \tag{3.1.3}$$

and

$$\lim_{y \to +\infty} \left(\frac{\partial U^=}{\partial y} + \frac{\partial V^=}{\partial x}, -P^= + 2\frac{\partial V^=}{\partial y}, \frac{\partial W^=}{\partial y} + \frac{\partial V^=}{\partial z} \right) =$$
$$= \lim_{Y \to 0^+} \left(\frac{\partial U^+}{\partial Y} + \frac{\partial V^+}{\partial X}, -ReP^+ + 2\frac{\partial V^+}{\partial Y}, \frac{\partial W^+}{\partial Y} + \frac{\partial V^+}{\partial Z} \right) \tag{3.1.4}$$

In the lower region, we use the same scales as in the interface region, except for replacing ϵU by $\epsilon^2 U$ for the velocity and for assuming a steady flow field. This means that viscous dissipation through the pores balances the macroscopic pressure gradient. Thus, in a square unit cell of this region, we have

$$\epsilon \frac{\partial U_i^-}{\partial x_i} = 0, \quad \epsilon^4 Re U_j^- \frac{\partial U_i^-}{\partial x_j} = -\frac{\partial P^-}{\partial x_i} + \epsilon \frac{\partial^2 U_i^-}{\partial x_j^2} \tag{3.1.5}$$

plus periodicity along all spatial directions. The resolution of (3.1.5) yields Darcy's equation.

Instead of doing this, we will try to couple these systems together, as illustrated below.

Asymptotic expansion Here, we try to get a composite system valid in the = and − regions.

From now on, we define $\mathcal{R} = \epsilon^2 Re$ and assume that $\mathcal{R} = \mathcal{O}(1)$. Then, we expand each generic F variable as

$$F\left(x_i, X_i, t \right) = F_0 + \epsilon F_1 + \epsilon^2 F_2 + \ldots \tag{3.1.6}$$

and we use a chain rule,

$$\frac{\partial}{\partial x_j} \to \frac{\partial}{\partial x_j} + \epsilon \frac{\partial}{\partial X_j} \tag{3.1.7}$$

In the end, we get the following results.
= Region:

$$\mathcal{O}\left(\epsilon^0 \right): \quad \frac{\partial U_{0i}^=}{\partial x_i} = 0, \quad \mathcal{R} U_{0j}^= \frac{\partial U_{0i}^=}{\partial x_j} = -\frac{\partial P_0^=}{\partial x_i} + \frac{\partial^2 U_{0i}^=}{\partial x_j^2} \tag{3.1.8}$$

$$\mathcal{O}\left(\epsilon^1\right): \quad \frac{\partial U_{1i}^{=}}{\partial x_i} = -\frac{\partial U_{0i}^{=}}{\partial X_i},$$

$$\mathcal{R}\left(U_{0j}^{=}\frac{\partial U_{1i}^{=}}{\partial x_j} + U_{0j}^{=}\frac{\partial U_{0i}^{=}}{\partial X_j} + U_{1j}^{=}\frac{\partial U_{0i}^{=}}{\partial x_j}\right) = -\frac{\partial P_1^{=}}{\partial x_i} - \frac{\partial P_0^{=}}{\partial X_i} + \frac{\partial^2 U_{1i}^{=}}{\partial x_j^2} + 2\frac{\partial^2 U_{0i}^{=}}{\partial x_j \partial X_j}$$

$$(3.1.9)$$

- Region:

$$\mathcal{O}\left(\epsilon^0\right): \quad \frac{\partial P_0^{-}}{\partial x_i} = 0 \qquad\qquad (3.1.10)$$

$$\mathcal{O}\left(\epsilon^1\right): \quad \frac{\partial U_{0i}^{-}}{\partial x_i} = 0, \quad -\frac{\partial P_1^{-}}{\partial x_i} + \frac{\partial^2 U_{0i}^{-}}{\partial x_j^2} = \frac{\partial P_0^{-}}{\partial X_i} \qquad (3.1.11)$$

$$\mathcal{O}\left(\epsilon^2\right): \quad \frac{\partial U_{1i}^{-}}{\partial x_i} = -\frac{\partial U_{0i}^{-}}{\partial X_i}, \quad \mathcal{R}\,U_{0j}^{-}\frac{\partial U_{0i}^{-}}{\partial x_j} = -\frac{\partial P_2^{-}}{\partial x_i} - \frac{\partial P_1^{-}}{\partial X_i} + \frac{\partial^2 U_{1i}^{-}}{\partial x_j^2} + 2\frac{\partial^2 U_{0i}^{-}}{\partial x_j \partial X_j}$$

$$(3.1.12)$$

The composite description   Now, we decompose the velocity and pressure fields as

$$u_i = u_i^{(0)} + \epsilon u_i^{(1)} + \mathcal{O}\left(\epsilon^2\right) \qquad\qquad (3.1.13)$$

$$p = p^{(0)} + \epsilon p^{(1)} + \mathcal{O}\left(\epsilon^2\right) \qquad\qquad (3.1.14)$$

with

$$u_i^{(0)} = \begin{cases} U_{i0}^{=}, & y > 0 \\ \epsilon U_{i0}^{-}, & y < 0 \end{cases} \qquad\qquad (3.1.15)$$

$$u_i^{(1)} = \begin{cases} U_{i1}^{=}, & y > 0 \\ \epsilon U_{i1}^{-}, & y < 0 \end{cases} \qquad\qquad (3.1.16)$$

$$p^{(0)} = \begin{cases} P_0^{=}, & y > 0 \\ P_0^{-} + \epsilon P_1^{-}, & y < 0 \end{cases} \qquad\qquad (3.1.17)$$

$$p^{(1)} = \begin{cases} P_1^{=}, & y > 0 \\ \epsilon P_2^{-}, & y < 0 \end{cases} \qquad\qquad (3.1.18)$$

Thus, one obtains the following composite system

$$\begin{cases} \partial_i u_i = -\epsilon \partial_i' u_i^{(0)} + \mathcal{O}\left(\epsilon^2\right) \\ -\partial_i p + \partial_j^2 u_i = \mathcal{R}\,u_j \partial_j u_i + \epsilon\left[\partial_i' p^{(0)} - 2\partial_j \partial_j' u_i^{(0)} + \mathcal{R}\,u_j^{(0)} \partial_j' u_i^{(0)}\right] + \mathcal{O}\left(\epsilon^2\right) \end{cases}$$

$$(3.1.19)$$

where we have changed notation by setting

$$\partial_i = \frac{\partial}{\partial x_i}, \quad \partial_i' = \frac{\partial}{\partial X_i} \qquad\qquad (3.1.20)$$
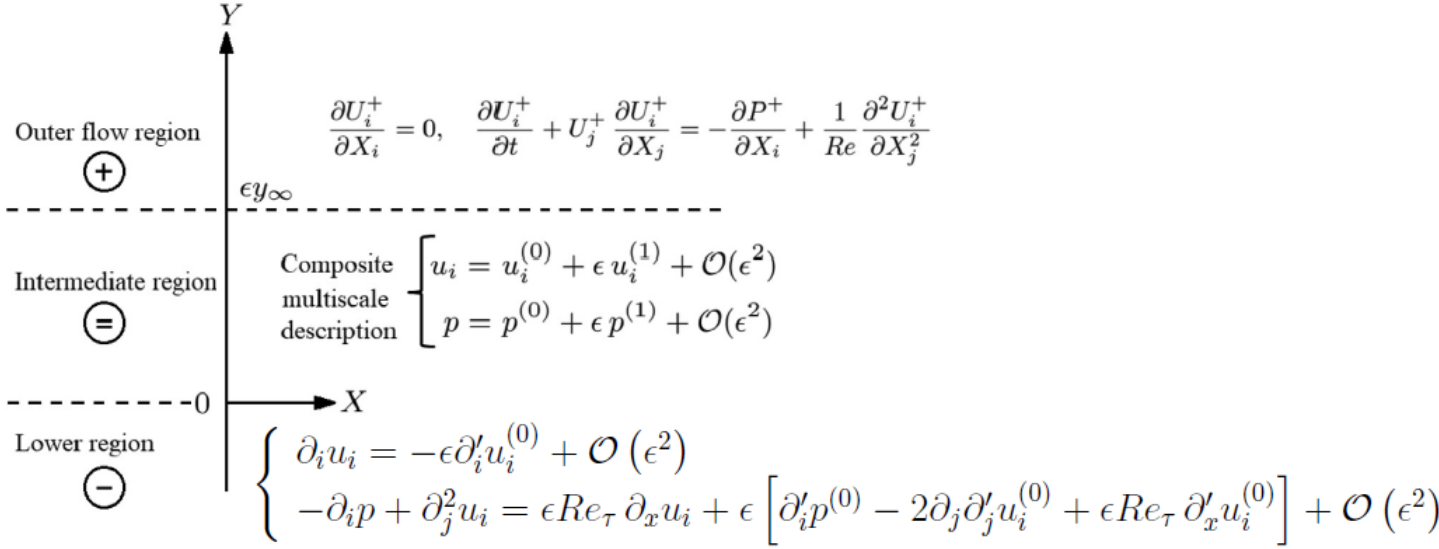
Figure 3.1.2: Graphical representation of the equations in the various regions, after the Oseen linearisation. (The figure has been adapted from Naqvi and Bottaro 2021).

Near-wall turbulence beyond the lower transitionally rough regime: the Oseen approximation In order to treat the problem, we simplify it by linearising the convective terms thanks to an Oseen approximation. In this regime, $\mathcal{R} = \mathcal{O}(1)$, we are authorised to assume that the velocity near the interface is approximately constant, equal to the (dimensionless) friction velocity u^*, and directed along x, i.e. $u_j^{(0)} \simeq (u^*, 0, 0)$, where the dimensional friction velocity $\hat{u}^*$ is normalised as $u^* = \frac{\hat{u}^*}{\epsilon \mathcal{U}}$, with $\mathcal{U}$ the characteristic macroscopic velocity. Now, thanks to this relationships and recalling that $Re = \frac{\mathcal{U}L}{\nu}$, we have

$$-\partial_i p + \partial_j^2 u_i = \epsilon Re_\tau \, \partial_x u_i + \epsilon \left[\partial_i' p^{(0)} - 2\partial_j \partial_j' u_i^{(0)} + \epsilon Re_\tau \, \partial_x' u_i^{(0)} \right] + \mathcal{O}\left(\epsilon^2\right) \quad (3.1.21)$$

where we have defined the friction Reynolds number $Re_\tau = \frac{\hat{u}^* L}{\nu}$. We observe that now we have $\epsilon Re_\tau = \mathcal{O}(1)$.

Thus, the composite description at leading order is given by

$$\mathcal{O}(1): \begin{cases} -\partial_i p^{(0)} + \partial_j^2 u_i^{(0)} = \epsilon Re_\tau \, \partial_x u_i^{(0)} \\ \partial_i u_i^{(0)} = 0 \\ \left(-p^{(0)} \delta_{i_2} + \partial_2 u_i^{(0)} + \partial_i u_2^{(0)} \right)_{y_\infty} = S_{i2} \end{cases} \quad (3.1.22)$$

and at next order we have

$$\mathcal{O}(\epsilon): \begin{cases} -\partial_i p^{(1)} + \partial_j^2 u_i^{(1)} = \epsilon Re_\tau \left(\partial_x u_i^{(1)} + \partial_x' u_i^{(0)} \right) + \partial_i' p^{(0)} - 2\partial_j \partial_j' u_i^{(0)} \\ \partial_i u_i^{(1)} = -\partial_i' u_i^{(0)} \\ \left(-p^{(1)}\delta_{i_2} + \partial_2 u_i^{(1)} + \partial_i u_2^{(1)} \right)_{y_\infty} = -\left(\partial_2' u_i^{(0)} + \partial_i' u_2^{(0)} \right)_{y_\infty} \end{cases}$$

$$(3.1.23)$$

where S_{i2} is the macroscopic traction vector evaluated at $Y = 0^+$, i.e.

$$S_{i2} = \boldsymbol{\sigma}\cdot\boldsymbol{e}_2|_{Y=0^+} = (S^{T_x}, S^N, S^{T_z}) = \lim_{Y \to 0^+} \left(\frac{\partial U}{\partial Y} + \frac{\partial V}{\partial X}, -ReP + 2\frac{\partial V}{\partial Y}, \frac{\partial W}{\partial Y} + \frac{\partial V}{\partial Z} \right)$$

$$(3.1.24)$$

with $\boldsymbol{\sigma}$ the total stress tensor.

Solution of the composite problem Now, thanks to the linearity of the previous systems, we can decompose the velocity and pressure at leading order, $\mathcal{O}(1)$, as

$$\begin{cases} u_i^{(0)} = \tilde{u}_{ij} S_{j2} \\ p^{(0)} = \tilde{p}_j S_{j2} \end{cases}$$

$$(3.1.25)$$

This leads to the following system

$$\begin{cases} -\partial_i \tilde{p}_j + \partial_l^2 \tilde{u}_{ij} = \epsilon Re_\tau \, \partial_x \tilde{u}_{ij} \\ \partial_i \tilde{u}_{ij} = 0 \\ (-\tilde{p}_j \delta_{i2} + \partial_2 \tilde{u}_{ij} + \partial_i \tilde{u}_{2j})_{|y_\infty} = \delta_{ij} \end{cases}$$

$$(3.1.26)$$

which are three microscopic problems for $j = 1, 2, 3$.
At $\mathcal{O}(\epsilon)$, we can decompose velocity and pressure as

$$\begin{cases} u_i^{(1)} = u_{ijk}^{\ddagger} \partial_k' S_{j2} \\ p^{(1)} = p_{jk}^{\ddagger} \partial_k' S_{j2} \end{cases}$$

$$(3.1.27)$$

This leads to

$$\begin{cases} \epsilon Re_\tau \, \partial_x u_{ijk}^{\ddagger} + \tilde{u}_{ij}\delta_{k1} = -\partial_i p_{jk}^{\ddagger} - \tilde{p}_j \delta_{ki} + \partial_l^2 u_{ijk}^{\ddagger} + 2\partial_k \tilde{u}_{ij} \\ \partial_i u_{ijk}^{\ddagger} = -\tilde{u}_{kj} \\ \left(-p_{jk}^{\ddagger}\delta_{i2} + \partial_2 u_{ijk}^{\ddagger} + \partial_i u_{2jk}^{\ddagger} \right)_{|y_\infty} = -\left(\tilde{u}_{ij}\delta_{k2} + \tilde{u}_{2j}\delta_{ik} \right)_{|y_\infty} \end{cases}$$

$$(3.1.28)$$

which are nine problems to be solved in the microscopic cell, for $j, k = 1, 2, 3$.

We have to numerically solve all the previous problems in order to get $\tilde{u}_{ij}|_{y_\infty}$ and $u_{ijk}^{\ddagger}\Big|_{y_\infty}$, which are the numerical coefficients appearing in the macroscopic interface condition.

We now would like to write explicitly every single problem before considering any particular geometry.

At $\mathcal{O}(1)$, one has the following three problems:

$j = 1$:

$$\begin{cases} -\partial_i \tilde{p}_1 + \partial_l^2 \tilde{u}_{i1} = \epsilon Re_\tau \, \partial_1 \tilde{u}_{i1} \\ \partial_i \tilde{u}_{i1} = 0 \\ \boldsymbol{F}^S = (1, 0, 0) \end{cases} \tag{3.1.29}$$

$j = 2$:

$$\begin{cases} -\partial_i \tilde{p}_2 + \partial_l^2 \tilde{u}_{i2} = \epsilon Re_\tau \, \partial_1 \tilde{u}_{i2} \\ \partial_i \tilde{u}_{i2} = 0 \\ \boldsymbol{F}^S = (0, 1, 0) \end{cases} \tag{3.1.30}$$

$j = 3$:

$$\begin{cases} -\partial_i \tilde{p}_3 + \partial_l^2 \tilde{u}_{i3} = \epsilon Re_\tau \, \partial_1 \tilde{u}_{i3} \\ \partial_i \tilde{u}_{i3} = 0 \\ \boldsymbol{F}^S = (0, 0, 1) \end{cases} \tag{3.1.31}$$

where $\boldsymbol{F}^S$ is the (dimensionless) boundary stress imposed at y_∞. For $j = 2$, one finds the simple analytical solution

$$\tilde{u}_{i2} = 0, \quad \tilde{p}_2 = -1. \tag{3.1.32}$$

These results will directly enter the $\mathcal{O}(\epsilon)$ problems.

At $\mathcal{O}(\epsilon)$, one has the following nine problems:

$j = 1, k = 1$:

$$\begin{cases} -\partial_i p_{11}^\ddagger + \partial_l^2 u_{i11}^\ddagger - \epsilon Re_\tau \, \partial_1 u_{i11}^\ddagger - \tilde{u}_{i1} - \tilde{p}_1 \delta_{i1} + 2\partial_1 \tilde{u}_{i1} = 0 \\ \partial_i u_{i11}^\ddagger = -\tilde{u}_{11} \\ \boldsymbol{F}^S = \left(-\tilde{u}_{21}\big|_{y_\infty}, 0, 0 \right) \end{cases} \tag{3.1.33}$$

$j = 1, k = 2$:

$$\begin{cases} -\partial_i p_{12}^\ddagger + \partial_l^2 u_{i12}^\ddagger - \epsilon Re_\tau \, \partial_1 u_{i12}^\ddagger - \tilde{p}_1 \delta_{i2} + 2\partial_2 \tilde{u}_{i1} = 0 \\ \partial_i u_{i12}^\ddagger = -\tilde{u}_{21} \\ \boldsymbol{F}^S = \left(-\tilde{u}_{11}\big|_{y_\infty}, -2\,\tilde{u}_{21}\big|_{y_\infty}, -\tilde{u}_{31}\big|_{y_\infty} \right) \end{cases} \tag{3.1.34}$$

$j = 1, k = 3$:

$$\begin{cases} -\partial_i p_{13}^\ddagger + \partial_l^2 u_{i13}^\ddagger - \epsilon Re_\tau \, \partial_1 u_{i13}^\ddagger - \tilde{p}_1 \delta_{i3} + 2\partial_3 \tilde{u}_{i1} = 0 \\ \partial_i u_{i13}^\ddagger = -\tilde{u}_{31} \\ \boldsymbol{F}^S = \left(0, 0, -\tilde{u}_{21}\big|_{y_\infty} \right) \end{cases} \tag{3.1.35}$$

$j = 2, k = 1$:

$$\begin{cases} -\partial_i p^\ddagger_{21} + \partial_l^2 u^\ddagger_{i21} - \epsilon Re_\tau\, \partial_1 u^\ddagger_{i21} + \delta_{i1} = 0 \\ \partial_i u^\ddagger_{i21} = 0 \\ \boldsymbol{F}^S = (0,0,0) \end{cases} \tag{3.1.36}$$

$j = 2, k = 2$:

$$\begin{cases} -\partial_i p^\ddagger_{22} + \partial_l^2 u^\ddagger_{i22} - \epsilon Re_\tau\, \partial_1 u^\ddagger_{i22} + \delta_{i2} = 0 \\ \partial_i u^\ddagger_{i22} = 0 \\ \boldsymbol{F}^S = (0,0,0) \end{cases} \tag{3.1.37}$$

$j = 2, k = 3$:

$$\begin{cases} -\partial_i p^\ddagger_{23} + \partial_l^2 u^\ddagger_{i23} - \epsilon Re_\tau\, \partial_1 u^\ddagger_{i23} + \delta_{i3} = 0 \\ \partial_i u^\ddagger_{i23} = 0 \\ \boldsymbol{F}^S = (0,0,0) \end{cases} \tag{3.1.38}$$

$j = 3, k = 1$:

$$\begin{cases} -\partial_i p^\ddagger_{31} + \partial_l^2 u^\ddagger_{i31} - \epsilon Re_\tau\, \partial_1 u^\ddagger_{i31} - \tilde{u}_{i3} - \tilde{p}_3 \delta_{i1} + 2\partial_1 \tilde{u}_{i3} = 0 \\ \partial_i u^\ddagger_{i31} = -\tilde{u}_{13} \\ \boldsymbol{F}^S = \left(-\left.\tilde{u}_{23}\right|_{y_\infty}, 0, 0 \right) \end{cases} \tag{3.1.39}$$

$j = 3, k = 2$:

$$\begin{cases} -\partial_i p^\ddagger_{32} + \partial_l^2 u^\ddagger_{i32} - \epsilon Re_\tau\, \partial_1 u^\ddagger_{i32} - \tilde{p}_3 \delta_{i2} + 2\partial_2 \tilde{u}_{i3} = 0 \\ \partial_i u^\ddagger_{i32} = -\tilde{u}_{23} \\ \boldsymbol{F}^S = \left(-\left.\tilde{u}_{13}\right|_{y_\infty}, -2\left.\tilde{u}_{23}\right|_{y_\infty}, -\left.\tilde{u}_{33}\right|_{y_\infty} \right) \end{cases} \tag{3.1.40}$$

$j = 3, k = 3$:

$$\begin{cases} -\partial_i p^\ddagger_{33} + \partial_l^2 u^\ddagger_{i33} - \epsilon Re_\tau\, \partial_1 u^\ddagger_{i33} - \tilde{p}_3 \delta_{i3} + 2\partial_3 \tilde{u}_{i3} = 0 \\ \partial_i u^\ddagger_{i33} = -\tilde{u}_{33} \\ \boldsymbol{F}^S = \left(0,0, -\left.\tilde{u}_{23}\right|_{y_\infty} \right) \end{cases} \tag{3.1.41}$$

This problems will simplify once the $\mathcal{O}(1)$ solutions are available.

All these problems are subject to periodicity along x and z and to the no-slip condition on the solid grains of the porous medium.

The boundary condition   The boundary condition arises from matching the velocity at the two scales, i.e.

$$\left. U_i \right|_{Y=\epsilon y_\infty} = \epsilon \left(\left. u_i^{(0)} \right|_{y_\infty} + \epsilon \left. u_i^{(1)} \right|_{y_\infty} \right) + \mathcal{O}(\epsilon^3) = \epsilon \left. \tilde{u}_{ij} \right|_{y_\infty} S_{j2} + \epsilon^2 \left. u^\ddagger_{ijk} \right|_{y_\infty} \frac{\partial S_{j2}}{\partial X_k} + \mathcal{O}(\epsilon^3) \tag{3.1.42}$$

We will implement later this condition, after solving the microscopic problems.

3.2 Numerical solution of the microscopic problems in the Oseen Approximation

3.2.1 Spanwise Cylinders
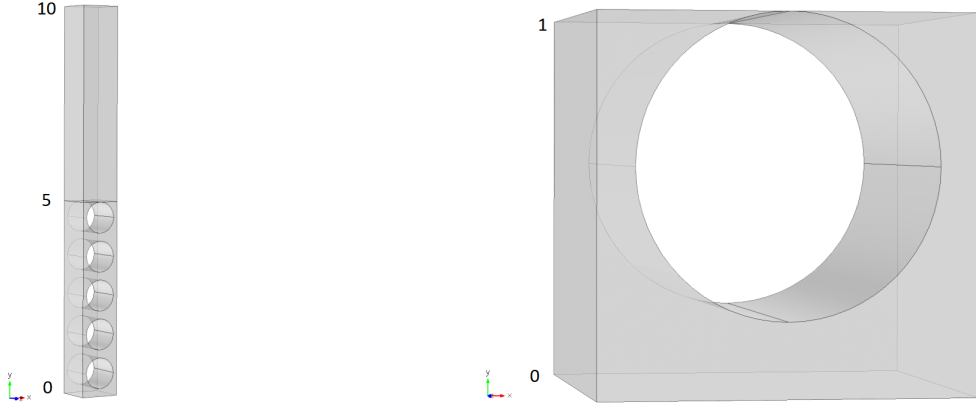
Figure 3.2.1: System geometry for spanwise-aligned cylinders: (sx) elongated domain (dx) fully periodic unit cell. Drawing not to scale.

With the aid of the software Comsol Multiphysics, we will now numerically solve the microscopic problem in the microscopic elongated domain, considering cylindrical solid inclusions, with axes directed spanwise, i.e. along z direction (see fig. 3.2.1). More specifically, our domain will consist of a xyz box of sides $[1, 2y_\infty, 1]$. We have to choose the value of y_∞ so that the fields will be homogeneous in x and z near $y = y_\infty$. Usually, we will take $y_\infty = 5$. The dividing surface is set at $y = y_\infty$, so that half of the domain ($y_\infty < y < 2y_\infty$) is over it and the other half ($0 < y < y_\infty$) below it. For $0 < y < y_\infty$, the above mentioned identical cylindrical solid grains are present, spaced of 1 unit in y and with an extension of 1 unit in z. The radius of the cylinders will be set according to the specific chosen value of porosity, using the formula

$$r = \sqrt{\frac{1 - \theta}{\pi}} \tag{3.2.1}$$

which comes directly from the definitions of porosity: $\theta = \frac{V_f}{V} = \frac{V - V_p}{V} = 1 - \pi r^2$. We will set the center of the cylinders so that the first cylinder is tangent to the dividing surface: $y_{cyl} = 1 - r$, with respect to $y = 0$.

We will at first fix both porosity to $\theta = 0.5$ and $Re_\tau = 180$ and compute the coefficients for varying y_∞, in order to find a trend the allows us to evaluate the parameters at $y_\infty \to 0$.

Then, we will fix only the value of the porosity at $\theta = 0.5$ and compute the coefficients for different values of Re_τ in the interval $[0, 390]$.

Finally, we will vary also the porosity in the interval $[0.215, 0.99]$ for several fixed values of $Re_\tau = 0, 193, 390$. Meanwhile, we will also plot these same

values by "transposing" them, i.e. we will vary Re_τ in the interval $[0, 390]$ for each fixed value of θ in the interval $[0.215, 0.99]$, just for having a complementary view of the same set of data.

Throughout the discussion, we will always take $\epsilon = 0.2$.

Before showing the first results, we would like to emphasise that, with the current values of ϵ and Re_τ, the assumption $\epsilon Re_\tau = \mathcal{O}(1)$ is not strictly valid anymore, in particular, we have $\epsilon Re_\tau = \mathcal{O}(10)$. This is not a real problem, since, in perturbation theory, one usually does asymptotic expansions in terms of a "small" parameter ε (formally $\varepsilon \ll 1$) that in reality can be set equal to 1. This is to say that we can go beyond the formal limit imposed by the theory and the results will still be correct. In our case, $\epsilon = 0.2$ is not so small because we are dealing with a very particular porous medium. On the other hand, if we took a common porous medium, like a soil or a fabric, we would obtain a really small ϵ, so that we could easily be within the limits of the theory.

Trend at the leading order problems In this case, we find that only $\tilde{u}_{11}\big|_{y_\infty}$ and $\tilde{u}_{33}\big|_{y_\infty}$ are non zero (see table 3.1). In particular, varying y_∞, one finds that (see fig. 3.2.2)

$$\tilde{u}_{11}\big|_{y_\infty} = y_\infty + \lambda_x, \quad \tilde{u}_{33}\big|_{y_\infty} = y_\infty + \lambda_z \tag{3.2.2}$$

with λ_x and λ_z slip lengths.

The same results are recovered also by

$$\lambda_i = \frac{1}{A} \int_S \tilde{u}_{ii}\big|_{y_\infty} \, \mathrm{d}S - y_\infty \tag{3.2.3}$$

for $i = 1, 3 = x, z$ (without summing), where the mean surface integral is evaluated at the top surface and A is the area of the integral surface ($A = 1$ in this case). This is true since the following equality holds:

$$\frac{1}{A} \int_S \tilde{u}_{ij}\big|_{y_\infty} \, \mathrm{d}S = \tilde{u}_{ij}\big|_{y_\infty} \tag{3.2.4}$$

because the fields are homogeneous in x and z at y_∞ (top surface).

y_∞	$\tilde{u}_{11}\vert_{y_\infty}$	$\tilde{u}_{33}\vert_{y_\infty}$
3	3.03560E + 00	3.04858E + 00
4	4.03564E + 00	4.04861E + 00
5	5.03562E + 00	5.04859E + 00
6	6.03563E + 00	6.04860E + 00
7	7.03567E + 00	7.04863E + 00

$$(3.2.5)$$

Table 3.1: This table shows the trend of $\tilde{u}_{11}$ and $\tilde{u}_{33}$ against y_∞, in order to compute λ_x and λ_z coefficients. The computation has been carried out for $\theta = 0.5$ and $Re_\tau = 180$.
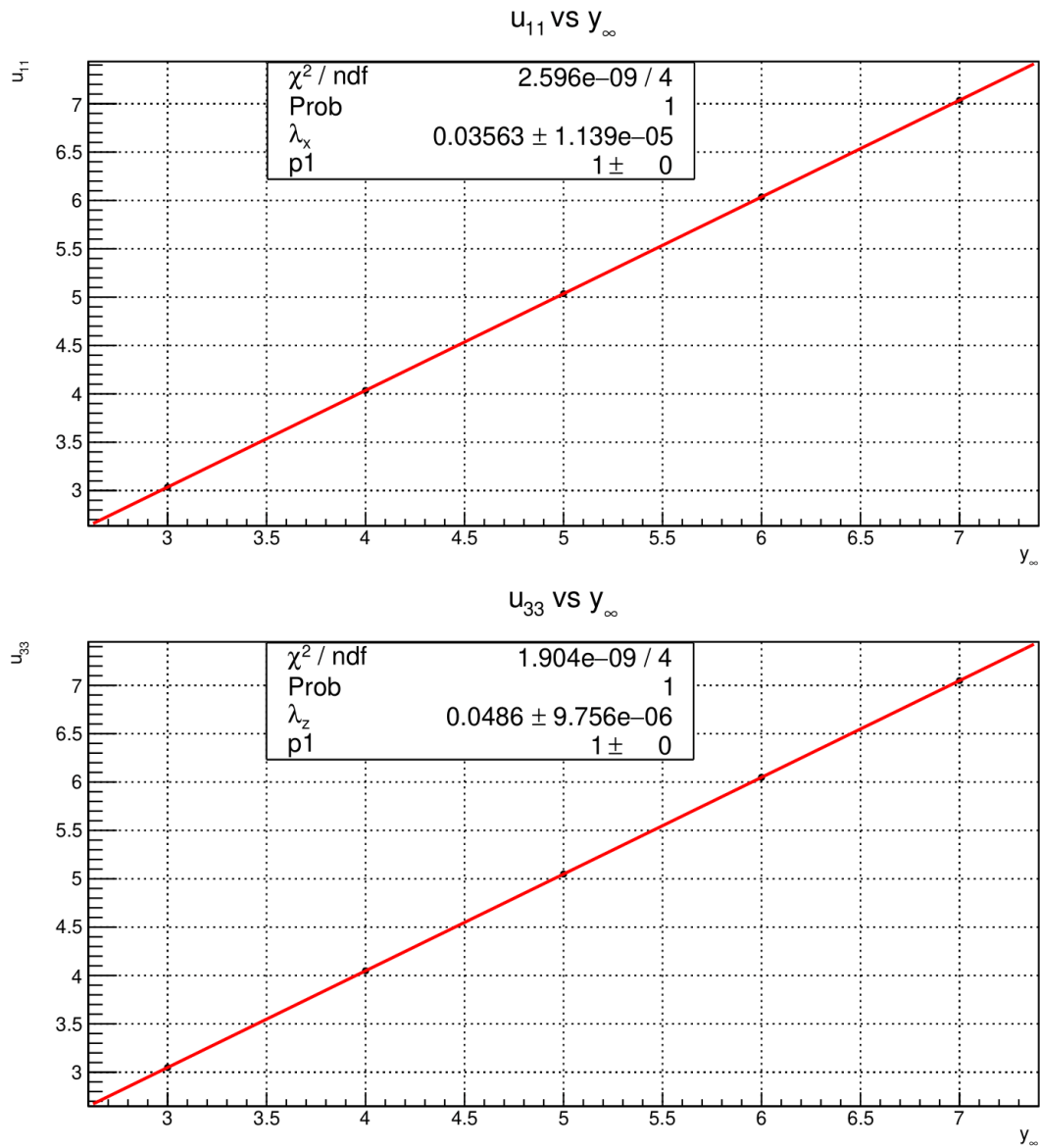
Figure 3.2.2: Fit to the trend of the λ_x and λ_z coefficients with a linear function.

Trend at the higher order problems Having solved the $\mathcal{O}(1)$ problems, little simplifications in the $\mathcal{O}(\epsilon)$ problems, in particular in the boundary stress conditions, can be made. One finds

$j = 1, k = 1$:

$$
\begin{cases}
-\partial_i p_{11}^{\ddagger} + \partial_l^2 u_{i11}^{\ddagger} - \epsilon Re_\tau \, \partial_1 u_{i11}^{\ddagger} - \tilde{u}_{i1} - \tilde{p}_1 \delta_{i1} + 2\partial_1 \tilde{u}_{i1} = 0 \\
\partial_i u_{i11}^{\ddagger} = -\tilde{u}_{11} \\
\boldsymbol{F}^S = (0, 0, 0)
\end{cases}
\tag{3.2.6}
$$

$j = 1, k = 2$:

$$
\begin{cases}
-\partial_i p_{12}^{\ddagger} + \partial_l^2 u_{i12}^{\ddagger} - \epsilon Re_\tau \, \partial_1 u_{i12}^{\ddagger} - \tilde{p}_1 \delta_{i2} + 2\partial_2 \tilde{u}_{i1} = 0 \\
\partial_i u_{i12}^{\ddagger} = -\tilde{u}_{21} \\
\boldsymbol{F}^S = \left(-\tilde{u}_{11}\big|_{y_\infty}, 0, 0 \right)
\end{cases}
\tag{3.2.7}
$$

$j = 1, k = 3$:

$$
\begin{cases}
-\partial_i p_{13}^{\ddagger} + \partial_l^2 u_{i13}^{\ddagger} - \epsilon Re_\tau \, \partial_1 u_{i13}^{\ddagger} - \tilde{p}_1 \delta_{i3} + 2\partial_3 \tilde{u}_{i1} = 0 \\
\partial_i u_{i13}^{\ddagger} = -\tilde{u}_{31} \\
\boldsymbol{F}^S = (0, 0, 0)
\end{cases}
\tag{3.2.8}
$$

$j = 2, k = 1$:

$$
\begin{cases}
-\partial_i p_{21}^{\ddagger} + \partial_l^2 u_{i21}^{\ddagger} - \epsilon Re_\tau \, \partial_1 u_{i21}^{\ddagger} + \delta_{i1} = 0 \\
\partial_i u_{i21}^{\ddagger} = 0 \\
\boldsymbol{F}^S = (0, 0, 0)
\end{cases}
\tag{3.2.9}
$$

$j = 2, k = 2$:

$$
\begin{cases}
-\partial_i p_{22}^{\ddagger} + \partial_l^2 u_{i22}^{\ddagger} - \epsilon Re_\tau \, \partial_1 u_{i22}^{\ddagger} + \delta_{i2} = 0 \\
\partial_i u_{i22}^{\ddagger} = 0 \\
\boldsymbol{F}^S = (0, 0, 0)
\end{cases}
\tag{3.2.10}
$$

$j = 2, k = 3$:

$$
\begin{cases}
-\partial_i p_{23}^{\ddagger} + \partial_l^2 u_{i23}^{\ddagger} - \epsilon Re_\tau \, \partial_1 u_{i23}^{\ddagger} + \delta_{i3} = 0 \\
\partial_i u_{i23}^{\ddagger} = 0 \\
\boldsymbol{F}^S = (0, 0, 0)
\end{cases}
\tag{3.2.11}
$$

$j = 3, k = 1$:

$$
\begin{cases}
-\partial_i p_{31}^{\ddagger} + \partial_l^2 u_{i31}^{\ddagger} - \epsilon Re_\tau \, \partial_1 u_{i31}^{\ddagger} - \tilde{u}_{i3} - \tilde{p}_3 \delta_{i1} + 2\partial_1 \tilde{u}_{i3} = 0 \\
\partial_i u_{i31}^{\ddagger} = -\tilde{u}_{13} \\
\boldsymbol{F}^S = (0, 0, 0)
\end{cases}
\tag{3.2.12}
$$

$j = 3, k = 2$:

$$
\begin{cases}
-\partial_i p_{32}^{\ddagger} + \partial_l^2 u_{i32}^{\ddagger} - \epsilon Re_\tau \, \partial_1 u_{i32}^{\ddagger} - \tilde{p}_3 \delta_{i2} + 2\partial_2 \tilde{u}_{i3} = 0 \\
\partial_i u_{i32}^{\ddagger} = -\tilde{u}_{23} \\
\boldsymbol{F}^S = \left(0, 0, -\tilde{u}_{33}\big|_{y_\infty} \right)
\end{cases}
\tag{3.2.13}
$$

$j = 3, k = 3$:

$$\begin{cases} -\partial_i p_{33}^{\ddagger} + \partial_l^2 u_{i33}^{\ddagger} - \epsilon Re_\tau \, \partial_1 u_{i33}^{\ddagger} - \tilde{p}_3 \delta_{i3} + 2\partial_3 \tilde{u}_{i3} = 0 \\ \partial_i u_{i33}^{\ddagger} = -\tilde{u}_{33} \\ \boldsymbol{F}^S = (0,0,0) \end{cases} \quad (3.2.14)$$

In this case, the only non zero coefficients are given by

$$\begin{aligned} -\left. u_{211}^{\ddagger} \right|_{y_\infty} &= \left. u_{121}^{\ddagger} \right|_{y_\infty} = 0.5 \, y_\infty^2 + \lambda_x \, y_\infty + \mathcal{K}_{xy}^{itf} \\ -\left. u_{233}^{\ddagger} \right|_{y_\infty} &= \left. u_{323}^{\ddagger} \right|_{y_\infty} = 0.5 \, y_\infty^2 + \lambda_z \, y_\infty + \mathcal{K}_{zy}^{itf} \\ \left. u_{222}^{\ddagger} \right|_{y_\infty} &= \mathcal{K}_{yy} \end{aligned} \quad (3.2.15)$$

where $\mathcal{K}_{yy}$ is the *apparent* permeability (*apparent* because of inertia; it will become the *medium* permeability in the small Re_τ limit) and $\mathcal{K}_{xy}^{itf}$ and $\mathcal{K}_{zy}^{itf}$ are the interface permeabilities (see table 3.2 for data and fig. 3.2.3 for fit). In particular, for the medium permeability we found that also a linear or quadratic trend can be proposed (see fig. 3.2.4). However, the absolute variation is so small that it can be imputed to numerical errors in the software computation. Then, we decided to quote a constant trend, that is the same trend found in the Stokes' limit.

These are the only parameters that enter the interface condition, since we decided to evaluate the fields in the limit $y_\infty \to 0$. In particular, we found that some fields sensibly differ from 0 at $y_\infty = 5$ (or any other sufficiently large finite value) but are compatible with a zero value at $y_\infty = 0$. These fields are $\left. u_{111}^{\ddagger} \right|_{y_\infty}$ and $\left. u_{331}^{\ddagger} \right|_{y_\infty}$ (see fig. 3.2.5). This phenomenon happens also in the Stokes' limit.

Also this time, the numerical value of the fields at the top surface corresponds to the one obtained performing the top surface average of the same fields:

$$\frac{1}{A} \int_S \left. u_{ijk}^{\ddagger} \right|_{y_\infty} \mathrm{d}S = \left. u_{ijk}^{\ddagger} \right|_{y_\infty} \quad (3.2.16)$$

where, as before, $A = 1$.

Moreover, as, once again, found in the Stokes limit, the numerical values of the above mentioned parameters are recovered also by taking the following volume integrals already in the $\mathcal{O}(1)$ simulations:

$$\begin{aligned} \mathcal{K}_{xy}^{itf} &= \int_{\mathcal{V}_{f_{Por}}} \tilde{u}_{11} \, \mathrm{d}V \\ \mathcal{K}_{zy}^{itf} &= \int_{\mathcal{V}_{f_{Por}}} \tilde{u}_{33} \, \mathrm{d}V \end{aligned} \quad (3.2.17)$$

where $\mathcal{V}_{f_{Por}}$ denotes the fluid volume below the interface. This results is particularly convenient since it means that interface permeabilities are already

y_∞	$u^{\ddagger}_{121}\big|_{y_\infty}$	$u^{\ddagger}_{211}\big|_{y_\infty}$	$u^{\ddagger}_{323}\big|_{y_\infty}$	$u^{\ddagger}_{233}\big|_{y_\infty}$	$u^{\ddagger}_{222}\big|_{y_\infty}$	$u^{\ddagger}_{111}\big|_{y_\infty}$	$u^{\ddagger}_{331}\big|_{y_\infty}$
3		$-4.6079\text{E}+00$				$-9.3238\text{E}+00$	$-9.4436\text{E}+00$
4	$8.1439\text{E}+00$	$-8.1436\text{E}+00$	$8.1973\text{E}+00$	$-8.1972\text{E}+00$	$9.849\text{E}-04$	$-2.1908\text{E}+01$	$-2.2120\text{E}+01$
5	$1.2679\text{E}+01$	$-1.2679\text{E}+01$	$1.2746\text{E}+01$	$-1.2746\text{E}+01$	$9.859\text{E}-04$	$-4.2563\text{E}+01$	$-4.2892\text{E}+01$
6	$1.8215\text{E}+01$	$-1.8216\text{E}+01$	$1.8294\text{E}+01$	$-1.8295\text{E}+01$	$9.866\text{E}-04$	$-7.3290\text{E}+01$	$-7.3763\text{E}+01$
7		$-2.4752\text{E}+01$			$9.871\text{E}-04$	$-1.1609\text{E}+02$	$-1.1673\text{E}+02$

$$(3.2.20)$$

Table 3.2: This table shows the trend of $\mathcal{O}(\epsilon)$ fields at y_∞ against y_∞, in order to compute $\mathcal{K}^{itf}_{xy}$, $\mathcal{K}^{itf}_{zy}$ and $\mathcal{K}_{yy}$ and λ_z coefficients. The computation has been carried out for $\theta = 0.5$ and $Re_\tau = 180$.

available from the $\mathcal{O}(1)$ problems, and so one does not need to solve the $\mathcal{O}(\epsilon)$ ones to compute them.

Finally, as far as the medium permeability is concerned, one can compute it also simulating the same $\mathcal{O}(\epsilon)$ problem in the fully periodic unit cell, which is computationally less expensive than using the elongated domain, and performing the following operation:

$$\mathcal{K}_{yy} = \int_{\mathcal{V}_f} u^{\ddagger}_{222}\,\mathrm{d}V \qquad (3.2.18)$$

where $\mathcal{V}_f$ is the fluid's volume. This is true only for the $u^{\ddagger}_{222}\big|_{y_\infty=0} = \mathcal{K}_{yy}$ parameter. Indeed, other diagonal components of the medium permeability tensor can be computed in the following way:

$$\begin{aligned} \mathcal{K}_{xx} &= \int_{\mathcal{V}_f} u^{\ddagger}_{121}\,\mathrm{d}V \\ \mathcal{K}_{zz} &= \int_{\mathcal{V}_f} u^{\ddagger}_{323}\,\mathrm{d}V \end{aligned} \qquad (3.2.19)$$

where the integral must be performed in the fully-periodic unit cell. We remark that, in this case, $\mathcal{K}_{xx}$ and $\mathcal{K}_{zz}$ do not correspond to any value of $u^{\ddagger}_{ijk}\big|_{y_\infty=0}$. Hence, they do not enter the interface condition. We should also mention that, in this case, differently from the Stokes' regime, where the relationship $\mathcal{K}_{xx} \approx \mathcal{K}_{yy}$ must be recovered, we have $\mathcal{K}_{xx} \neq \mathcal{K}_{yy}$, since we assumed convection along the x-direction.
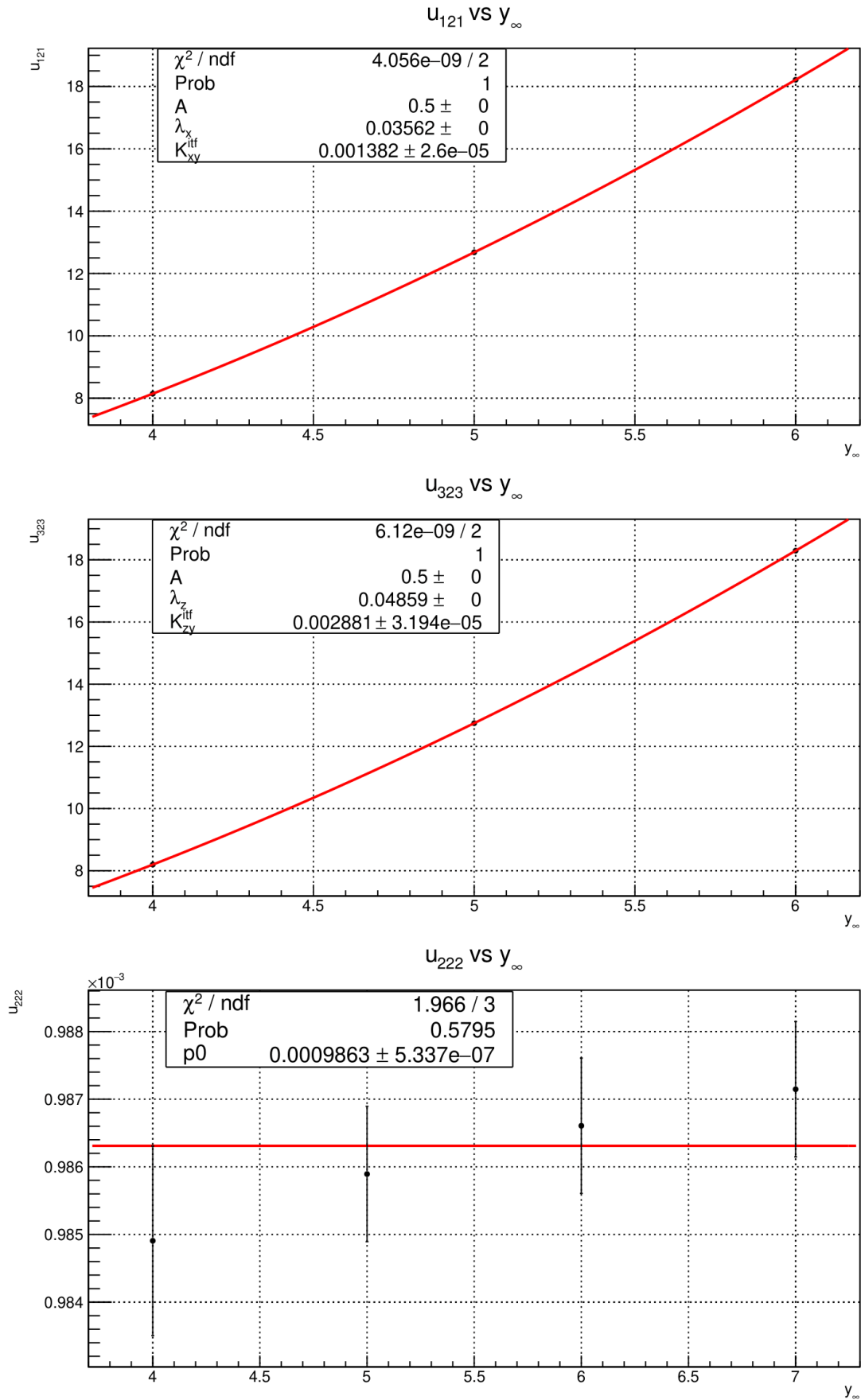
Figure 3.2.3: Fit to the trend of the $\mathcal{O}(\epsilon)$ coefficients: $\mathcal{K}_{xy}^{itf}$, $\mathcal{K}_{zy}^{itf}$ and $\mathcal{K}_{yy}$. In the last figure from top, the p_0 fitting parameter is $\mathcal{K}_{yy}$ and the vertical error bars, $\pm 10^{-6}$, are present only to make the fit converge.
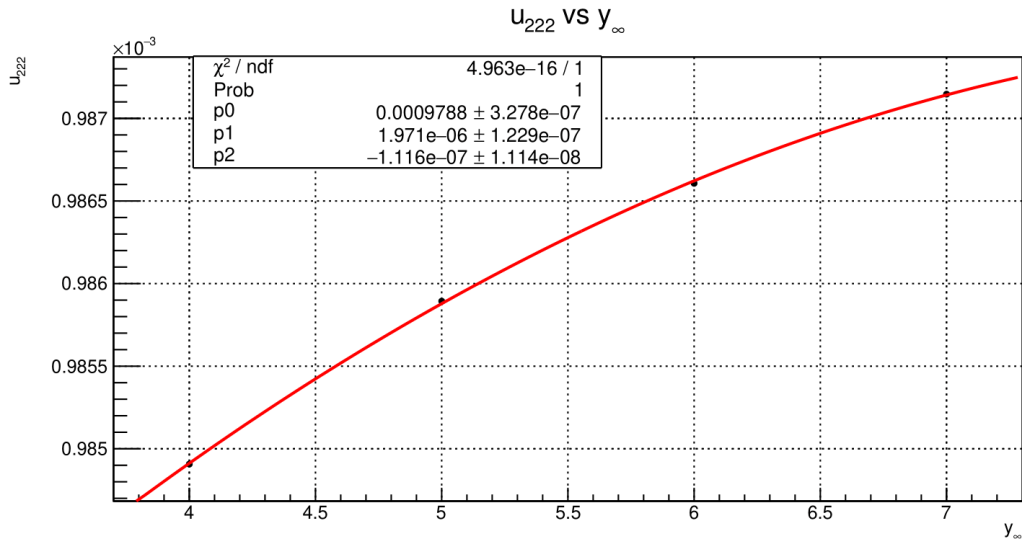
Figure 3.2.4: Fit to the trend of $\mathcal{K}_{yy}$ coefficient with a quadratic function. The p_0 fitting parameter is $\mathcal{K}_{yy}$.
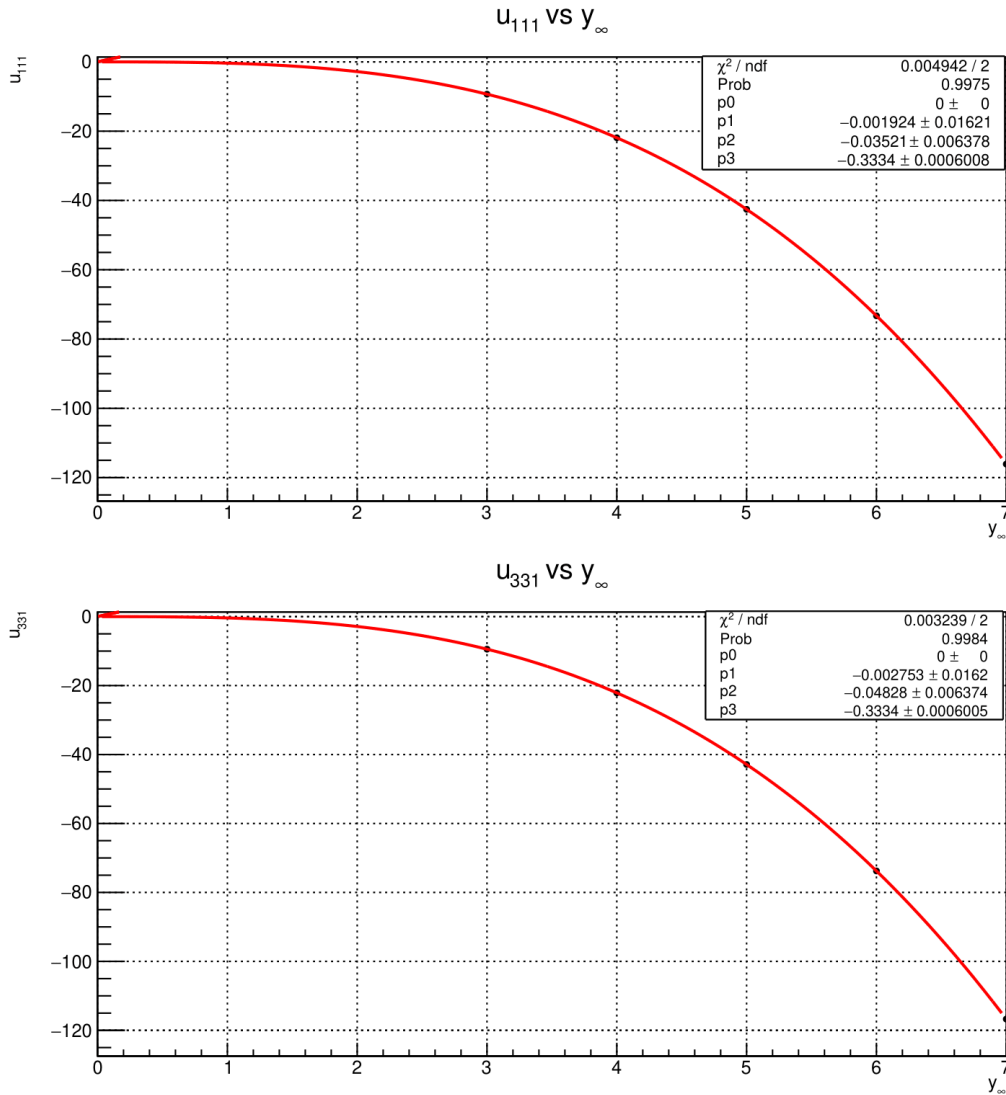
Figure 3.2.5: Fit to the trend of $u^{\ddagger}_{111}\big|_{y_\infty}$ and $u^{\ddagger}_{331}\big|_{y_\infty}$ coefficients showing they are zero at the origin.

Results for $\theta = 0.5$ and several Re_τ   We now fix $\theta = 0.5$ (and $\epsilon = 0.2$) and compute the coefficients for several values of Re_τ in the interval $[0, 390]$. When possible, also $\mathcal{K}_{xy}^{itf}$ and $\mathcal{K}_{zy}^{itf}$ have been calculated directly from the $\mathcal{O}(1)$ simulations. Moreover, $\mathcal{K}_{yy}$ has been calculated indifferently in the elongated domain or in the fully periodic unit cell. Results are reported in table 4.7

A decreasing trend with Re_τ has been found for all parameters (see fig. 3.2.6).

Coefficients variation with θ for several fixed Re_τ   We now fix $Re_\tau = 0, 193, 390$ (and $\epsilon = 0.2$) and compute, for each Re_τ, the parameters for varying θ in the interval $[0.215, 0.99]$. $\theta = 0.215$ is the minimum value of porosity for our geometry ($r = 0.5$): it is as if the medium is not permeable anymore ($\mathcal{K}_{yy} = 0$), like a rough wall. For the case $Re_\tau = 0$, more values of θ are reported, since we wanted to better characterise the laminar case. Results are reported in tables 4.5, 4.8 and 4.9.

This time, we find an increasing trend in θ, while the different curves corresponding to a particular value of Re_τ show the same previous decreasing trend in this parameter (see fig. 3.2.7).

Moreover, in figures 3.2.8, 3.2.9, velocity and pressure fields are shown in the xy plane for the shear-along-x problem (i.e. $\tilde{u}_{i1}$). One can see the effect of changing θ (first picture) and Re_τ (second picture).

Furthermore, figure 3.2.10 shows $\mathcal{K}_{yy}$ in the fully periodic unit cell. Again, one can see separately the effect of changing θ and Re_τ. In particular, we see that changing only θ one keeps the same trend, while changing Re_τ from 0 to 193, leads to a different profile, in account that we assumed convection along x-direction.

Coefficients variation with Re_τ for several fixed θ   We now consider the "transpose" values of the previous case, i.e. we keep porosity fixed to $\theta = 0.215, 0.5, 0.8, 0.9, 0.99$ and, for each of these values, we compute the coefficients letting Re_τ varying in $[0, 390]$ (always with $\epsilon = 0.2$). Numerical values are reported in tables 4.10, 4.11, 4.12 and 4.13. This analysis does not add anything else from physical point of view to the previous one, but it is another option to show the data concentrating on the variation on Re_τ instead on θ.

Indeed the same decreasing trend with Re_τ for all parameters is confirmed for each value of θ (see fig. 3.2.11).

68
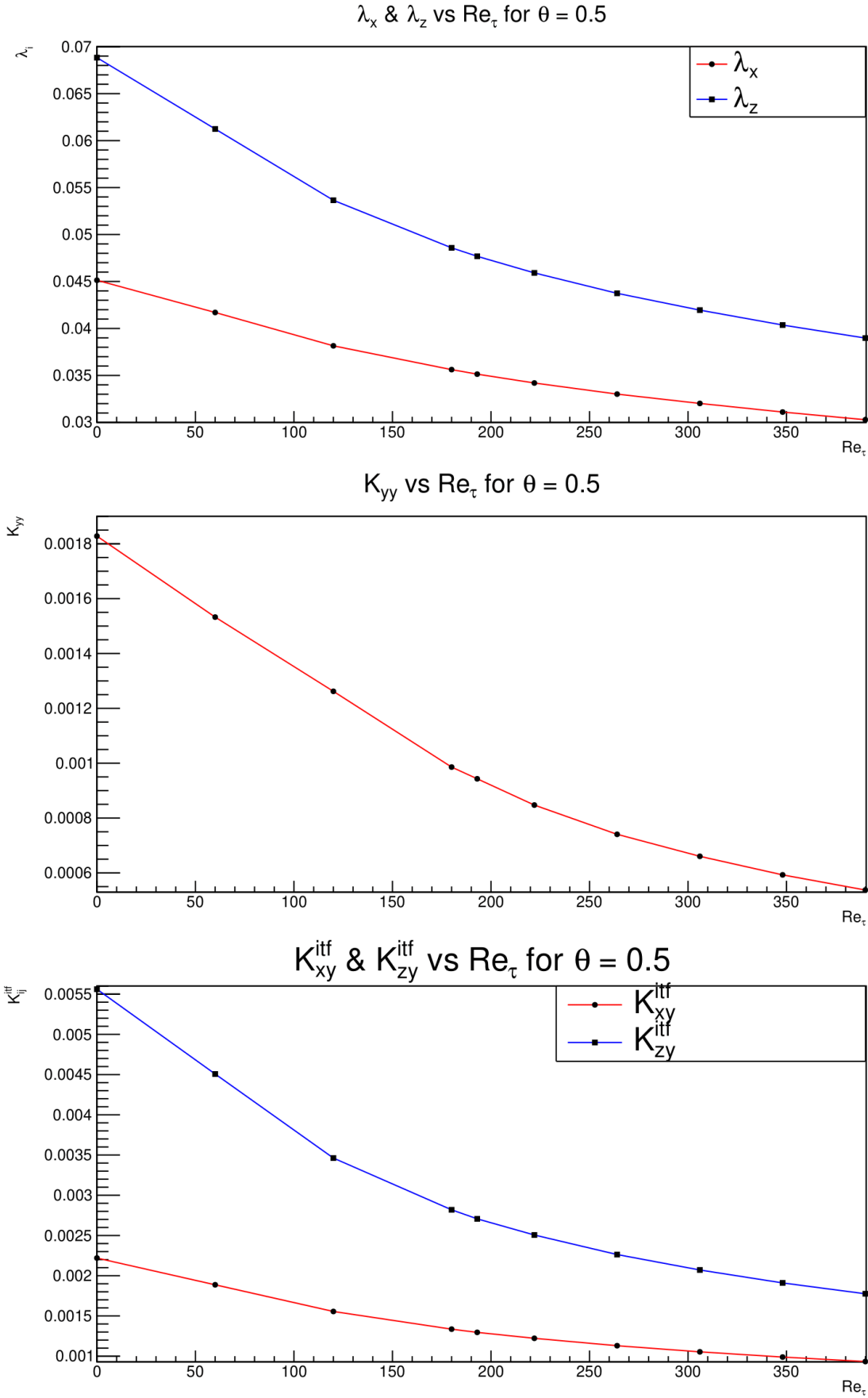
Figure 3.2.6: Graphs of Table 4.7, i.e. of the parameters against Re_τ having fixed $\theta = 0.5$ and $\epsilon = 0.2$, for *inline* pattern and *spanwise* inclusions.
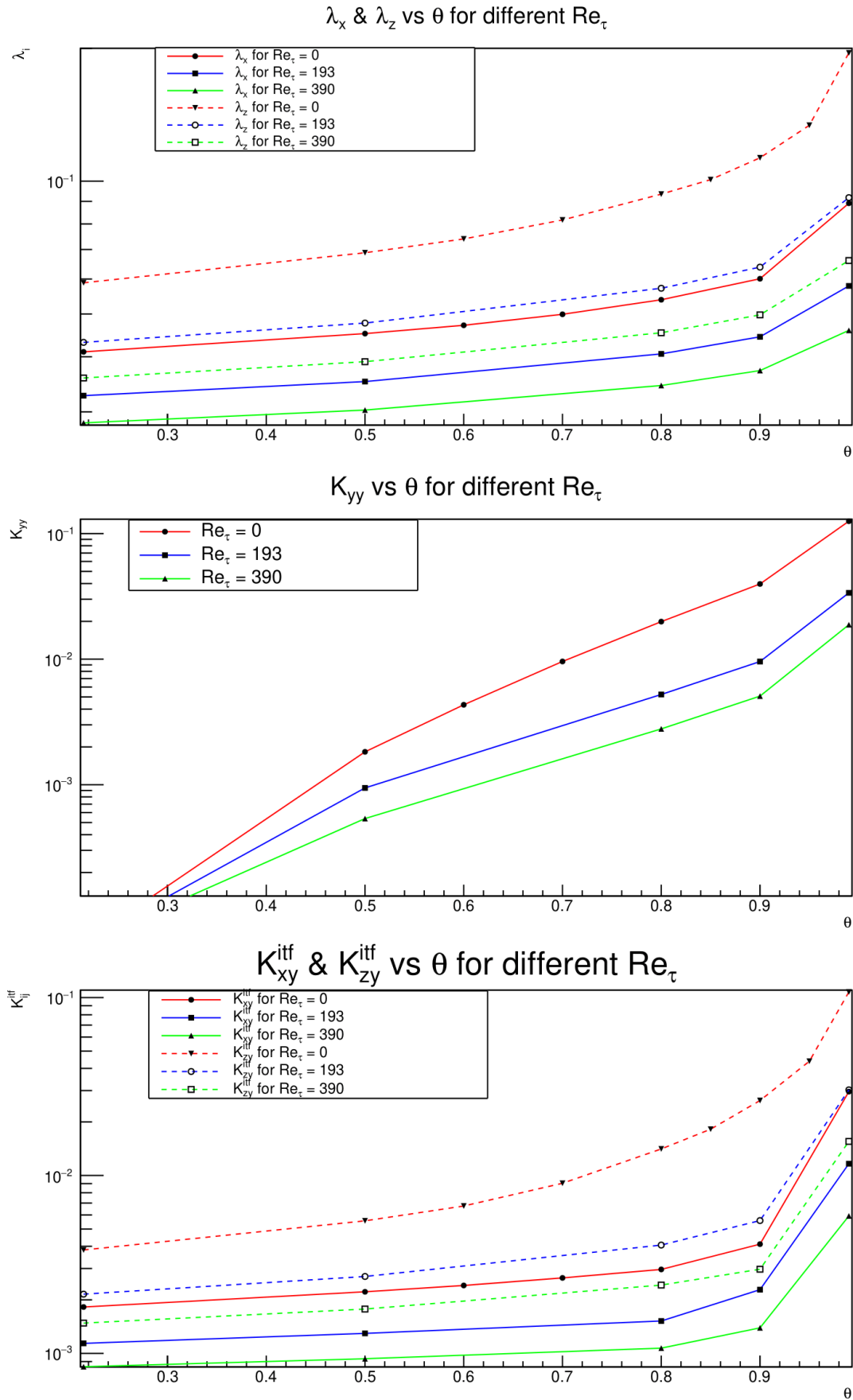
Figure 3.2.7: Graphs of Tables 4.5, 4.8, 4.9, i.e. of the parameters against θ for different Re_τ series (*inline* configuration and *spanwise* inclusions).
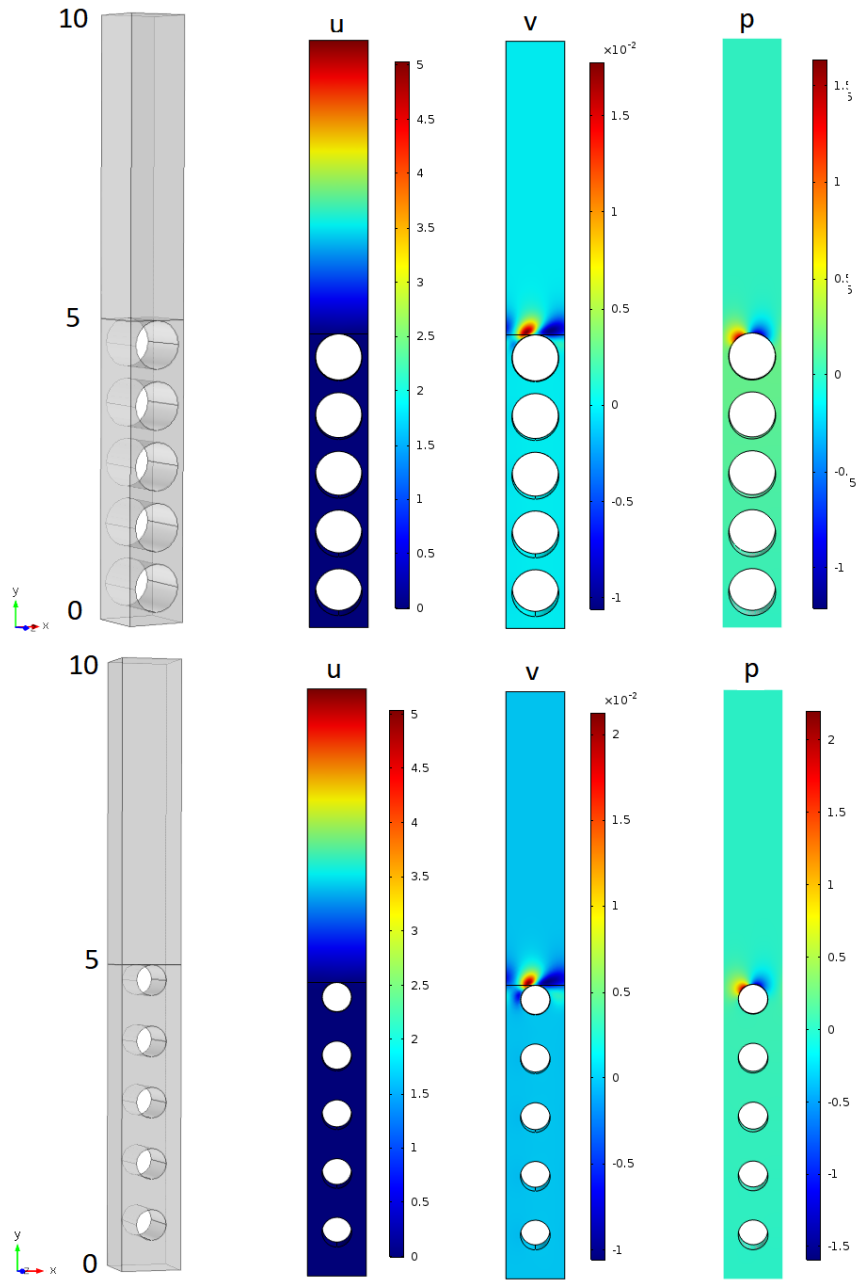
Figure 3.2.8: Velocity and pressure fields in the xy plain for $\theta = 0.50$ (above), $\theta = 0.80$ (below) and $Re_\tau = 193$ for the problem of shear along x, i.e. $\tilde{u}_{i1}$, in the spanwise configuration.
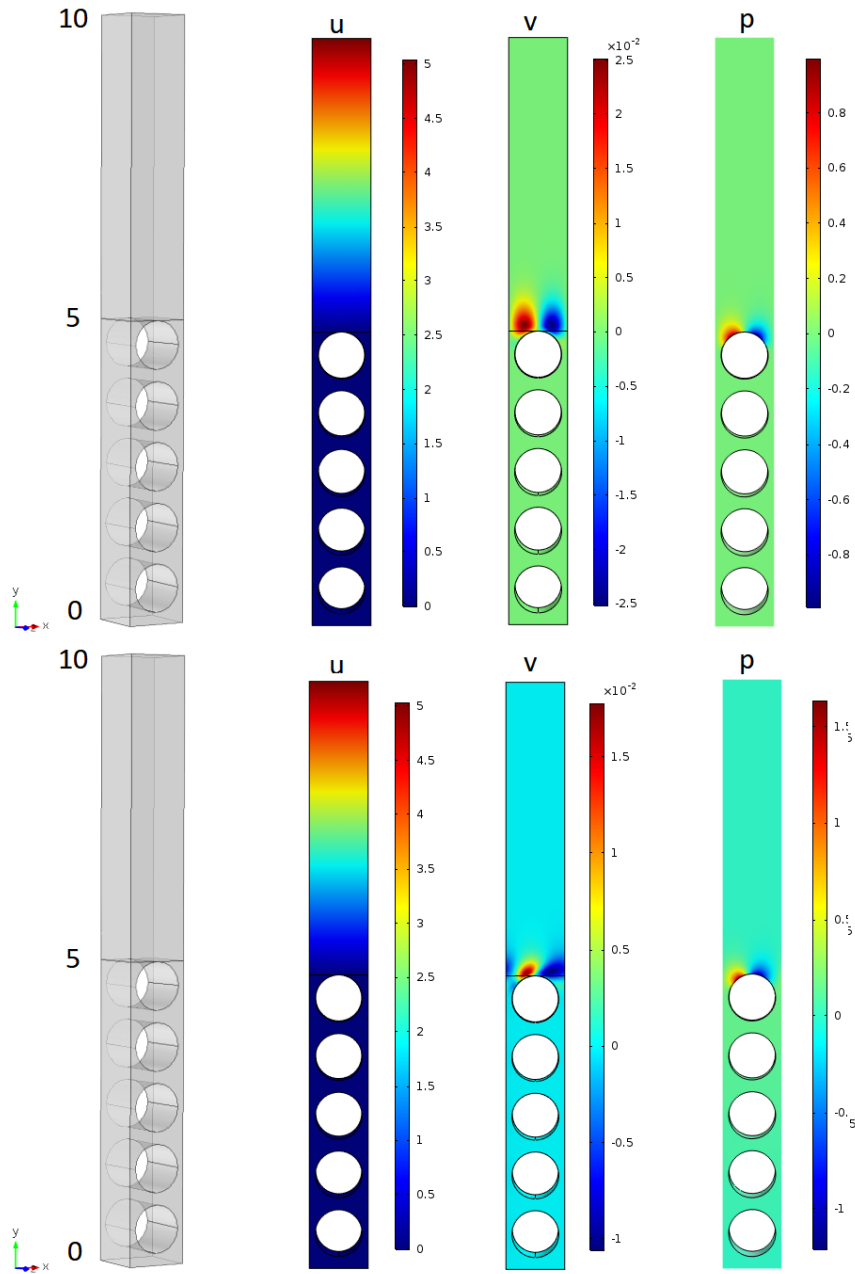
Figure 3.2.9: Velocity and pressure fields in the xy plain for $Re_\tau = 0$ (above), $Re_\tau = 193$ (below) and $\theta = 0.50$ for the problem of shear along x, i.e. $\tilde{u}_{i1}$, in the spanwise configuration.
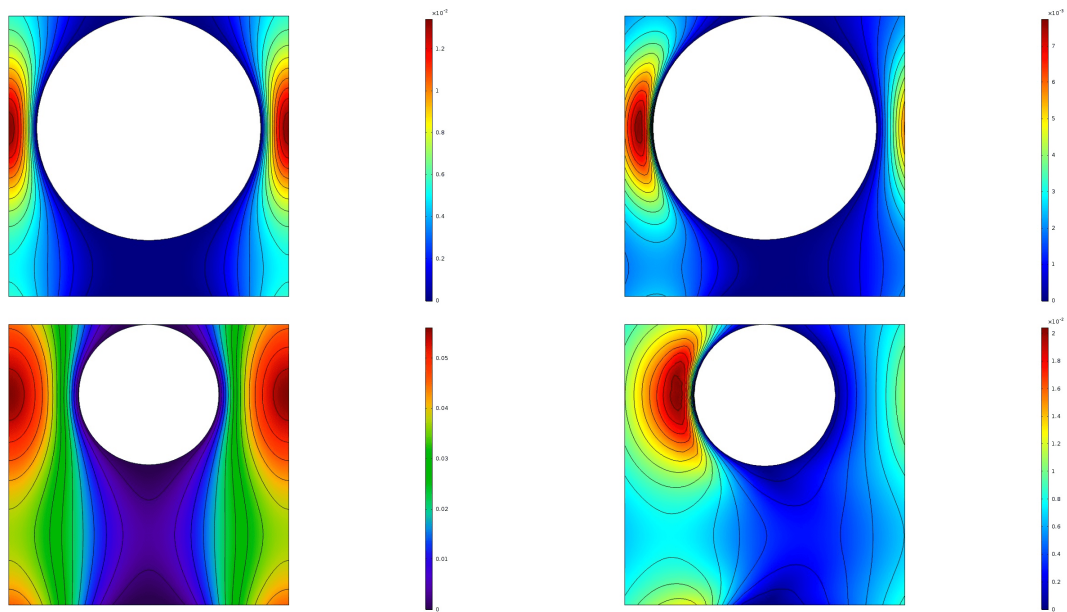
Figure 3.2.10: $\mathcal{K}_{yy}$ in the fully periodic unit cell for $\theta = 0.50$ (top), $\theta = 0.80$ (bottom) and for $Re_\tau = 0$ (sx), $Re_\tau = 193$ (dx), in the spanwise configuration.
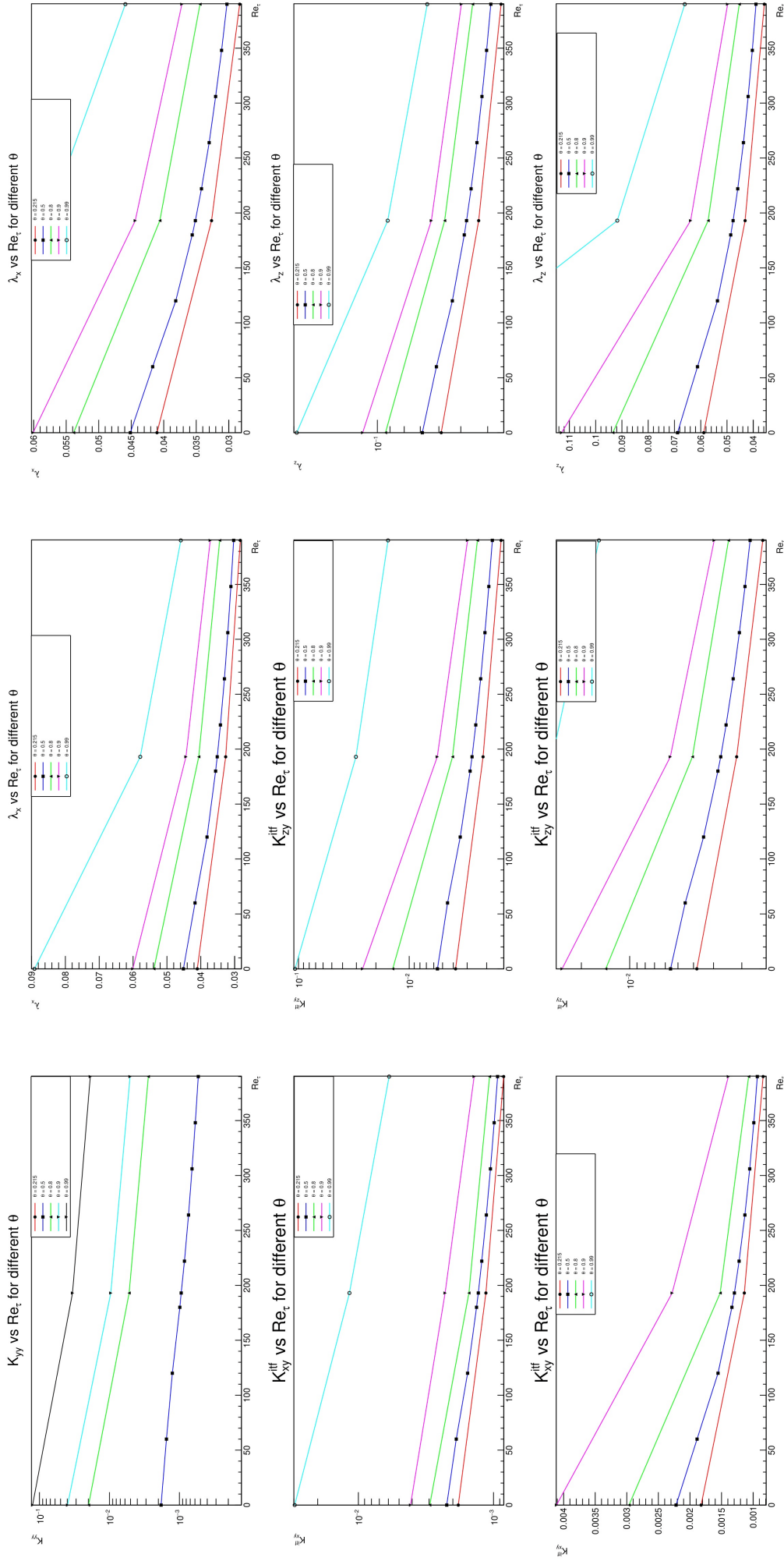
Figure 3.2.11: Graphs of Tables 4.10, 4.7, 4.11, 4.12, 4.13, i.e. of the parameters against Re_τ for different θ series (*inline* configuration and *spanwise* inclusions).

74

3.2.2 Streamwise Cylinders
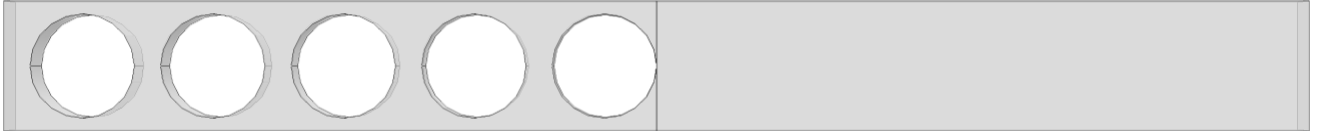
Figure 3.2.12: System geometry for streamwise-aligned cylinders. View in the $y-z$ plain.

We now change the (microscopic) geometry by changing only the direction of the axes of the cylinders (see fig. 3.2.12), from spanwise (aligned along z) to streamwise (aligned along x).

We then calculate the parameters for $\theta = 0.5$ and different Re_τ in the interval $[0, 264]$ (with $\epsilon = 0.2$). The non zero parameters arise from the same problems of spanwise cylinders, and, in principle, the calculation can be carried out in the same manner. As before, $\mathcal{K}_{xy}^{itf}$ and $\mathcal{K}_{zy}^{itf}$ have been calculated directly from the $\mathcal{O}(1)$ simulations. Moreover, $\mathcal{K}_{yy}$ has been always calculated in the elongated domain. Indeed, we found further simplifications. Numerical values are reported in table 4.14.

By first, we observe that there is no dependence of the parameters on Re_τ, recovering the Stokes' results for every Re_τ (see also fig. 3.2.13). This is because we supposed to have convection only along x and, since, in this case, from homogeneity, $\frac{\partial \cdot}{\partial x} = 0$, the Oseen term $-\epsilon Re_\tau \partial_x u_i$ is always zero.

Secondly, we observe that, approximately, the values of the parameters in this case are simply the ones of the corresponding Stokes' simulations with spanwise cylinders but switched, i.e. $\lambda_x|_{\text{stream}, \forall \epsilon Re_\tau} \approx \lambda_z|_{\text{span}, Re_\tau=0}$, $\lambda_z|_{\text{stream}, \forall \epsilon Re_\tau} \approx \lambda_x|_{\text{span}, Re_\tau=0}$, $\mathcal{K}_{xy}^{itf}|_{\text{stream}, \forall \epsilon Re_\tau} \approx \mathcal{K}_{zy}^{itf}|_{\text{span}, Re_\tau=0}$ and $\mathcal{K}_{zy}^{itf}|_{\text{stream}, \forall \epsilon Re_\tau} \approx \mathcal{K}_{xy}^{itf}|_{\text{span}, Re_\tau=0}$. Whereas for medium permeability, one finds $\mathcal{K}_{yy}|_{\text{stream}, \forall \epsilon Re_\tau} \approx \mathcal{K}_{yy}|_{\text{span}, Re_\tau=0}$. Anyhow, since these results are approximated, we preferred to simulate everything from start.
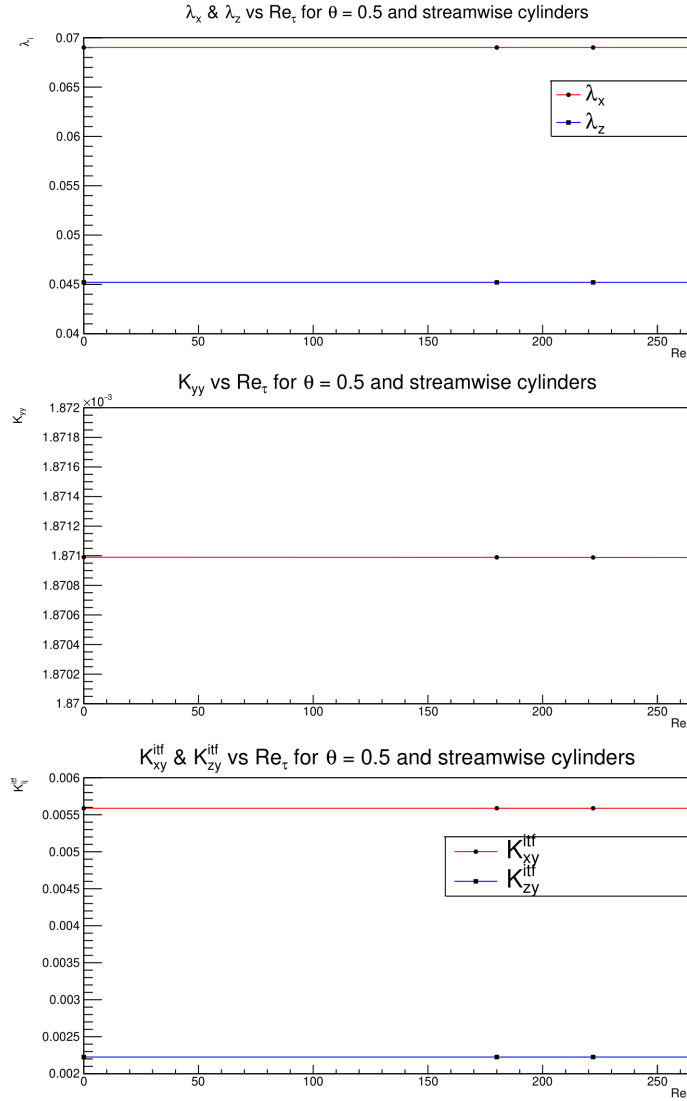
Figure 3.2.13: Graphs of Table 4.14, i.e. of the parameters against Re_τ for $\theta = 0.5$ (*inline* configuration and *spanwise* inclusions). This graph tells us that, in this streamwise configuration, the parameters are ϵRe_τ independent. Furthermore, streamwise parameters are directly available from the Stokes' spanwise ones by performing the following operations: $f_x|_{\text{stream}, \forall \epsilon Re_\tau} \approx f_z|_{\text{span}, Re_\tau = 0}$ (and *viceversa* for the z component), where $f_i = \lambda_i, \mathcal{K}_{iy}^{itf}$ (for $i = x, z$), and $\mathcal{K}_{yy}|_{\text{stream}, \forall \epsilon Re_\tau} \approx \mathcal{K}_{yy}|_{\text{span}, Re_\tau = 0}$.

In the end, the coefficients for the case of streamwise-aligned cylinders for every Re_τ (always in this Oseen approximation) are directly available from the Stokes' ones with spanwise-aligned cylinders, with the simply above mentioned replacements.

Furthermore, also this time, in figure 3.2.14, velocity and pressure fields are shown in the yz plain for the shear-along-x problem (i.e. $\tilde{u}_{i1}$), just for one case ($\theta = 0.5$, $Re_\tau = 0$).

Moreover, figure 3.2.15 shows $\mathcal{K}_{yy}$ in the elongated domain for one simple case. With the above consideration, it's clear why this picture is similar to the one of the corresponding spanwise case, changing only the axes orientation.
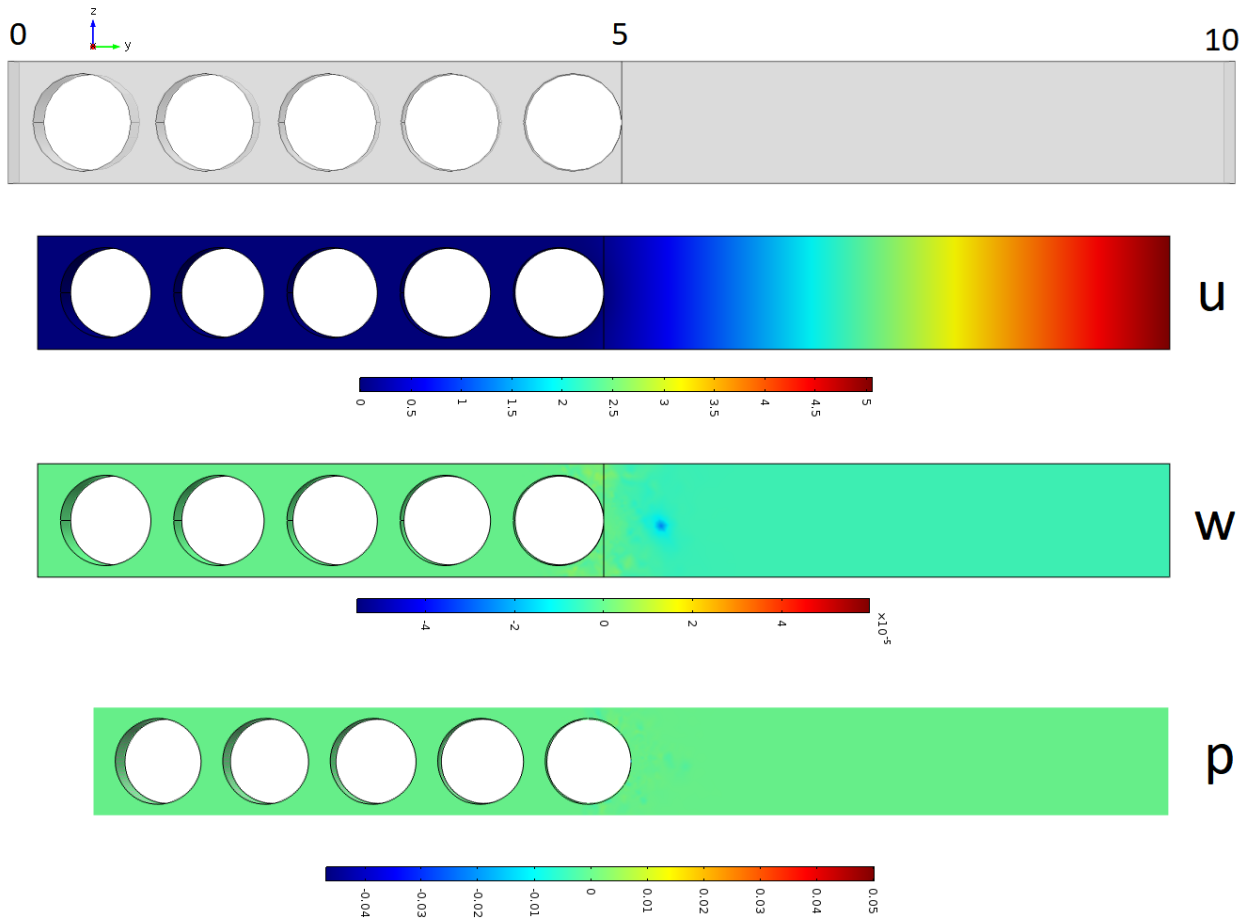
Figure 3.2.14: Velocity and pressure fields in the yz plain for $\theta = 0.50$ and $Re_\tau = 0$ for the problem of shear along x, i.e. $\tilde{u}_{i1}$, in the streamwise configuration.
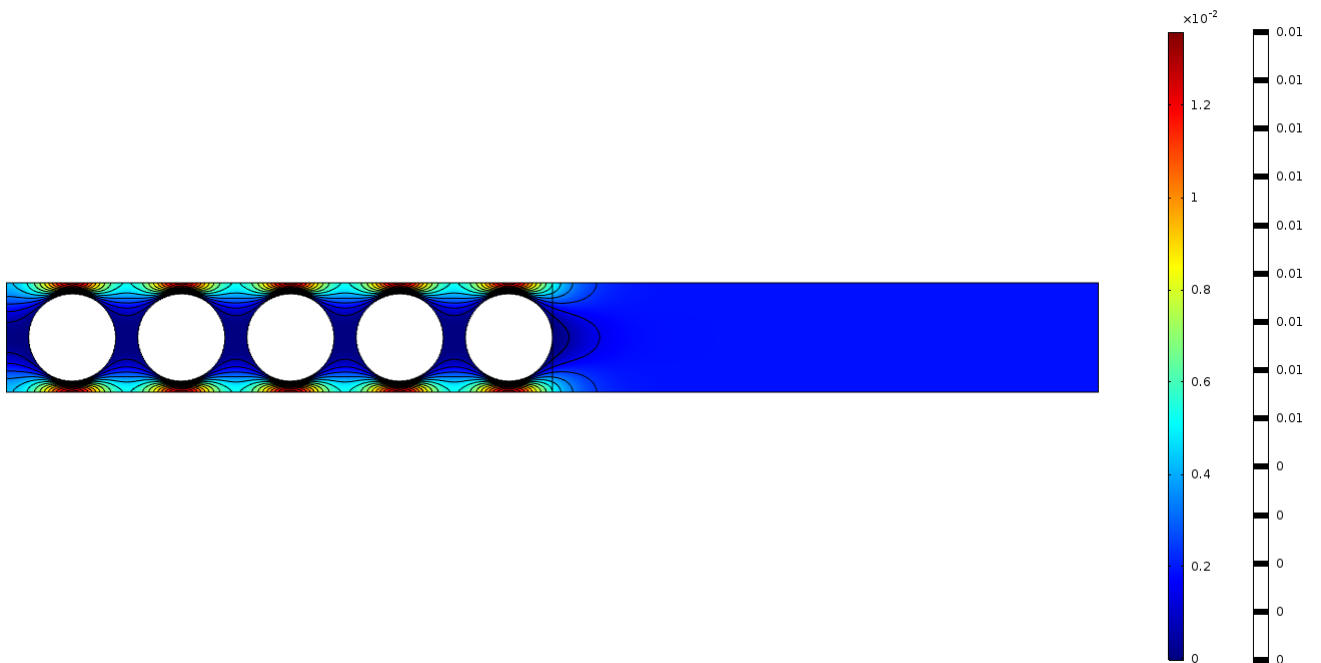
Figure 3.2.15: $\mathcal{K}_{yy}$ in the elongated domain for $\theta = 0.50$, $Re_\tau = 0$ in the spanwise configuration.

3.2.3 Boundary condition

Based on previous results, the macroscopic boundary condition, enforced at $Y = 0^+$, assumes the following form

$$U|_{Y=0^+} = \epsilon \lambda_x S_{12}|_{Y=0^+} + \epsilon^2 \mathcal{K}_{xy}^{itf} \frac{\partial S_{22}}{\partial X}\bigg|_{Y=0^+} + \mathcal{O}\left(\epsilon^3\right) \qquad (3.2.21)$$

$$V|_{Y=0^+} = -\epsilon^2 \mathcal{K}_{xy}^{itf} \frac{\partial S_{12}}{\partial X}\bigg|_{Y=0^+} - \epsilon^2 \mathcal{K}_{zy}^{itf} \frac{\partial S_{32}}{\partial Z}\bigg|_{Y=0^+} + \epsilon^2 \mathcal{K}_{yy} \frac{\partial S_{22}}{\partial Y}\bigg|_{Y=0^+} + \mathcal{O}\left(\epsilon^3\right) \qquad (3.2.22)$$

$$W|_{Y=0^+} = \epsilon \lambda_z S_{32}|_{Y=0^+} + \epsilon^2 \mathcal{K}_{zy}^{itf} \frac{\partial S_{22}}{\partial Z}\bigg|_{Y=0^+} + \mathcal{O}\left(\epsilon^3\right) \qquad (3.2.23)$$

where S_{j2} are the following component of the traction vector at $Y = 0^+$

$$S_{12} = \frac{\partial U}{\partial Y} + \frac{\partial V}{\partial X}\bigg|_{Y=0^+}, \quad S_{22} = -ReP + 2\frac{\partial V}{\partial Y}\bigg|_{Y=0^+}, \quad S_{32} = \frac{\partial W}{\partial Y} + \frac{\partial V}{\partial Z}\bigg|_{Y=0^+} \qquad (3.2.24)$$

and where the following effective coefficients have been defined:

$$\lambda_{x,z} = \tilde{u}_{11,33}|_{y_\infty=0}, \quad \mathcal{K}_{yy} = u_{222}^{\ddagger}\bigg|_{y_\infty=0} \quad \mathcal{K}_{xy,zy}^{itf} = u_{121,323}^{\ddagger}\bigg|_{y_\infty=0} = -u_{211,233}^{\ddagger}\bigg|_{y_\infty=0}. \qquad (3.2.25)$$

We can write these conditions in dimensional form:

$$\hat{u}|_{0^+} \approx \hat{\lambda}_x \left(\frac{\partial \hat{u}}{\partial \hat{y}} + \frac{\partial \hat{v}}{\partial \hat{x}}\right)\bigg|_{0^+} + \frac{\hat{\mathcal{K}}_{xy}^{itf}}{\mu} \frac{\partial}{\partial \hat{x}}\left(-\hat{p} + 2\mu \frac{\partial \hat{v}}{\partial \hat{y}}\right)\bigg|_{0^+} \qquad (3.2.26)$$

$$\hat{v}|_{0^+} \approx \frac{\hat{\mathcal{K}}_{yy}}{\mu} \frac{\partial}{\partial \hat{y}}\left(-\hat{p} + 2\mu \frac{\partial \hat{v}}{\partial \hat{y}}\right)\bigg|_{0^+} - \hat{\mathcal{K}}_{xy}^{itf} \frac{\partial}{\partial \hat{x}}\left(\frac{\partial \hat{u}}{\partial \hat{y}} + \frac{\partial \hat{v}}{\partial \hat{x}}\right)\bigg|_{0^+} - \hat{\mathcal{K}}_{zy}^{itf} \frac{\partial}{\partial \hat{z}}\left(\frac{\partial \hat{w}}{\partial \hat{y}} + \frac{\partial \hat{v}}{\partial \hat{z}}\right)\bigg|_{0^+} \qquad (3.2.27)$$

$$\hat{w}|_{0^+} \approx \hat{\lambda}_z \left(\frac{\partial \hat{w}}{\partial \hat{y}} + \frac{\partial \hat{v}}{\partial \hat{z}}\right)\bigg|_{0^+} + \frac{\hat{\mathcal{K}}_{zy}^{itf}}{\mu} \frac{\partial}{\partial \hat{z}}\left(-\hat{p} + 2\mu \frac{\partial \hat{v}}{\partial \hat{y}}\right)\bigg|_{0^+} \qquad (3.2.28)$$

where $\hat{\lambda}_{x,z} = \lambda_{x,z} l$, $\hat{\mathcal{K}}_{xy,zy}^{itf} = \mathcal{K}_{xy,zy}^{itf} l^2$ and $\hat{\mathcal{K}}_{yy} = \mathcal{K}_{yy} l^2$. Alternatively, writing the dimensional coefficients in terms of the macroscopic length L (for example a channel-half height), which is more useful for our purpose, we have $\hat{\lambda}_{x,z} =$

$(\epsilon\lambda_{x,\,z})\,L$, $\hat{\mathcal{K}}^{itf}_{xy,\,zy} = (\epsilon^2\mathcal{K}^{itf}_{xy,\,zy})\,L^2$ and $\hat{\mathcal{K}}_{yy} = (\epsilon^2\mathcal{K}_{yy})\,L^2$. Then, if we choose $L = 1\,m$, we have

$$
\begin{aligned}
\hat{\lambda}_{x,\,z} &= (\epsilon\lambda_{x,\,z})\,m \\
\hat{\mathcal{K}}^{itf}_{xy,\,zy} &= (\epsilon^2\mathcal{K}^{itf}_{xy,\,zy})\,m^2 \\
\hat{\mathcal{K}}_{yy} &= (\epsilon^2\mathcal{K}_{yy})\,m^2
\end{aligned}
\tag{3.2.29}
$$

which will be a useful result for our next development.

With the above conditions, there is no direct coupling between the Navier-Stokes and the Darcy regions and the two problems can be solved separately: once the outer flow problem is solved for, the pore pressure at leading order within the isotropic porous medium is a harmonic function which satisfies the Laplace equations, while at the dividing line one must take into account a Dirichlet condition, *infra* mentioned in the section devoted to Saffman's conditions.

Another way to express the above conditions is writing them in Saffman's form, i.e. in term of the pore pressure P_0^-. In dimensionless form, one has

$$
U|_{Y=0^+} = \epsilon\lambda_x S_{12}|_{Y=0^+} - \epsilon^2\mathcal{K}^{itf}_{xy}\frac{\partial P_0^-}{\partial X}\bigg|_{Y=0^-} + \mathcal{O}\left(\epsilon^3\right)
\tag{3.2.30}
$$

$$
V|_{Y=0^+} = -\epsilon^2\mathcal{K}^{itf}_{xy}\frac{\partial S_{12}}{\partial X}\bigg|_{Y=0^+} - \epsilon^2\mathcal{K}^{itf}_{zy}\frac{\partial S_{32}}{\partial Z}\bigg|_{Y=0^+} - \epsilon^2\mathcal{K}_{yy}\frac{\partial P_0^-}{\partial Y}\bigg|_{Y=0^-} + \mathcal{O}\left(\epsilon^3\right)
\tag{3.2.31}
$$

$$
W|_{Y=0^+} = \epsilon\lambda_z S_{32}|_{Y=0^+} - \epsilon^2\mathcal{K}^{itf}_{zy}\frac{\partial P_0^-}{\partial Z}\bigg|_{Y=0^-} + \mathcal{O}\left(\epsilon^3\right)
\tag{3.2.32}
$$

In this way, the motion in the free-fluid region is coupled to that in the porous medium: the two problems must be solved together, coupling to the Laplace equation for the pore pressure in the porous medium, i.e.

$$
\frac{\partial P_0^-}{\partial X_i}n_i = 0,
\tag{3.2.33}
$$

using the following equation, which expresses the balance of normal forces at the interface,

$$
P_0^-\big|_{Y=0^-} = P|_{Y=0^+} - \frac{2}{Re}\frac{\partial V}{\partial Y}\bigg|_{Y=0^+}
\tag{3.2.34}
$$

The same Saffman-like equations in dimensional form look like

$$
\hat{u}|_{0^+} \approx \hat{\lambda}_x\left(\frac{\partial\hat{u}}{\partial\hat{y}} + \frac{\partial\hat{v}}{\partial\hat{x}}\right)\bigg|_{0^+} - \frac{\hat{\mathcal{K}}^{itf}_{xy}}{\mu}\frac{\partial\hat{p}}{\partial\hat{x}}\bigg|_{0^-}
\tag{3.2.35}
$$

$$\hat{v}|_{0^+} \approx -\frac{\hat{\mathcal{K}}_{yy}}{\mu}\frac{\partial \hat{p}}{\partial \hat{y}}\bigg|_{0^-} - \hat{\mathcal{K}}_{xy}^{itf}\frac{\partial}{\partial \hat{x}}\left(\frac{\partial \hat{u}}{\partial \hat{y}} + \frac{\partial \hat{v}}{\partial \hat{x}}\right)\bigg|_{0^+} - \hat{\mathcal{K}}_{zy}^{itf}\frac{\partial}{\partial \hat{z}}\left(\frac{\partial \hat{w}}{\partial \hat{y}} + \frac{\partial \hat{v}}{\partial \hat{z}}\right)\bigg|_{0^+} \quad (3.2.36)$$

$$\hat{w}|_{0^+} \approx \hat{\lambda}_z\left(\frac{\partial \hat{w}}{\partial \hat{y}} + \frac{\partial \hat{v}}{\partial \hat{z}}\right)\bigg|_{0^+} - \frac{\hat{\mathcal{K}}_{zy}^{itf}}{\mu}\frac{\partial \hat{p}}{\partial \hat{z}}\bigg|_{0^-} \quad (3.2.37)$$

together with the Dirichlet condition for the pore pressure at the interface

$$\hat{p}|_{0^-} \approx \hat{p}|_{0^+} - 2\mu\frac{\partial \hat{v}}{\partial \hat{y}}\bigg|_{0^+} \quad (3.2.38)$$

3.3 The Stokes Limit

Mathematical Formulation   If $\epsilon^2 Re \ll 1$, the effective tensorial quantities directly arise from the solution of Stokes' problems. Indeed, we have
$\mathcal{O}(1)$:

$$\begin{cases} -\partial_i \tilde{p}_j + \partial_l^2 \tilde{u}_{ij} = 0 \\ \partial_i \tilde{u}_{ij} = 0 \\ \left(-\tilde{p}_j \delta_{i2} + \partial_2 \tilde{u}_{ij} + \partial_i \tilde{u}_{2j}\right)_{|y_\infty} = \delta_{ij} \end{cases} \tag{3.3.1}$$

which are three microscopic problems for $j = 1, 2, 3$.
$\mathcal{O}(\epsilon)$:

$$\begin{cases} \tilde{u}_{ij}\delta_{k1} = -\partial_i p_{jk}^{\ddagger} - \tilde{p}_j \delta_{ki} + \partial_l^2 u_{ijk}^{\ddagger} + 2\partial_k \tilde{u}_{ij} \\ \partial_i u_{ijk}^{\ddagger} = -\tilde{u}_{kj} \\ \left(-p_{jk}^{\ddagger}\delta_{i2} + \partial_2 u_{ijk}^{\ddagger} + \partial_i u_{2jk}^{\ddagger}\right)_{|y_\infty} = -\left(\tilde{u}_{ij}\delta_{k2} + \tilde{u}_{2j}\delta_{ik}\right)_{|y_\infty} \end{cases} \tag{3.3.2}$$

which are nine problems to be solved in the microscopic cell, for $j, k = 1, 2, 3$.

Once again, we explicitly write all the problems we need to solve, before considering any particular geometry.
At $\mathcal{O}(1)$, one has the following three problems:
$j = 1$:

$$\begin{cases} -\partial_i \tilde{p}_1 + \partial_l^2 \tilde{u}_{i1} = 0 \\ \partial_i \tilde{u}_{i1} = 0 \\ \boldsymbol{F}^S = (1, 0, 0) \end{cases} \tag{3.3.3}$$

$j = 2$:

$$\begin{cases} -\partial_i \tilde{p}_2 + \partial_l^2 \tilde{u}_{i2} = 0 \\ \partial_i \tilde{u}_{i2} = 0 \\ \boldsymbol{F}^S = (0, 1, 0) \end{cases} \tag{3.3.4}$$

$j = 3$:

$$\begin{cases} -\partial_i \tilde{p}_3 + \partial_l^2 \tilde{u}_{i3} = 0 \\ \partial_i \tilde{u}_{i3} = 0 \\ \boldsymbol{F}^S = (0, 0, 1) \end{cases} \tag{3.3.5}$$

where $\boldsymbol{F}^S$ is the (dimensionless) boundary stress imposed at y_∞.
For $j = 2$, one finds the simple analytical solution

$$\tilde{u}_{i2} = 0, \quad \tilde{p}_2 = -1. \tag{3.3.6}$$

These results will directly enter in the $\mathcal{O}(\epsilon)$ problems.
At $\mathcal{O}(\epsilon)$, one has the following nine problems:

$j = 1, k = 1$:

$$\begin{cases} -\partial_i p_{11}^{\ddagger} + \partial_l^2 u_{i11}^{\ddagger} - \tilde{u}_{i1} - \tilde{p}_1 \delta_{i1} + 2\partial_1 \tilde{u}_{i1} = 0 \\ \partial_i u_{i11}^{\ddagger} = -\tilde{u}_{11} \\ \boldsymbol{F}^S = \left(- \left. \tilde{u}_{21} \right|_{y_\infty}, 0, 0 \right) \end{cases} \tag{3.3.7}$$

$j = 1, k = 2$:

$$\begin{cases} -\partial_i p_{12}^{\ddagger} + \partial_l^2 u_{i12}^{\ddagger} - \tilde{p}_1 \delta_{i2} + 2\partial_2 \tilde{u}_{i1} = 0 \\ \partial_i u_{i12}^{\ddagger} = -\tilde{u}_{21} \\ \boldsymbol{F}^S = \left(- \left. \tilde{u}_{11} \right|_{y_\infty}, -2 \left. \tilde{u}_{21} \right|_{y_\infty}, - \left. \tilde{u}_{31} \right|_{y_\infty} \right) \end{cases} \tag{3.3.8}$$

$j = 1, k = 3$:

$$\begin{cases} -\partial_i p_{13}^{\ddagger} + \partial_l^2 u_{i13}^{\ddagger} - \tilde{p}_1 \delta_{i3} + 2\partial_3 \tilde{u}_{i1} = 0 \\ \partial_i u_{i13}^{\ddagger} = -\tilde{u}_{31} \\ \boldsymbol{F}^S = \left(0, 0, - \left. \tilde{u}_{21} \right|_{y_\infty} \right) \end{cases} \tag{3.3.9}$$

$j = 2, k = 1$:

$$\begin{cases} -\partial_i p_{21}^{\ddagger} + \partial_l^2 u_{i21}^{\ddagger} + \delta_{i1} = 0 \\ \partial_i u_{i21}^{\ddagger} = 0 \\ \boldsymbol{F}^S = (0, 0, 0) \end{cases} \tag{3.3.10}$$

$j = 2, k = 2$:

$$\begin{cases} -\partial_i p_{22}^{\ddagger} + \partial_l^2 u_{i22}^{\ddagger} + \delta_{i2} = 0 \\ \partial_i u_{i22}^{\ddagger} = 0 \\ \boldsymbol{F}^S = (0, 0, 0) \end{cases} \tag{3.3.11}$$

$j = 2, k = 3$:

$$\begin{cases} -\partial_i p_{23}^{\ddagger} + \partial_l^2 u_{i23}^{\ddagger} + \delta_{i3} = 0 \\ \partial_i u_{i23}^{\ddagger} = 0 \\ \boldsymbol{F}^S = (0, 0, 0) \end{cases} \tag{3.3.12}$$

$j = 3, k = 1$:

$$\begin{cases} -\partial_i p_{31}^{\ddagger} + \partial_l^2 u_{i31}^{\ddagger} - \tilde{u}_{i3} - \tilde{p}_3 \delta_{i1} + 2\partial_1 \tilde{u}_{i3} = 0 \\ \partial_i u_{i31}^{\ddagger} = -\tilde{u}_{13} \\ \boldsymbol{F}^S = \left(- \left. \tilde{u}_{23} \right|_{y_\infty}, 0, 0 \right) \end{cases} \tag{3.3.13}$$

$j = 3, k = 2$:

$$\begin{cases} -\partial_i p_{32}^{\ddagger} + \partial_l^2 u_{i32}^{\ddagger} - \tilde{p}_3 \delta_{i2} + 2\partial_2 \tilde{u}_{i3} = 0 \\ \partial_i u_{i32}^{\ddagger} = -\tilde{u}_{23} \\ \boldsymbol{F}^S = \left(- \left. \tilde{u}_{13} \right|_{y_\infty}, -2 \left. \tilde{u}_{23} \right|_{y_\infty}, - \left. \tilde{u}_{33} \right|_{y_\infty} \right) \end{cases} \tag{3.3.14}$$

$j = 3, k = 3$:

$$\begin{cases} -\partial_i p_{33}^{\ddagger} + \partial_l^2 u_{i33}^{\ddagger} - \tilde{p}_3 \delta_{i3} + 2\partial_3 \tilde{u}_{i3} = 0 \\ \partial_i u_{i33}^{\ddagger} = -\tilde{u}_{33} \\ \boldsymbol{F}^S = \left(0, 0, -\left.\tilde{u}_{23}\right|_{y_\infty}\right) \end{cases} \qquad (3.3.15)$$

We anticipate that, also this time, just as in the Oseen case, with our usual geometry, due to the solution of the $\mathcal{O}(1)$ problems, the $\mathcal{O}(\epsilon)$ problems simplify a little bit in the top boundary stress condition, as follows

$j = 1, k = 1$:

$$\begin{cases} -\partial_i p_{11}^{\ddagger} + \partial_l^2 u_{i11}^{\ddagger} - \tilde{u}_{i1} - \tilde{p}_1 \delta_{i1} + 2\partial_1 \tilde{u}_{i1} = 0 \\ \partial_i u_{i11}^{\ddagger} = -\tilde{u}_{11} \\ \boldsymbol{F}^S = (0, 0, 0) \end{cases} \qquad (3.3.16)$$

$j = 1, k = 2$:

$$\begin{cases} -\partial_i p_{12}^{\ddagger} + \partial_l^2 u_{i12}^{\ddagger} - \tilde{p}_1 \delta_{i2} + 2\partial_2 \tilde{u}_{i1} = 0 \\ \partial_i u_{i12}^{\ddagger} = -\tilde{u}_{21} \\ \boldsymbol{F}^S = \left(-\left.\tilde{u}_{11}\right|_{y_\infty}, 0, 0\right) \end{cases} \qquad (3.3.17)$$

$j = 1, k = 3$:

$$\begin{cases} -\partial_i p_{13}^{\ddagger} + \partial_l^2 u_{i13}^{\ddagger} - \tilde{p}_1 \delta_{i3} + 2\partial_3 \tilde{u}_{i1} = 0 \\ \partial_i u_{i13}^{\ddagger} = -\tilde{u}_{31} \\ \boldsymbol{F}^S = (0, 0, 0) \end{cases} \qquad (3.3.18)$$

$j = 2, k = 1$:

$$\begin{cases} -\partial_i p_{21}^{\ddagger} + \partial_l^2 u_{i21}^{\ddagger} + \delta_{i1} = 0 \\ \partial_i u_{i21}^{\ddagger} = 0 \\ \boldsymbol{F}^S = (0, 0, 0) \end{cases} \qquad (3.3.19)$$

$j = 2, k = 2$:

$$\begin{cases} -\partial_i p_{22}^{\ddagger} + \partial_l^2 u_{i22}^{\ddagger} + \delta_{i2} = 0 \\ \partial_i u_{i22}^{\ddagger} = 0 \\ \boldsymbol{F}^S = (0, 0, 0) \end{cases} \qquad (3.3.20)$$

$j = 2, k = 3$:

$$\begin{cases} -\partial_i p_{23}^{\ddagger} + \partial_l^2 u_{i23}^{\ddagger} + \delta_{i3} = 0 \\ \partial_i u_{i23}^{\ddagger} = 0 \\ \boldsymbol{F}^S = (0, 0, 0) \end{cases} \qquad (3.3.21)$$

$j = 3, k = 1$:

$$\begin{cases} -\partial_i p_{31}^{\ddagger} + \partial_l^2 u_{i31}^{\ddagger} - \tilde{u}_{i3} - \tilde{p}_3 \delta_{i1} + 2\partial_1 \tilde{u}_{i3} = 0 \\ \partial_i u_{i31}^{\ddagger} = -\tilde{u}_{13} \\ \boldsymbol{F}^S = (0, 0, 0) \end{cases} \qquad (3.3.22)$$

$j = 3, k = 2$:

$$\begin{cases} -\partial_i p_{32}^{\ddagger} + \partial_l^2 u_{i32}^{\ddagger} - \tilde{p}_3 \delta_{i2} + 2\partial_2 \tilde{u}_{i3} = 0 \\ \partial_i u_{i32}^{\ddagger} = -\tilde{u}_{23} \\ \boldsymbol{F}^S = \left(0, 0, -\tilde{u}_{33}|_{y_\infty}\right) \end{cases} \qquad (3.3.23)$$

$j = 3, k = 3$:

$$\begin{cases} -\partial_i p_{33}^{\ddagger} + \partial_l^2 u_{i33}^{\ddagger} - \tilde{p}_3 \delta_{i3} + 2\partial_3 \tilde{u}_{i3} = 0 \\ \partial_i u_{i33}^{\ddagger} = -\tilde{u}_{33} \\ \boldsymbol{F}^S = (0, 0, 0) \end{cases} \qquad (3.3.24)$$

We remember that all these problems are solved together with periodicity along x and z and with no-slip condition at the solid inclusions.

3.4 Numerical Solution for the Microscopic Stokes Case
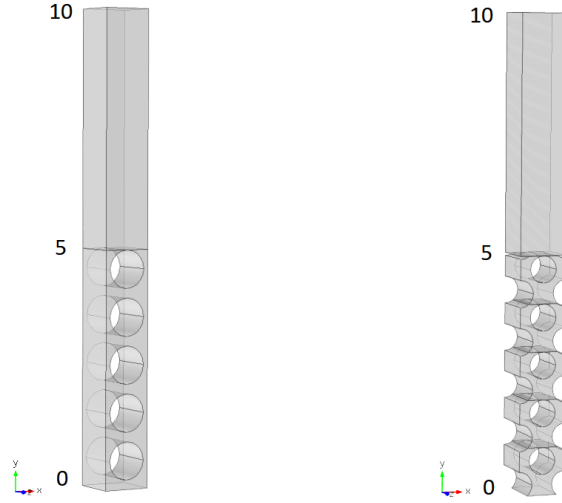
Figure 3.4.1: System geometry for the shear problem. (sx) inline arrangement (dx) staggered arrangement.

Figure 3.4.2: System geometry for the unit force problem. (sx) inline arrangement (dx) staggered arrangement.

Then, we numerically solved the Stokes' microscopic problems for both in-line and staggered cylindrical inclusions, arranged in spanwise direction, for different values of porosity (fig. 3.4.1, 3.4.2). The system geometry is the same as before, a part that now we also consider a staggered arrangement of cylindrical inclusions. For this latter configuration, since we have a total of two cylinders in the unit cell, the radius of the cylinders is divided by a factor $\sqrt{2}$ to keep the same value of porosity, i.e. $r = \sqrt{\frac{1-\theta}{2\pi}}$.

All the non zero coefficients at y_∞ are the same as before, i.e.

$$\lambda_{x,z} = \tilde{u}_{11,33}\big|_{y_\infty=0}, \quad \mathcal{K}_{yy} = u^{\ddagger}_{222}\big|_{y_\infty=0} \quad \mathcal{K}^{itf}_{xy,zy} = u^{\ddagger}_{121,323}\big|_{y_\infty=0} = -u^{\ddagger}_{211,233}\big|_{y_\infty=0}.$$

$$(3.4.1)$$

with the same trends in y_∞.

Furthermore, the same simplifying considerations of the Oseen case, can be made here *a fortiori*, i.e.

- $$\frac{1}{A} \int_S u^{\ddagger}_{ijk}\Big|_{y_\infty} \, \mathrm{d}S = u^{\ddagger}_{ijk}\Big|_{y_\infty}, \quad \frac{1}{A} \int_S \tilde{u}_{ij}|_{y_\infty} \, \mathrm{d}S = \tilde{u}_{ij}|_{y_\infty} \qquad (3.4.2)$$

  at the top of the domain.

- $$\begin{aligned} \mathcal{K}^{itf}_{xy} &= \int_{\mathcal{V}_{f\,Por}} \tilde{u}_{11} \, \mathrm{d}V \\ \mathcal{K}^{itf}_{zy} &= \int_{\mathcal{V}_{f\,Por}} \tilde{u}_{33} \, \mathrm{d}V \end{aligned} \qquad (3.4.3)$$

  already in the $\mathcal{O}(1)$ simulations.

- $$\mathcal{K}_{yy} = \int_{\mathcal{V}_f} u^{\ddagger}_{222} \, \mathrm{d}V \qquad (3.4.4)$$

  in the fully periodic unit cell.

- the other diagonal components of the medium permeability tensor can be computed in the following way:

  $$\begin{aligned} \mathcal{K}_{xx} &= \int_{\mathcal{V}_f} u^{\ddagger}_{121} \, \mathrm{d}V \\ \mathcal{K}_{zz} &= \int_{\mathcal{V}_f} u^{\ddagger}_{323} \, \mathrm{d}V \end{aligned} \qquad (3.4.5)$$

  always in the fully-periodic unit cell. We remark that, in this case, $\mathcal{K}_{xx}$ and $\mathcal{K}_{zz}$ do not correspond to any value of $u^{\ddagger}_{ijk}\Big|_{y_\infty=0}$. Hence, they do not enter the interface condition.

This time, we should recover the relationship $\mathcal{K}_{xx} \approx \mathcal{K}_{yy}$, at least for the inline configuration. We will see that for the staggered configuration, this relationship is only partially recovered, since in some cases (depending on geometrical parameters) the symmetry from which the above relationship arises is broken, because of the translation of the inclusions (made so that they are tangent to the interface). We remember that we are translating only the inclusions, not also the unit square containing them. Thus, we are left with a different periodic unit cell than the one we would have without translating the cylinders.

In figures 3.4.3, 3.4.4, velocity and pressure fields are shown in the xy plane for the shear-along-x problem (i.e. $\tilde{u}_{i1}$) for both inline and staggered arrangement, each for two different values of porosity, namely 0.50 and 0.80.
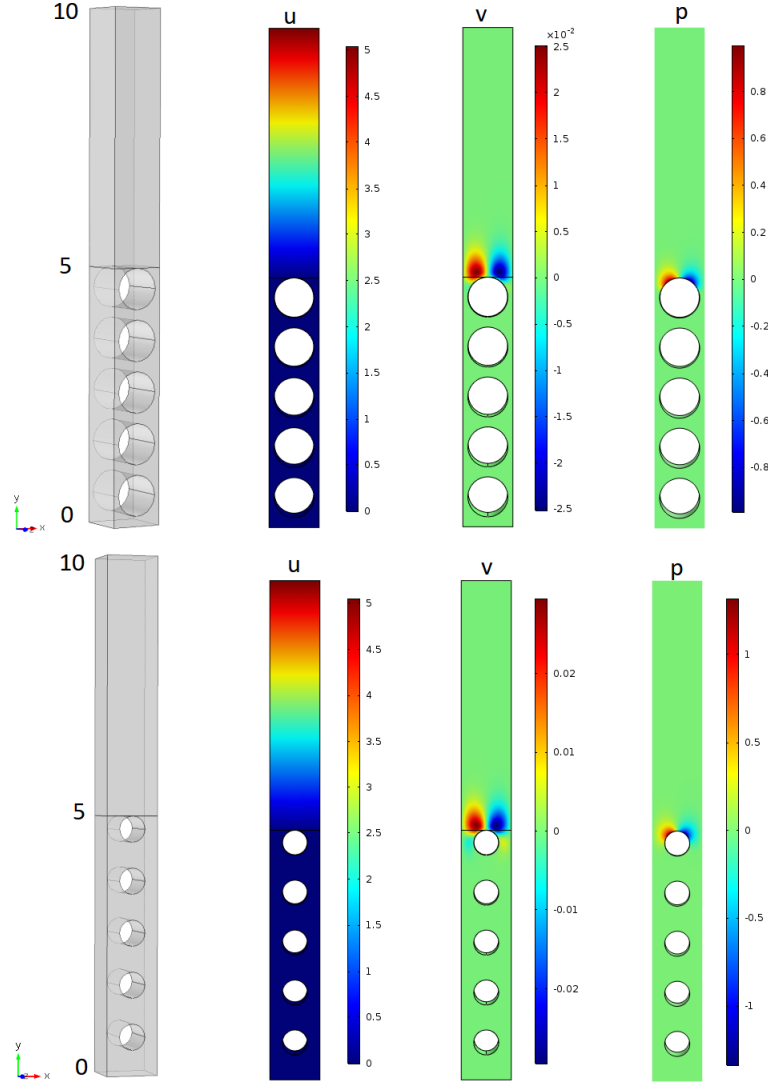
Figure 3.4.3: Velocity and pressure fields in the xy plain for $\theta = 0.50$ (above) and $\theta = 0.80$ (below) for inline solid grains for the problem of shear along x, i.e. $\tilde{u}_{i1}$.

Furthermore, $\mathcal{K}_{ii}$ for $i = x, y, z$ are shown in figure 3.4.5, for both inline and staggered arrangement and for $\theta = 0.50$ and $\theta = 0.80$. From this figure and also from tables 3.5, we notice that, for the inline case, we have $\mathcal{K}_{xx} \approx \mathcal{K}_{yy}$, which comes from the symmetry of unit cell. As a consequence of this symmetry, we also notice that (always in the inline case) $\mathcal{K}_{xx}$ and $\mathcal{K}_{yy}$ only differ in a $\pi/2$ rotation in figure 3.4.5. Instead, in the staggered configuration this symmetry is broken when the radius of the cylinders is less than a quarter of the cube length side, i.e. for $r < 0.25$. Thus, only for $\theta = 0.50$ we recover the relationship $\mathcal{K}_{xx} \approx \mathcal{K}_{yy}$, in the other cases the two permeabilities are different, as one can see by 3.6 and from fig. 3.4.5. This fact comes out from translating the cubes, keeping the cylinders fixed (or *viceversa*, which is equivalent) so that the first top cylinder is tangent to the interface beetween the free-fluid region and the porous medium. If we hadn't performed this translation, the symmetry would have been kept and the two permeabilities would have been
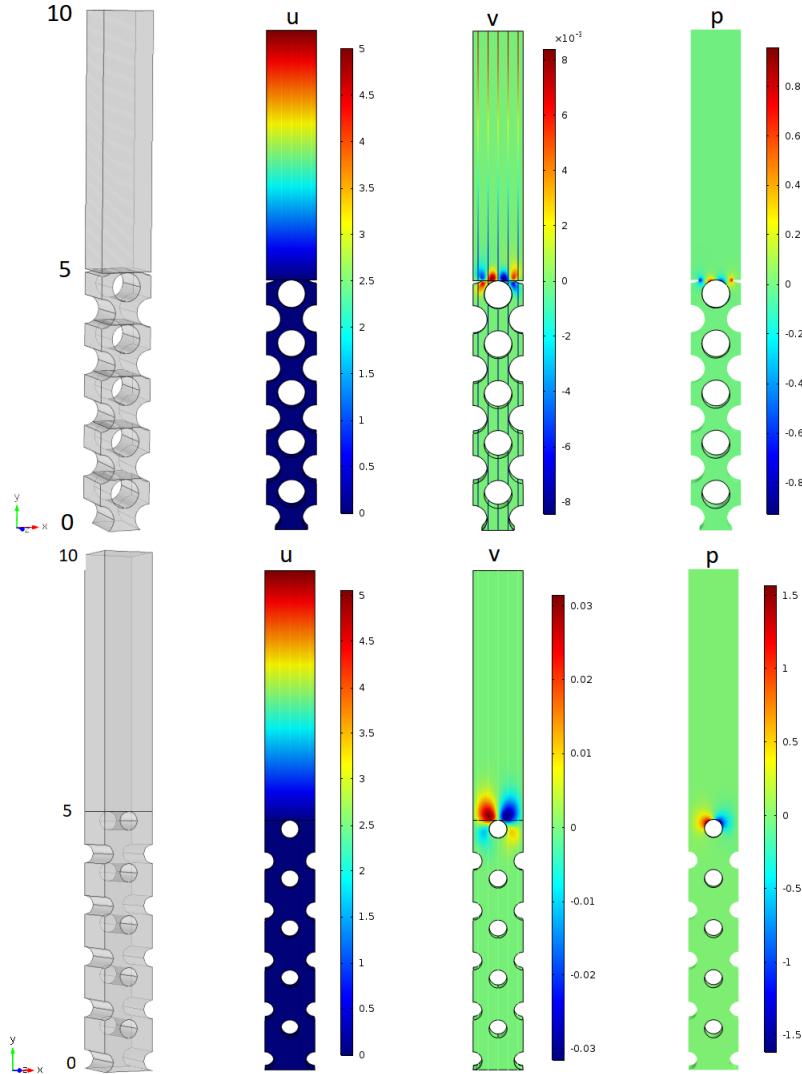
Figure 3.4.4: Velocity and pressure fields in the xy plain for $\theta = 0.50$ (above) and $\theta = 0.80$ (below) for staggered solid grains or the problem of shear along x, i.e. $\tilde{u}_{i1}$.

still numerically equal. We did this translation so that we can compare our results with full DNS by Chu et al. 2021.

Tables 4.5, 4.6 report numerical values of the parameters as porosity varies. We have considered $\theta \in [0.215, 0.99]$, adding also two extra point ($\theta = 0.85, 0.95$) when necessary. We should mention that high θ-values, in particular the value $\theta = 0.99$, are not representative of a realistic porous medium, except perhaps for the case of sparse canopies; nonetheless, we consider them to validate the correct trend, since we expect the parameters to have an abrupt, but continuous, jump at high θ.

As far as errors are concerned, we estimated an error for the porosity, coming from the fact that in Comsol, we truncated the corresponding value of the radius at a certain digit (two significant digits). Thus, if r_{trunc} is the truncated radius, we re-calculated porosity as $\theta_{true} = 1 - \pi r_{trunc}^2$ (or $\theta_{true} = 1 - 2\pi r_{trunc}^2$ for the staggered pattern), and defined the error over the porosity θ as $\sigma_\theta = |\theta - \theta_{true}|$ (see tables 3.3, 3.4). For $\theta = 0.215$, the error does not

θ	θ_{true}	σ_θ	r
0.2150	0.2146	0.0004	0.50
0.5000	0.4973	0.0027	0.40
0.600	0.593	0.007	0.36
0.7000	0.6981	0.0019	0.31
0.800	0.804	0.004	0.25
0.8500	0.8479	0.0021	0.22
0.9000	0.8982	0.0018	0.18
0.950	0.947	0.003	0.13
0.99000	0.99015	0.00015	0.056

$$(3.4.6)$$

Table 3.3: This table shows the calculation of the error on θ for the inline configuration.

θ	θ_{true}	σ_θ	r
0.2150	0.2146	0.0004	0.35
0.500	0.507	0.007	0.28
0.600	0.607	0.007	0.25
0.700	0.696	0.004	0.22
0.800	0.796	0.004	0.18
0.850	0.859	0.009	0.15
0.900	0.894	0.006	0.13
0.95000	0.95023	0.00023	0.089
0.99000	0.98995	0.00005	0.040

$$(3.4.7)$$

Table 3.4: This table shows the calculation of the error on θ for the staggered configuration.

θ	$\mathcal{K}_{xx}$	$\mathcal{K}_{yy}$
0.5000	$1.828E-03$	$1.827E-03$
0.800	$1.991E-02$	$1.990E-02$

$$(3.4.8)$$

Table 3.5: Comparison between $\mathcal{K}_{xx}$ and $\mathcal{K}_{yy}$ for restricted values of porosity, for the inline case.

θ	$\mathcal{K}_{xx}$	$\mathcal{K}_{yy}$
0.500	$1.008E-03$	$1.008E-03$
0.800	$1.153E-02$	$7.358E-03$
0.850	$1.975E-02$	$1.050E-02$

$$(3.4.9)$$

Table 3.6: Comparison between $\mathcal{K}_{xx}$ and $\mathcal{K}_{yy}$ for restricted values of porosity, for the staggered case.
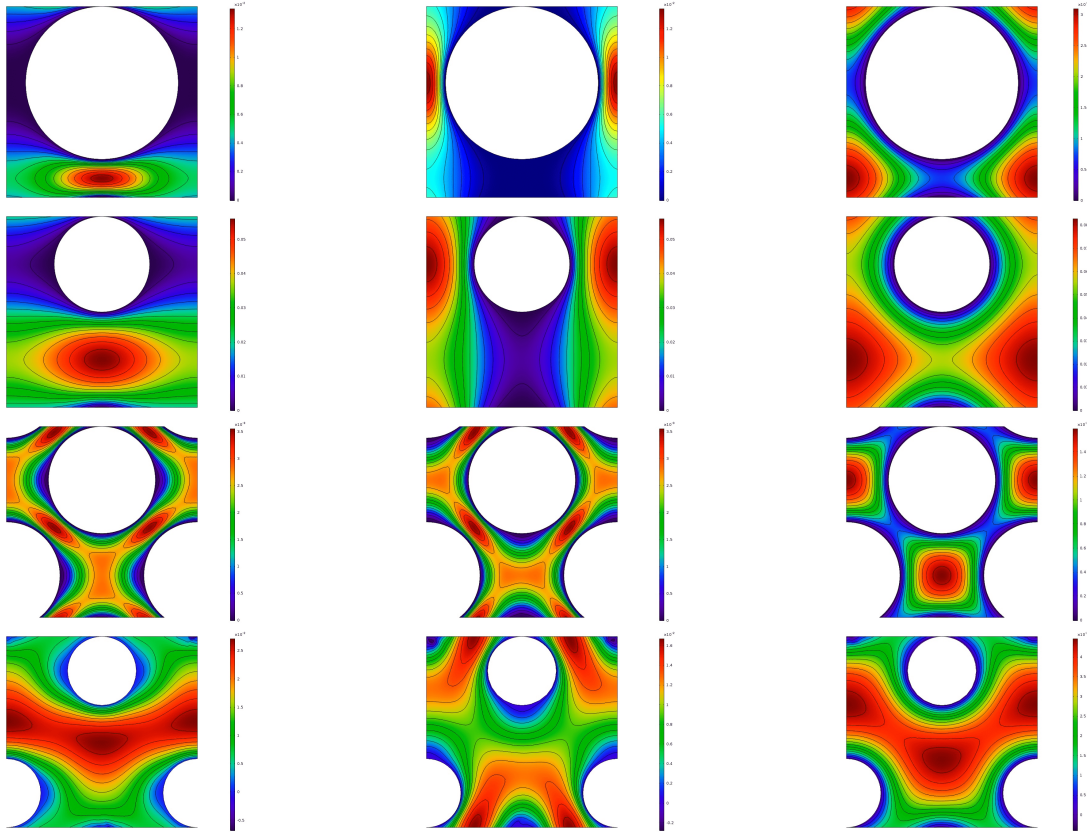
Figure 3.4.5: $\mathcal{K}_{ii}$ for $i = x, y, z$ (sx to dx) in the fully periodic unit cell both for inline (top) and staggered (bottom) pattern and for two different values of porosity, namely $\theta = 0.50$ (first and third row) and $\theta = 0.80$ (second and fourth row).

arise from the approximation of $r = 0.5$, which indeed is exact, but from the truncation of the corresponding porosity value itself (which should be $\theta = 1 - \frac{\pi}{4} \approx 0.2146\ldots$). The relative error is small, $\mathcal{O}(1\%)$, but not negligible, considering that, in principle, we are dealing with exact calculations and not with experimental measurements.

Finally, in figure 3.4.6 graphs of the parameters against porosity are shown, both for inline and staggered configurations. The coefficients have a monotonic behaviour with θ. One should also notice that K_{xy}^{itf} (inline pattern) varies very slowly for $\theta \in [0.215, 0.8]$ and then presents a sharp increase for $\theta \in [0.8, 0.99]$. This trend is also present in the other parameters, but with a less abrupt change, since for $\theta \in [0.215, 0.8]$ they vary more than K_{xy}^{itf} does in this range. We mention the for $\theta = 0.215$, which represents the minimum value of porosity ($r = 0.5$ for inline case), we have $\mathcal{K}_{yy} \approx 0$, consistently with the fact that, with this geometrical configuration, it is as if the surface is impermeable. For the staggered configuration, the medium permeabilities assume lower values with respect to the inline pattern at the same value of porosity. This is because, in staggered configuration, there is a non negligible portion of domain in which the fluid cannot penetrate. These results are in good agreement with the ones presented by Naqvi and Bottaro 2021.

λ_x & λ_z vs θ (inline and staggered pattern)

χ² / ndf	4.026 / 4	χ² / ndf	2.889 / 2	χ² / ndf	18.22 / 4	χ² / ndf	5.066 / 2
Prob	0.4025	Prob	0.2358	Prob	0.001118	Prob	0.07941
$A_{λ_{x,inlg}}$	0.06374 ± 0.003231	$A_{λ_{z,inlg}}$	0.01934 ± 0.001155	$A_{λ_{x,st}}$	0.05493 ± 0.001645	$A_{λ_{z,st}}$	0.0209 ± 0.0006622
β	0.9864 ± 0.04667	β	1.214 ± 0.0427	β	1.081 ± 0.02681	β	1.03 ± 0.02615
offset	0.07544 ± 0.0002457	offset	0.04665 ± 0.0002752	offset	0.05714 ± 0.0002256	offset	0.04027 ± 0.0001849
n	17.76 ± 1.724	n	14.22 ± 2.779	n	13.54 ± 1.122	n	16.76 ± 1.514
m	2.514 ± 0.1311	m	1.963 ± 0.1911	m	2.256 ± 0.08328	m	2.139 ± 0.1105

Legend:
- λ_x inline
- λ_z inline
- λ_x staggered
- λ_z staggered

K_yy & K_zz vs θ (inline and staggered pattern)

χ² / ndf	9.997 / 3	χ² / ndf	5.228 / 3	χ² / ndf	8.992 / 2
Prob	0.01859	Prob	0.1559	Prob	0.01116
$A_{K_{yy,inlg}}$	0.01045 ± 0.00425	$A_{K_{zz,inlg}}$	0.01836 ± 0.0009408	$A_{K_{yy,st}}$	0.08095 ± 0.00429
β	2.74 ± 0.377	β	1.267 ± 0.04517	β	1.319 ± 0.04817
offset	−0.005624 ± 0.004512	offset	−3.643e−05 ± 6.101e−06	offset	0.0009772 ± 3.203e−05
n	4.279 ± 0.6306	n	21.34 ± 4.846	n	11.49 ± 0.9241
m	0.3499 ± 0.2214	m	4.049 ± 0.1378	m	3.786 ± 0.114

χ² / ndf	3.075 / 2
Prob	0.2149
$A_{K_{zz,st}}$	0.05648 ± 0.002341
β	1.003 ± 0.03334
offset	−2.767e−05 ± 1.087e−05
n	16.66 ± 1.9
m	4.947 ± 0.09365

Legend:
- K_yy inline
- K_zz inline
- K_yy staggered
- K_zz staggered

K_{xy}^{itf} & K_{zy}^{itf} vs θ (inline and staggered pattern)

χ² / ndf	7.495 / 4	χ² / ndf	2.954 / 2	χ² / ndf	24.61 / 4	χ² / ndf	0.6415 / 2
Prob	0.1119	Prob	0.2283	Prob	6.035e−05	Prob	0.7256
$A_{K_{xy,inlg}^{itf}}$	0.03044 ± 0.001752	$A_{K_{zy,inlg}^{itf}}$	0.002895 ± 0.0004609	$A_{K_{xy,st}^{itf}}$	0.01453 ± 0.0007597	$A_{K_{zy,st}^{itf}}$	0.001789 ± 4.758e−05
β	1.418 ± 0.05503	β	2.758 ± 0.1425	β	2.197 ± 0.04888	β	3.323 ± 0.02452
offset	0.007817 ± 1.44e−05	offset	0.002426 ± 2.009e−05	offset	0.00366 ± 2.146e−05	offset	0.001715 ± 2.257e−05
n	16 ± 0.9046	n	9.34 ± 1.143	n	9.681 ± 0.4422	n	18.3 ± 0.6582
m	4.117 ± 0.1489	m	2.734 ± 0.3264	m	2.956 ± 0.1054	m	1.828 ± 0.1093

Legend:
- K_{xy}^{itf} inline
- K_{zy}^{itf} inline
- K_{xy}^{itf} staggered
- K_{zy}^{itf} staggered

Figure 3.4.6: Fit of Tables 4.5, 4.6, i.e. of the Stokes' parameters ($Re_\tau = 0$), for both *inline* and *staggered* pattern (*spanwise* inclusions). We used the fit function $f_{\text{fit}} : y = A\,x^m \exp(\beta\,x^n) + \text{offset}$, where y and x denote, respectively, dependent and independent variable and A, m, n and "offset" are free coefficients.

In fig. 3.4.6 data have also been fitted with the aid of ROOT libraries, using the following function:

$$f_{\text{fit}} : \quad y = A\,x^m \exp(\beta\,x^n) + \text{offset} \tag{3.4.10}$$

where y and x denotes, respectively, dependent and independent variable and A, m, n and "offset" are free coefficients.

Our fitting function is in good (and sometimes excellent) agreement with numerical results and faithfully reproduces the numerical trend, as one can see, by first, from direct inspection and, secondly, from the good χ^2-probability, almost well above the 5% threshold. For the staggered configurations, sometimes there is some point slightly to the limits of compatibility, suggesting that one could thicken the graphs with more numerical values. Anyhow, the trend is perfectly reproduced in both cases and we are fully satisfied.

3.4.1 Boundary condition

The macroscopic boundary condition to implement at $Y = 0^+$ in the Stokes' limit is the same than in the Oseen approximation, i.e.

$$U|_{Y=0^+} = \epsilon \lambda_x S_{12}|_{Y=0^+} + \epsilon^2 \mathcal{K}_{xy}^{itf} \left. \frac{\partial S_{22}}{\partial X} \right|_{Y=0^+} + \mathcal{O}\left(\epsilon^3\right) \qquad (3.4.11)$$

$$V|_{Y=0^+} = -\epsilon^2 \mathcal{K}_{xy}^{itf} \left. \frac{\partial S_{12}}{\partial X} \right|_{Y=0^+} - \epsilon^2 \mathcal{K}_{zy}^{itf} \left. \frac{\partial S_{32}}{\partial Z} \right|_{Y=0^+} + \epsilon^2 \mathcal{K}_{yy} \left. \frac{\partial S_{22}}{\partial Y} \right|_{Y=0^+} + \mathcal{O}\left(\epsilon^3\right)$$
$$(3.4.12)$$

$$W|_{Y=0^+} = \epsilon \lambda_z S_{32}|_{Y=0^+} + \epsilon^2 \mathcal{K}_{zy}^{itf} \left. \frac{\partial S_{22}}{\partial Z} \right|_{Y=0^+} + \mathcal{O}\left(\epsilon^3\right) \qquad (3.4.13)$$

where S_{j2} are the following component of the traction vector at $Y = 0^+$

$$S_{12} = \frac{\partial U}{\partial Y} + \left. \frac{\partial V}{\partial X} \right|_{Y=0^+}, \quad S_{22} = -ReP + 2 \left. \frac{\partial V}{\partial Y} \right|_{Y=0^+}, \quad S_{32} = \frac{\partial W}{\partial Y} + \left. \frac{\partial V}{\partial Z} \right|_{Y=0^+}$$
$$(3.4.14)$$

and where the following effective coefficients have been defined:

$$\lambda_{x,z} = \tilde{u}_{11,33}|_{y_\infty=0}, \quad \mathcal{K}_{yy} = u_{222}^\ddagger \big|_{y_\infty=0} \quad \mathcal{K}_{xy,zy}^{itf} = u_{121,323}^\ddagger \big|_{y_\infty=0} = -u_{211,233}^\ddagger \big|_{y_\infty=0}.$$
$$(3.4.15)$$

We can write these conditions in dimensional form:

$$\hat{u}|_{0^+} \approx \hat{\lambda}_x \left(\frac{\partial \hat{u}}{\partial \hat{y}} + \frac{\partial \hat{v}}{\partial \hat{x}} \right) \bigg|_{0^+} + \frac{\hat{\mathcal{K}}_{xy}^{itf}}{\mu} \frac{\partial}{\partial \hat{x}} \left(-\hat{p} + 2\mu \frac{\partial \hat{v}}{\partial \hat{y}} \right) \bigg|_{0^+} \qquad (3.4.16)$$

$$\hat{v}|_{0^+} \approx \frac{\hat{\mathcal{K}}_{yy}}{\mu} \frac{\partial}{\partial \hat{y}} \left(-\hat{p} + 2\mu \frac{\partial \hat{v}}{\partial \hat{y}} \right) \bigg|_{0^+} - \hat{\mathcal{K}}_{xy}^{itf} \frac{\partial}{\partial \hat{x}} \left(\frac{\partial \hat{u}}{\partial \hat{y}} + \frac{\partial \hat{v}}{\partial \hat{x}} \right) \bigg|_{0^+} - \hat{\mathcal{K}}_{zy}^{itf} \frac{\partial}{\partial \hat{z}} \left(\frac{\partial \hat{w}}{\partial \hat{y}} + \frac{\partial \hat{v}}{\partial \hat{z}} \right) \bigg|_{0^+}$$
$$(3.4.17)$$

$$\hat{w}|_{0^+} \approx \hat{\lambda}_z \left(\frac{\partial \hat{w}}{\partial \hat{y}} + \frac{\partial \hat{v}}{\partial \hat{z}} \right) \bigg|_{0^+} + \frac{\hat{\mathcal{K}}_{zy}^{itf}}{\mu} \frac{\partial}{\partial \hat{z}} \left(-\hat{p} + 2\mu \frac{\partial \hat{v}}{\partial \hat{y}} \right) \bigg|_{0^+} \qquad (3.4.18)$$

where $\hat{\lambda}_{x,z} = \lambda_{x,z} \, l$, $\hat{\mathcal{K}}_{xy,zy}^{itf} = \mathcal{K}_{xy,zy}^{itf} \, l^2$ and $\hat{\mathcal{K}}_{yy} = \mathcal{K}_{yy} \, l^2$.

Chapter 4

Macroscopic test: Fully-developed Turbulent Channel Flow

This chapter represents the second part of the original project of my thesis. We use our effective boundary condition to study the following macroscopic problem: a fully-developed turbulent channel flow at a moderate friction Reynolds number at the low wall. In particular, the upper wall will be a smooth wall, whereas the inferior wall will be an anisotropic porous rough wall. We imagine that below the inferior wall a porous medium is present, but we will concentrate our interest only in the channel flow. In our numerical calculations, carried out as a DNS (always technically done by two PhD students from the University of Genoa, Essam Abdo and Sahrish Naqvi, whom we sincerely thank), we will substitute the rough wall with a smooth wall, positioned, for the sake of convenience, at the same height of the previous rough one, at which we will apply our special interface slip condition. This procedure allows us to properly study the interaction between a three-dimensional turbulent boundary layer and a porous medium avoiding expensive fully-feature resolving DNS, thus saving computational time. Thus, the present modelisation, directly stemming from homogenisation theory, represents an alternative and innovative way to study such cases of interests, which indeed cover most of the interaction between a flow and natural/biological surfaces, possibly with industrial application, as widely seen in previous chapters.

In order to validate our solution, we will try to compare it with the fully-featuring resolving DNS made by Chu et al. 2021. However, very recently we discovered that, in this reference, important geometrical and dynamical quantities have different numerical values from ours. Thus, only a qualitative comparison is allowed. We will use both our Stokes and Oseen-like coefficients DNS, in order to see if there is a good agreement already with Stokes' co-

efficients and if there is an improvement with Oseen-like coefficients. These solutions will be carried out with spanwise-aligned inclusions, with $\theta = 0.5$, $Re_\tau = 193$ and $\epsilon = 0.2$. As previously mentioned, we have been careful of taking the inclusions tangent to the interface, at the level of microscopic simulations, as reported in the above mentioned reference paper.

Then we consider longitudinal inclusions to see if there is drag reduction with respect to the case of a smooth wall. We remember that, in this case, Oseen's coefficients reduce to Stokes' coefficients, which have been widely validated in the past. Indeed, as a reference, we will preliminarily carry out a simulation where also the inferior-channel wall is a smooth wall. Then, by changing the value of ϵ, we should be able to optimise this drag reduction, reconstructing the drag curve. In these simulations, we will take $Re_\tau = 193$, $\theta = 0.5$ and $\epsilon \in [0, 0.2]$. We remember that, with the previously computed coefficients, one should be able to study a variety of cases, changing θ and Re_τ, for both spanwise and streamwise-aligned (cylindrical) inclusions.

4.1   Spanwise inclusions: DNS validation

A DNS (Direct Numerical Simulation) study is a simulation at which the exact unsteady Navier-Stokes equations are solved throughout the domain, in order to resolve the behaviour of the different scales of turbulence eddies without the need of any sort of turbulence modelling.

These simulations have been carried out with the aid of the software STAR-CCM+ Multiphysics (entirely by two PhD students from the University of Genoa, Essam Abdo and Sahrish Naqvi, as previously mentioned), whose available license at the University of Genoa lacks most of the DNS utilities, such as turbulence statistics and monitors.

In the following discussion, the velocity components in the streamwise x-, wall normal y- and spanwise z-directions are denoted as u, v and w, respectively.

We consider a channel where the upper wall is a smooth wall, at which we apply a no-slip condition, while the inferior wall is originally a rough permeable wall with spanwise-aligned cylindrical porous elements of porosity $\theta = 0.5$ and of small parameter $\epsilon = 0.2$ (ratio between the porous length scale - say the interpore distance - and the outer, macroscopic one - say the half-channel height H), where a friction Reynolds number of $Re_\tau = 193$ can be defined as below. We substitute the permeable wall with a smooth wall positioned at the same height, at which we apply our effective boundary condition 3.2.26, 3.2.27, 3.2.28. We will use both the corresponding Stokes' and Oseen's coefficients, previously calculated (reported in tables 4.1, 4.2 for clarity), thus performing two different DNS. We will compare these results with

ϵRe_τ	Re_τ	λ_x	λ_z	$\mathcal{K}_{yy}$	$\mathcal{K}_{xy}^{itf}$	$\mathcal{K}_{zy}^{itf}$
0	0	$4.513\mathrm{E}-02$	$6.883\mathrm{E}-02$	$1.828\mathrm{E}-03$	$2.220\mathrm{E}-03$	$5.561\mathrm{E}-03$
39	193	$3.514\mathrm{E}-02$	$4.768\mathrm{E}-02$	$9.431\mathrm{E}-04$	$1.296\mathrm{E}-03$	$2.707\mathrm{E}-03$

(4.1.1)

Table 4.1: This table shows the numerical values of the (dimensionless) parameters of the effective boundary conditions applied at the lower wall in the DNS. The case is of spanwise-directed cylindrical inclusions, with $\theta = 0.5$ and $\epsilon = 0.2$. The first row represents Stokes' coefficients, while the second one is Oseen's coefficient at the indicated Re_τ.

ϵRe_τ	Re_τ	$\hat{\lambda}_x\,(m)$	$\hat{\lambda}_z\,(m)$	$\hat{\mathcal{K}}_{yy}\,(m^2)$	$\hat{\mathcal{K}}_{xy}^{itf}\,(m^2)$	$\hat{\mathcal{K}}_{zy}^{itf}\,(m^2)$
0	0	$9.027\mathrm{E}-03$	$1.377\mathrm{E}-02$	$7.312\mathrm{E}-05$	$8.879\mathrm{E}-05$	$2.224\mathrm{E}-04$
39	193	$7.028\mathrm{E}-03$	$9.537\mathrm{E}-03$	$3.773\mathrm{E}-05$	$5.184\mathrm{E}-05$	$1.083\mathrm{E}-04$

(4.1.2)

Table 4.2: This table shows the numerical values of the (dimensional, via 3.2.29) parameters of the effective boundary conditions applied at the lower wall in the DNS. The case is of spanwise-directed cylindrical inclusions, with $\theta = 0.5$ and $\epsilon = 0.2$. The first row represents Stokes' coefficients, while the second one is Oseen's coefficient at the indicated Re_τ.

the fully-feature resolving DNS made by Chu et al. 2021, at least qualitatively.
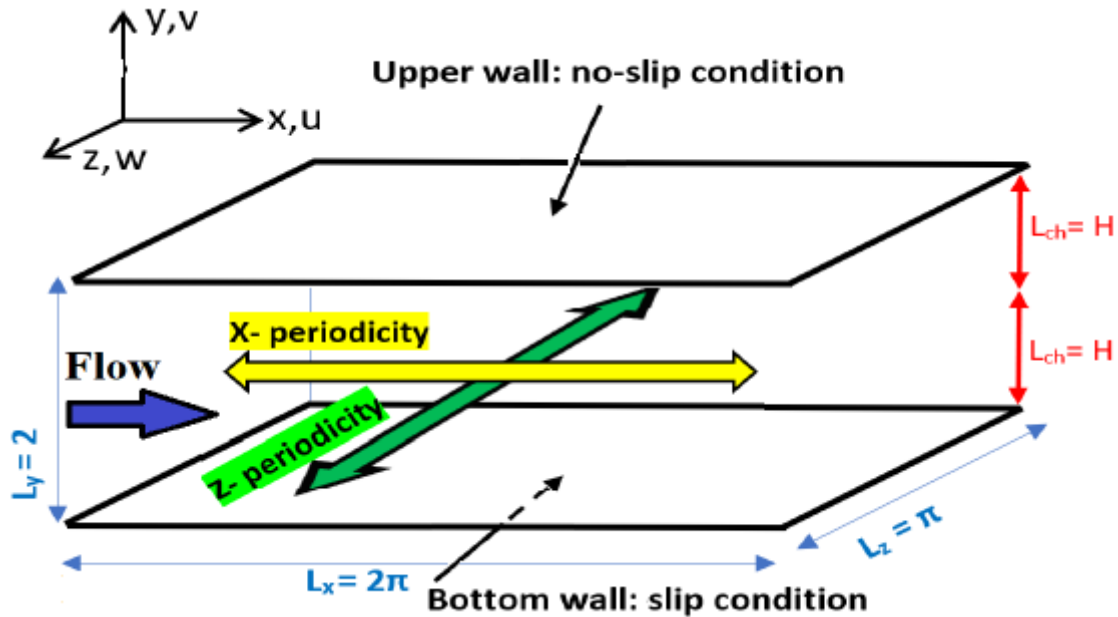
Figure 4.1.1: DNS computational domain, with explanations of length sides, directions, periodicity and boundary conditions.

Geometry and Setup We consider a channel of sides $(L_x, L_y, L_z) = (2\pi, 2, \pi)$, where we have normalised lengths with the channel half height $H = 1\,m$ (see fig. 4.1.1). We have selected this domain size in order to include the largest turbulence eddies in the proper way, as similarly presented by Kozuka, Seki, and Kawamura 2009. Due to the homogeneity of the fully-developed channel flow in the stream-wise and span-wise directions, it is reasonable to assume
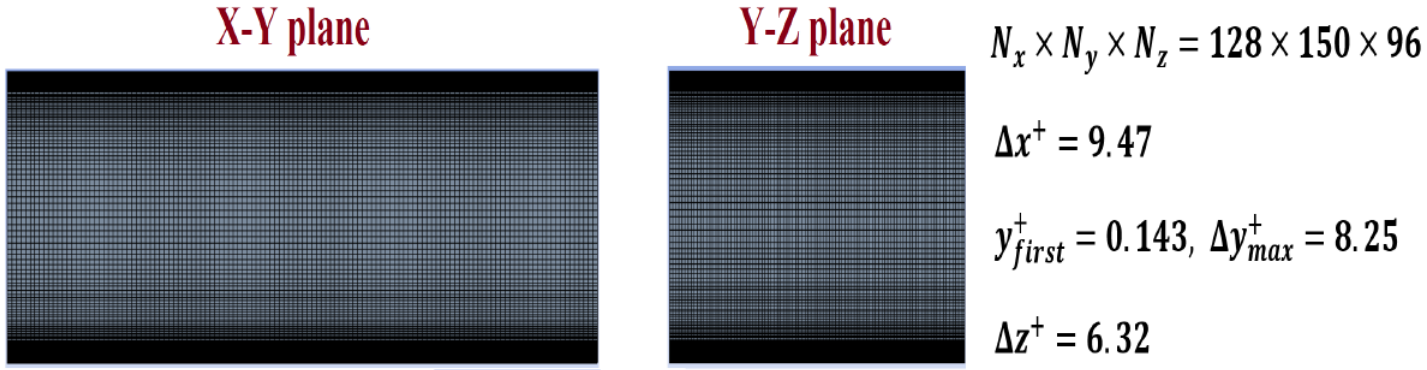
Figure 4.1.2: DNS mesh characteristics.

periodicity in these two directions. Furthermore, the flow is driven by imposing the constant source term $\boldsymbol{f} = (1,0,0)\,N/m^3$, which substitutes the (absent) pressure gradient. These choices, together with the equilibrium between the shear forces on the walls and the driving source term on the whole domain, lead to a wall shear stress on each wall of $1\,Pa$: $\tau_w = 1\,Pa$. Moreover, we remember that we want to impose a friction Reynolds number at the lower wall of 193, defined as $Re_\tau = \frac{u_\tau H}{\nu}$, where $u_\tau = \sqrt{\frac{\tau_w}{\rho}}$ is the friction velocity at the lower wall. In order to reach this target, we choose $\rho = 1\,kg/m^3$, so that $u_\tau = 1\,m/s$, which leads to $\nu = \frac{u_\tau H}{Re_\tau} = Re_\tau^{-1}\,m^2/s \approx 5.18 \cdot 10^{-3}\,m^2/s$. As far as normalisation is concerned, the normal distance y and the grid spacings $(\Delta_x, \Delta_y, \Delta_z)$ are normalised with the length scale $\frac{\nu}{u_\tau}$, so that the dimensionless parameters y^+ and $(\Delta_x^+, \Delta_y^+, \Delta_z^+)$ are defined. The velocity components (u, v, w) as well as the RMS of the velocity fluctuations $(u_{\mathrm{rms}}, v_{\mathrm{rms}}, w_{\mathrm{rms}})$ are normalised with the shear velocity u_τ. Sometimes, it is more suitable to normalise some parameters according to global coordinates: as seen, the domain dimensions are normalised with H and the mean streamwise velocity component will be occasionally normalised with the channel bulk average velocity U_{bulk}. As far as the mesh is concerned, the number of cells is given by $(N_x, N_y, N_z) = (128, 150, 96)$; graphical visualisation can be found in figure 4.1.2.

Turbulent statistics and main monitored parameters   All statistics were formulated using user-defined functions. This included the following calculations

- mean velocity by time-averaging

- velocity fluctuations to get the RMS values

- mean values of the Reynolds stresses
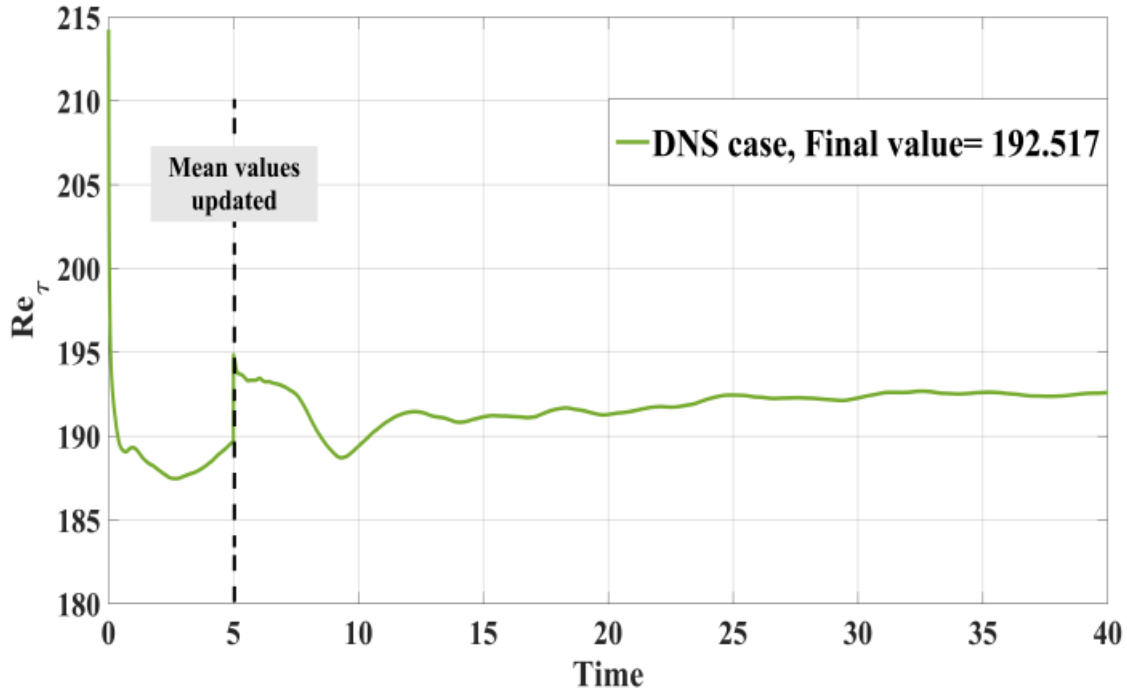
Figure 4.1.3: Behaviour of Re_τ vs. time for the DNS study.

The main monitored parameter to assess the convergence of statistics was Re_τ on the lower wall (see fig. 4.1.3). We based the calculation on the mean value of the wall shear stress averaged over the lower surface. The calculation of the mean value was updated after some time in order to avoid the effect of the initial transient.

Mean Velocity profile The DNS results of the streamwise velocity at all grid points were averaged through time to get mean values. Moreover, the values of the mean streamwise velocity at each normal distance were also spatially averaged through a horizontal xy plane. This is equivalent to the averaging of the velocity profile from all available vertical line in the computational domain. The mean velocity profile is presented for the Stokes case (longitudinal and spanwise cylinders) in figure 4.1.4 in terms of global coordinate in which the normal distance y is normalised with H, while the mean streamwise velocity is normalised with $\overline{U}_{avg}$. As a reference, the smooth channel case and results from Chu et al. 2021 are reported as well. In fig. 4.1.5, the mean velocity for the Oseen case is present, in terms of global coordinates in which the normal distance y_{center} is measured from the center of the channel and normalised with H ($y_{center}/H = 1$ for the upper wall, $y_{center}/H = -1$ for the lower wall), while the mean velocity is normalised with $U_{bulk} = \overline{U}_{avg}$. Note that, in the smooth case, mean velocity equals to zero at both walls, while in the porous case it is different from zero at the lower wall, consistently with our boundary conditions. Moreover, in the smooth case, the velocity profile is

symmetric with respect to the center of the channel, while in the porous case it is distorted, with a higher mean velocity in the upper region.
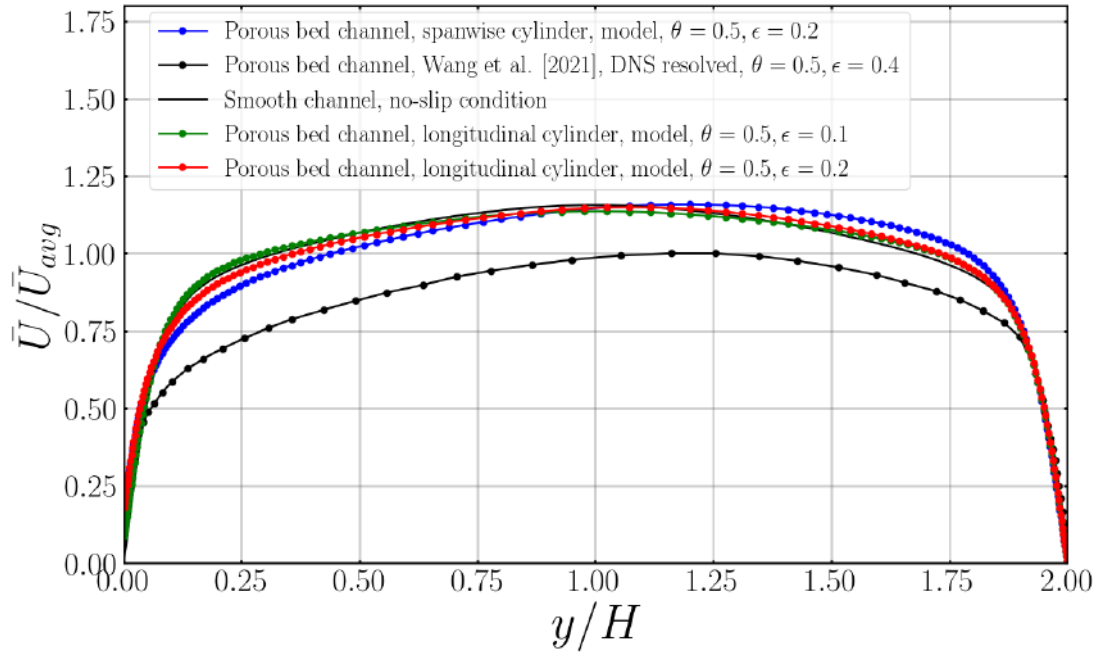
Figure 4.1.4: Mean velocity profile for longitudinal and spanwise inclusions (DNS performed with Stokes' coefficients), compared with the smooth walls one. As a reference, also the case for $\epsilon = 0.4$ by Chu et al. 2021 is reported.
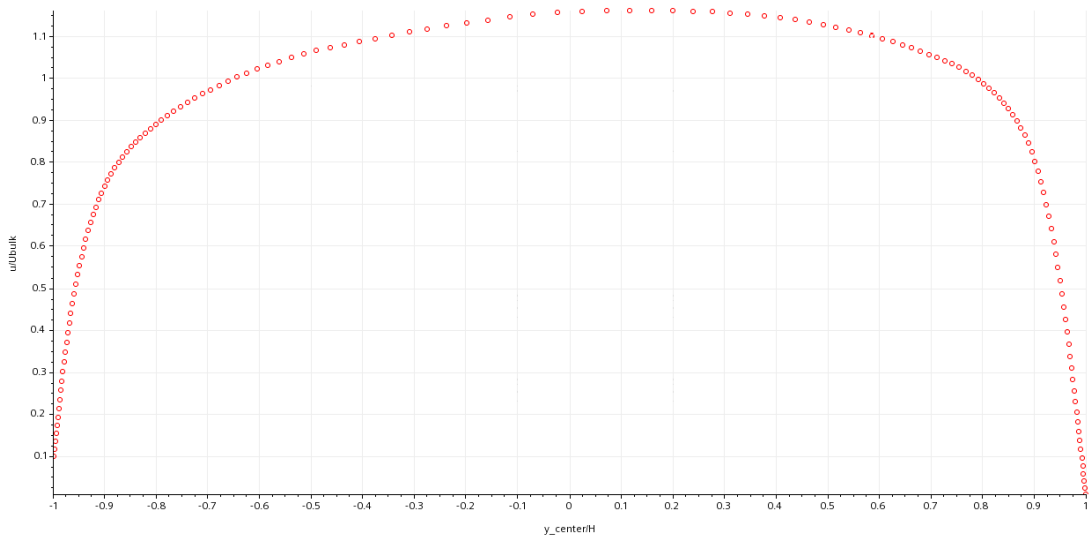
Figure 4.1.5: Mean velocity profile for spanwise inclusions (DNS performed with Oseen's coefficients).

Velocity profile against wall coordinates It is better to plot the mean velocity against the wall coordinates, i.e. the behaviour of u^+ vs y^+ (fig. 4.1.6, 4.1.7). In addition, this description provides a better understanding of the simulation accuracy based on the classification of flow regions. We see that the smooth wall case correctly reproduces the expected behaviour, based on the general Spalding's law. For spanwise cylinders, we find drag-increasing, while with streamwise ones we are able to find also drag-reduction (as we will see). We are going to compare our (spanwise) results with fully-feature DNS by Chu et al. 2021 (fig. 4.1.8), being their case for spanwise cylinders with $\theta = 0.5$, $\epsilon = 0.4$, $Re_\tau = 279$ (with our definition) and $Re = 3680$ (based on H and on U_{bulk}). However, we have $\epsilon = 0.2$ and $Re_\tau = 193$. This difference makes a quantitative comparison not possible, leaving us with only the possibility of a qualitative one. For spanwise cylinders, results from Stokes' coefficients are quite similar, while Oseen's coefficients slightly improve results in the viscous sub-layer but degrade them in the log-law region. This difference may be due to the difference in Re_τ, since, while for the Stokes' case its value does not matter much, as long as it is above 170 (about), for larger Re_τ the only difference is felt in the extent of the log region, exactly where we have a discrepancy with Oseen's coefficients, which themselves depend on Re_τ. Finally, we have to stress out that the difference in ϵ is the main difficult to overcame in order to compare our results with this fully-feature DNS. The point is that $\epsilon = 0.4$ in our macroscopic case is really too large in order to get convergent results (there is too much transpiration through the virtual wall). This is why we tried to reproduce literature results with $\epsilon = 0.2$, which is not so small but neither too large. This difference is felt more in the Oseen case (which in principle should improve Stokes' results) because Oseen's coefficients themselves depend also on ϵ, as they depend on ϵRe_τ: in our case, we used $\epsilon Re_\tau = 0.2 \cdot 193 \approx 40 = \mathcal{O}(10)$, while in the fully-feature DNS it is $\epsilon Re_\tau = 0.4 \cdot 280 \approx 112 = \mathcal{O}(10^2)$. We remember that in principle our Oseen approximation should rely on the fact that $\epsilon \ll 1$ and $\epsilon Re_\tau = \mathcal{O}(1)$. We know that as a matter of fact we can go beyond the formal limit of the theory, but the fully-feature DNS would require going two order of magnitude above the limit, not only one as we did. In the end, this qualitative comparison gives us the idea that our solutions present a reasonable trend. However, we must suspend the judgment about a possible close quantitative agreement with the exact result, and also about a possible improvement of the Oseen's coefficients. At the same time, the fact that the ($\epsilon Re_\tau \approx 40$)-Oseen's DNS presents a less agreement with the ($\epsilon Re_\tau \approx 112$)-fully-feature DNS with respect to the ($\epsilon Re_\tau \approx 40$)-Stoke's DNS makes us confident that Oseen's coefficients can correctly reproduce the true case for which they have been calculated.
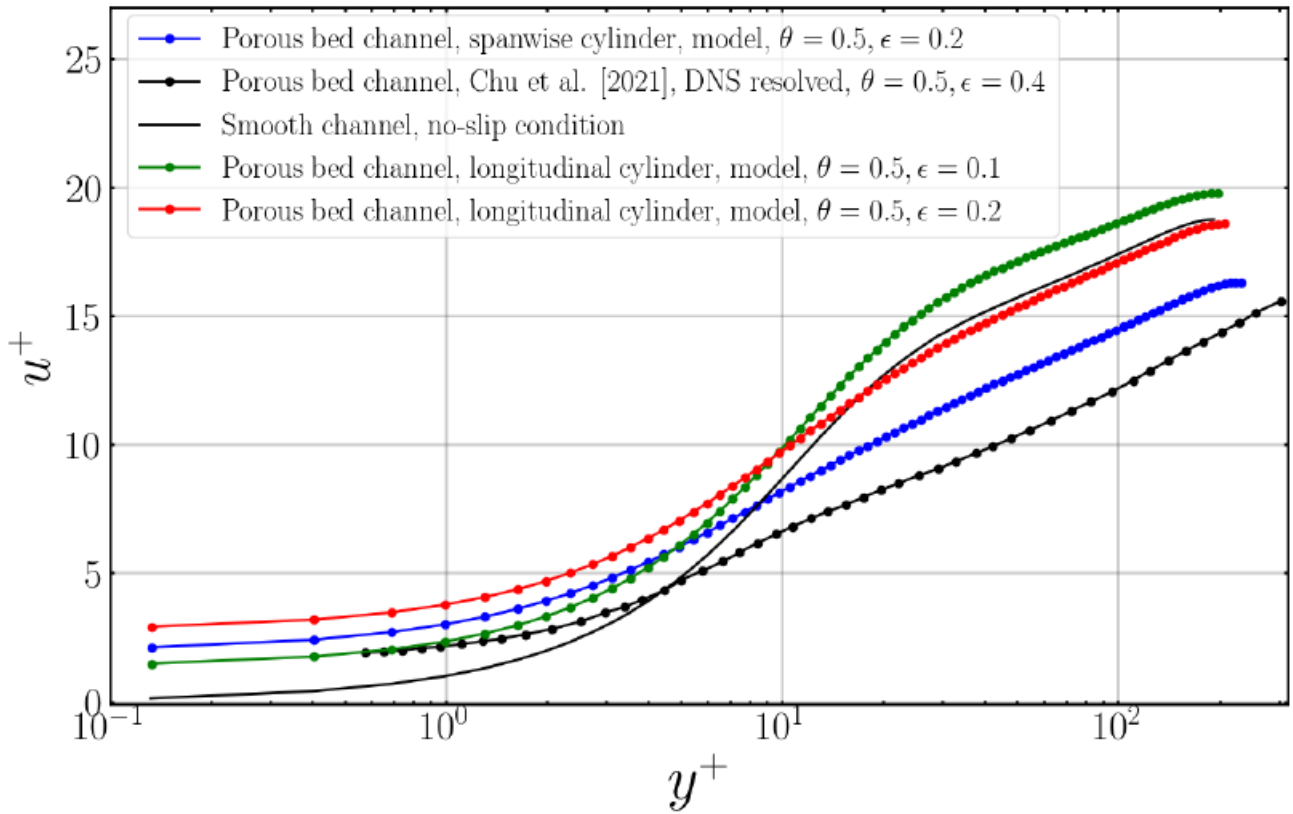
Figure 4.1.6: Velocity profile against wall coordinate, for varying cases compared to the smooth channel case (DNS performed with Stokes' coefficients). Results from Chu et al. 2021 are reported as well.
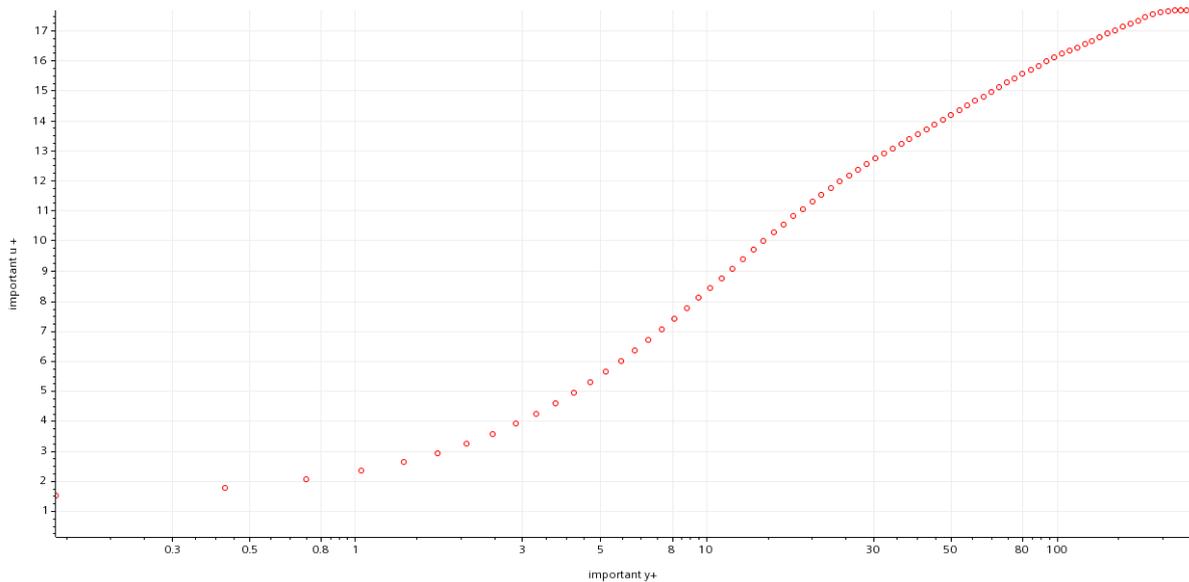
Figure 4.1.7: Velocity profile against wall coordinate, for spanwise inclusions (DNS performed with Oseen's coefficients).
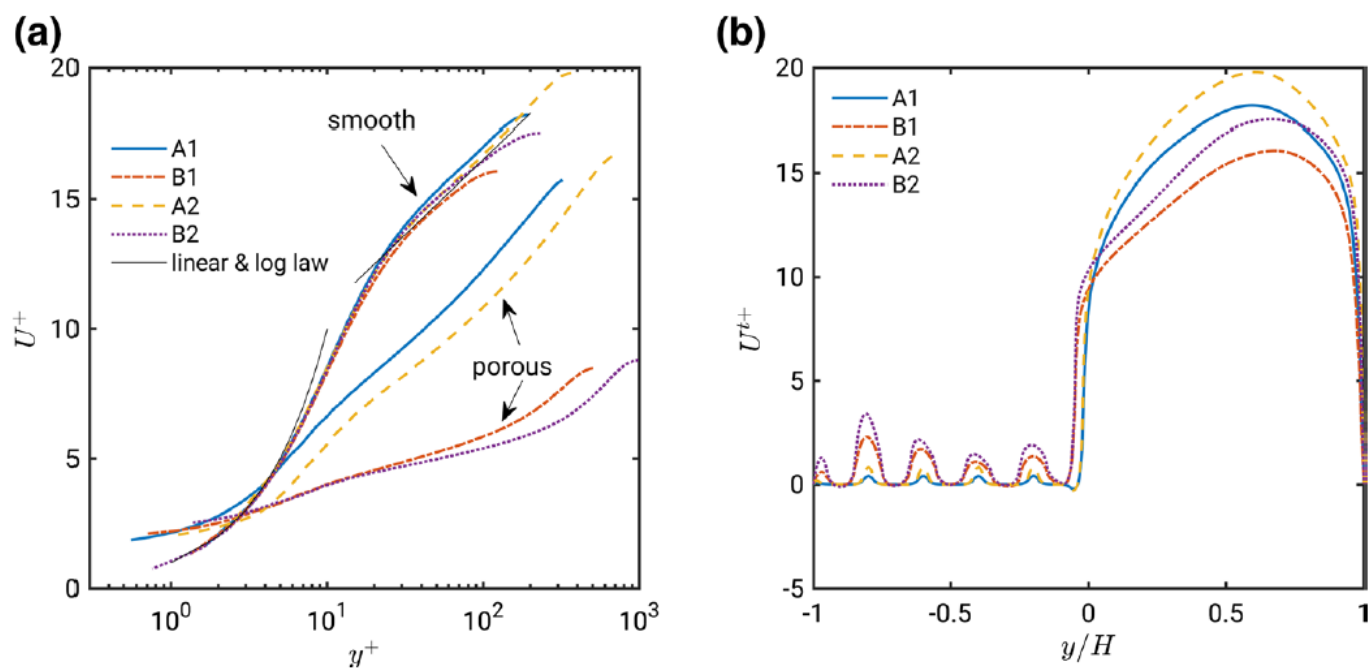
Figure 4.1.8: Results from fully-feature DNS made by Chu et al. 2021 (case A1). (a): Velocity profile against wall coordinate. (b): Mean velocity profile.

RMS of the velocity fluctuations We decompose the instantaneous velocity u_i into the sum of the mean velocity $\bar{u}_i$ and a time-fluctuating field u_i', as

$$u_i = \bar{u}_i + u_i' \qquad (4.1.3)$$

Then, we consider its RMS value as a measure of the strength of the fluctuations:

$$u_{i,\mathrm{rms}} = \sqrt{\overline{u_i'^2}} \qquad (4.1.4)$$

without summing on i. Again, these results were collected against y/H from all available vertical lines and averaged to perform the pattern of the rms fluctuation vs the wall normal distance. Now we clearly see (fig. 4.1.9) that the fluctuations in the streamwise velocity is the strongest, then comes the spanwise one and, finally, the normal velocity fluctuations are the weakest. Furthermore, the spanwise cylinders enhance turbulent fluctuations (v_{rms} and w_{rms}) as compared to the smooth wall case, and damper the intensity of the streaks (u_{rms}). It's reasonable to find that both spanwise and normal velocity components are fluctuating around zero, because the mean flow is driven only in the streamwise direction. The strongest fluctuations take place in the buffer layer, while in the viscous sub-layer they are weak.

Reynolds stresses We now concentrate on the description of the behaviour of the viscous and the Reynolds stresses, specially the xy component across the channel. This will give the total shear stress on the permeable wall, τ_w, which is related to the total friction:

$$\tau_w = \tau_{xy}^v + \tau_{xy}^R \qquad (4.1.5)$$

where $\tau_{xy}^v = \mu\left(\frac{\partial \bar{u}}{\partial y} + \frac{\partial \bar{v}}{\partial x}\right)$ is the viscous stress xy component (taking into account that here $\bar{v} = 0$) and $\tau_{12}^R = -\rho\overline{u'v'}$ is the Reynolds stress xy component. Since we find $\tau_{xy}^R > 0$, it actually increases the total stress at the low wall. Finally, the stresses are normalised with the scale ρu_τ^2. The behavior of the DNS results of the Reynolds and stresses (modulus a $-$ sign) against y/H is presented in figure 4.1.10. For spanwise cylinders, the stress at the low wall is in absolute value quite higher than in the smooth channel case.
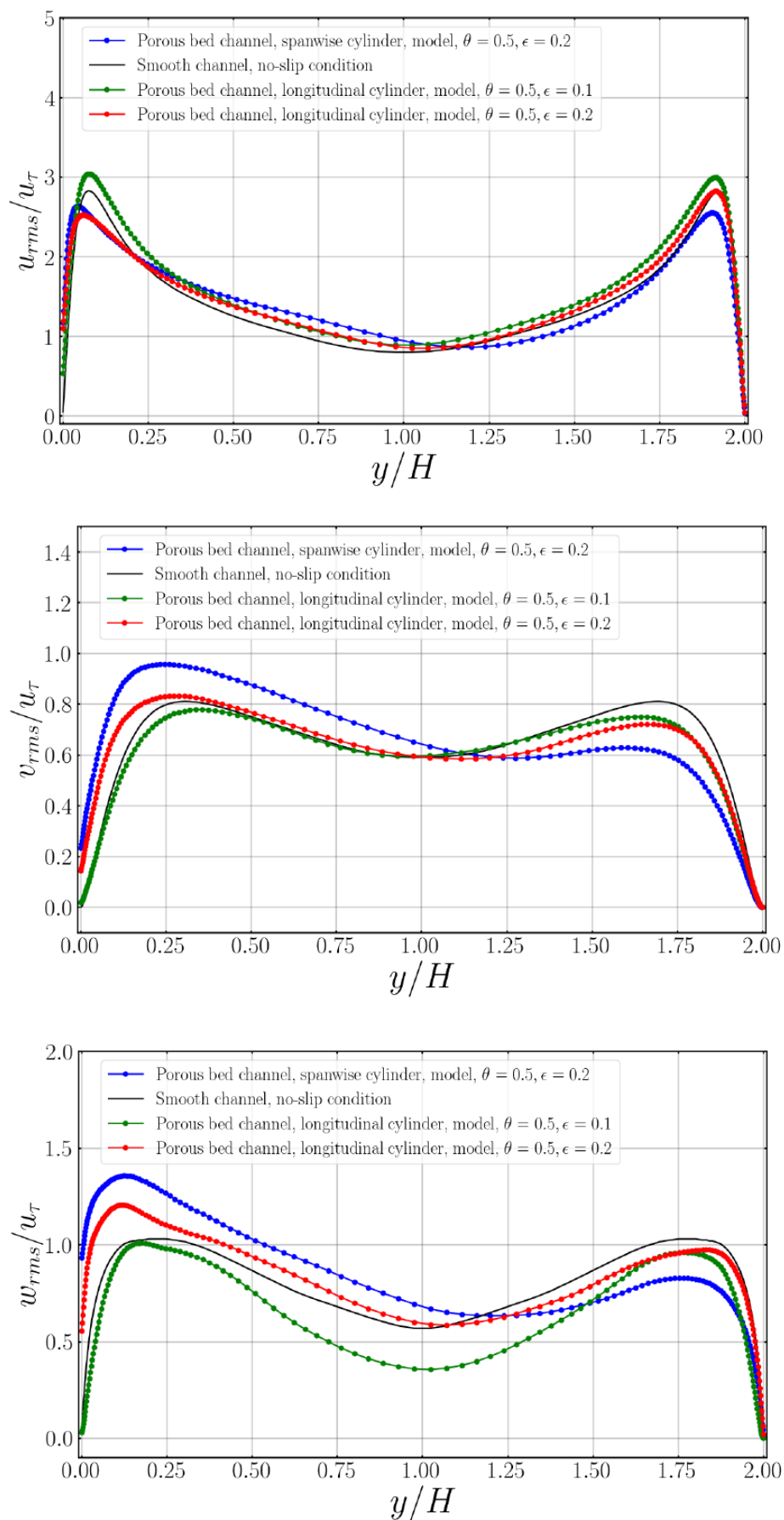
Figure 4.1.9: RMS of the velocity fluctuations (DNS performed with Stokes' coefficients).
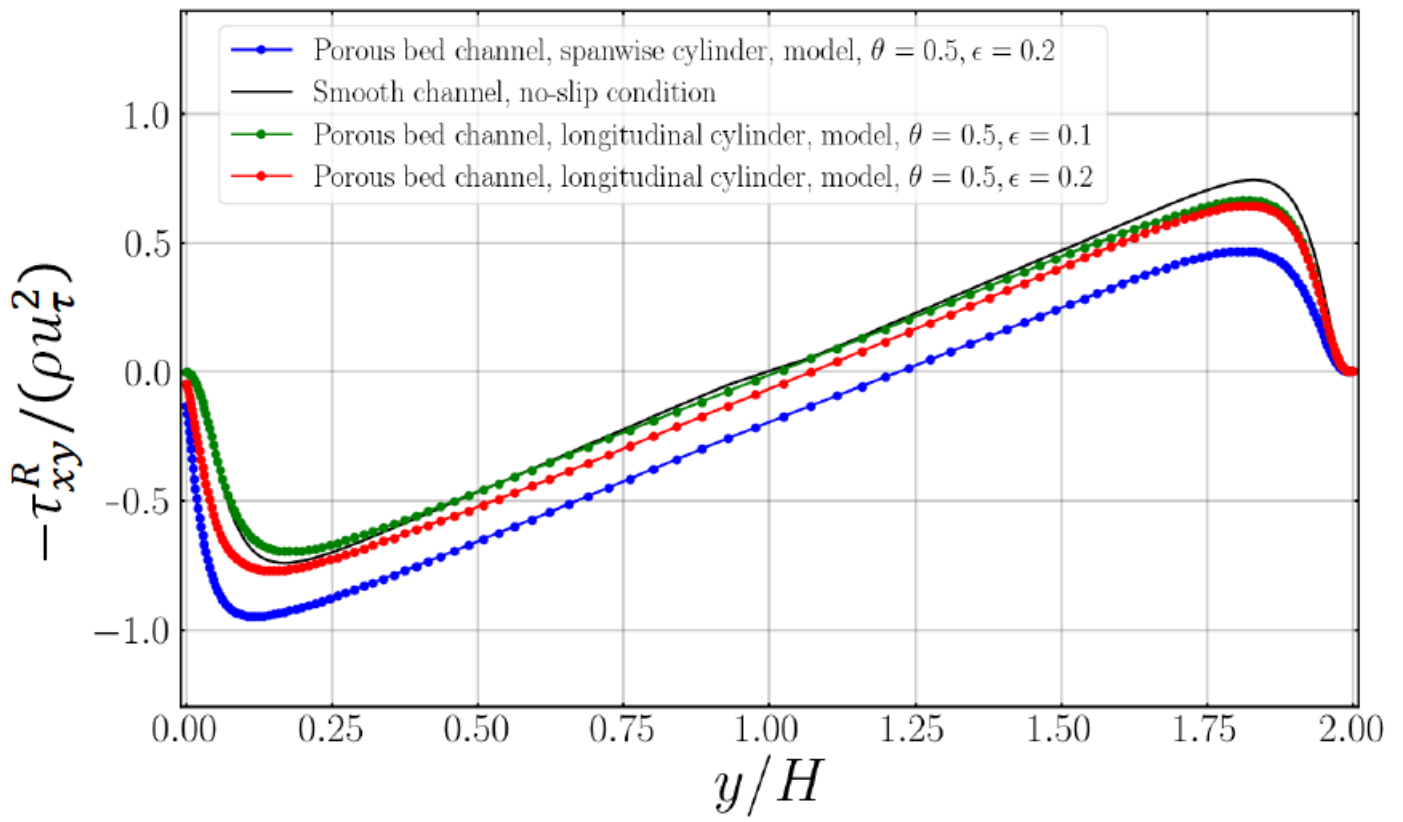
Figure 4.1.10: Reynolds stress $-\tau_{xy}^R$ (DNS performed with Stokes' coefficients).

4.2 Streamwise inclusions: Drag reduction

This time, we switch the direction of the cylindrical inclusions of the (inferior) permeable wall from spanwise to streamwise. We remember that, in this case, Oseen's coefficients coincide with Stokes' ones, which have been widely tested and validated in the past (Naqvi and Bottaro 2021), nor they present a dependence from Re_τ or ϵ (provided ϵ is still small and, ideally, ϵRe_τ of order 1). For this reason, we are going to use our own homogenised development, despite the previous ineffective validation.

In this configuration, we hope to find drag-reduction with respect to the smooth wall case. We are trying our inspiration from the riblets case, as widely illustrated in previous chapters. Again, we choose $\theta = 0.5$ and $Re_\tau = 193$ at the inferior wall. However, this time we vary $\epsilon \in [0, 0.2]$ ($\epsilon = 0, 0.1, 0.2$ so far) in order to reconstruct the drag curve, thus doing several DNSs. Indeed, we believe that here ϵ (or ϵRe_τ) plays the same role of the (dimensionless) riblets spacing $s^+ = \frac{su_\tau}{\nu}$ in the case of riblets. This is because, if we try to divide s^+ by $Re_\tau = \frac{u_\tau H}{\nu}$, we find $\frac{s^+}{Re_\tau} = \frac{s}{H}$. Hence, if we remember the definition of ϵ as $\epsilon = \frac{l}{L}$, where l is a characteristic microscopic length and L a macroscopic one, by choosing $l = s$, the inter-pore distance (analog to the riblets spacing), and $L = H$ the half-channel height (as previously done), we are left with

$$\epsilon = \frac{s^+}{Re_\tau} \tag{4.2.1}$$

Since s^+ is a parameters that controls the drag-curve in the case of riblets, we hope we can do the same here with ϵ (or ϵRe_τ), which is here proportional to the analogue of s^+.

Considering that from literature we know that there is drag reduction for approximately $s^+ \in [0, 30]$ (and that there is drag-increase for higher values), reaching its optimum for $s^+ \approx 20$, we expect to find drag-reduction for $\epsilon \in [0, 0.2]$ with optimum drag-reduction for $\epsilon \approx 0.1$, being $Re_\tau = 193$ fixed.

Obviously, also this time we substitute the inferior rough, permeable wall with a smooth wall positioned at the same height, at which we apply our effective boundary condition 3.2.26, 3.2.27, 3.2.28. As far as microscopic coefficients are concerned, we will use a unique set of (dimensionless) coefficients, reported in table 4.3. Moreover, dimensional coefficients are reported in table 4.4.

Geometry and Setup   The geometry and setup are identical to the ones of the spanwise simulations, apart that now the flow is driven not by an external forcing but by an imposed constant pressure gradient, which acts as a source

λ_x	λ_z	$\mathcal{K}_{yy}$	$\mathcal{K}_{xy}^{itf}$	$\mathcal{K}_{zy}^{itf}$
6.901E − 02	4.521E − 02	1.871E − 03	5.588E − 03	2.226E − 03

$$(4.2.2)$$

Table 4.3: This table shows the numerical values of the (dimensionless) parameters of the effective boundary conditions applied at the lower wall in the DNS. The case is of longitudinal cylindrical inclusions, with $\theta = 0.5$.

ϵ	$\hat{\lambda}_x\ (m)$	$\hat{\lambda}_z\ (m)$	$\hat{\mathcal{K}}_{yy}\ (m^2)$	$\hat{\mathcal{K}}_{xy}^{itf}\ (m^2)$	$\hat{\mathcal{K}}_{zy}^{itf}\ (m^2)$
0.2	1.380E − 02	9.042E − 03	7.484E − 05	2.235E − 04	8.902E − 05
0.1	6.901E − 03	4.521E − 03	1.871E − 05	5.588E − 05	2.226E − 05

$$(4.2.3)$$

Table 4.4: This table shows the numerical values of the (dimensional, via 3.2.29) parameters of the effective boundary conditions applied at the lower wall in the DNS. The case is of longitudinal cylindrical inclusions, with $\theta = 0.5$. We considered several values of ϵ.

term. Hence, we can say that

$$\tau_w = \frac{\Delta p}{L} H \qquad (4.2.4)$$

where L is a length measured in the streamwise direction (say the global streamwise length of the domain) and Δp is the pressure difference between inlet and outlet when the fluid travels this streamwise distance. Since we set $H = 1\,m$ and would like $\tau_w = 1\,Pa$, we choose the ratio $\frac{\Delta p}{L}$ to be $\frac{\Delta p}{L} = 1\,N/m^3$. Thus, we are in the same numerical situation of the previous simulations.

Turbulent statistics and main monitored parameters Statistics include the same calculation of the previous case plus the flow rate, i.e.

- mean velocity by time-averaging

- velocity fluctuations to get the RMS values

- mean values of the Reynolds stresses

- flow rate, in order to reconstruct the drag curve

The main monitored parameter was Re_τ on the lower wall also this time. Moreover, we monitored instantaneous streamwise and wall normal velocities at $y^+ = 20$ (buffer layer) for spanwise cylinders with $\epsilon = 0.2$ and for streamwise cylinders with $\epsilon = 0.1$ (fig. 4.2.1). We find that for streamwise cylinders ($\epsilon = 0.1$) the flow seems on the way to become laminar again, while for spanwise cylinders ($\epsilon = 0.2$) it seems more chaotic.

Spanwise arranged cylinder, $\epsilon = 0.2$ Streamwise arranged cylinder, $\epsilon = 0.1$
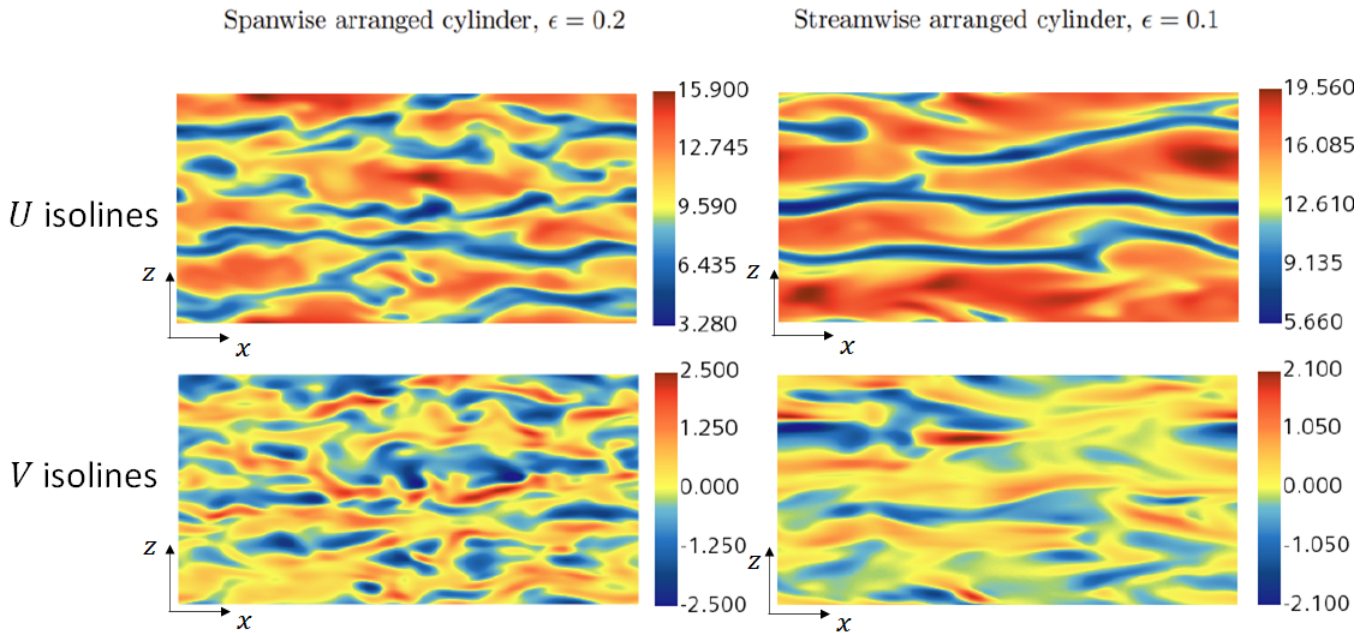
Figure 4.2.1: Isolines of U and V at $y^+ = 20$ for $\epsilon = 0.1, 0.2$ in a plane parallel to the inferior wall (DNS performed with Stokes' coefficients). Velocity numerical values are intended as expressed in ms^{-1}.

Mean Velocity profile The same previous procedure to get the mean velocity profile is performed. Result is presented in figure 4.1.4, with the same previous notation. Also this time, we can note that we have a non zero velocity at the lower wall in the porous case. However, apart from this, this time the profile is less altered with respect to the smooth case, with much less asymmetry (though still present) than in the spanwise case.

Velocity profile against wall coordinates With reference to fig. 4.1.6, we notice that in this case with streamwise cylinders the shape of the velocity is more similar to the smooth wall case than with spanwise cylinders. Furthermore, by looking at the log-law region, we clearly see that there is drag-reduction for $\epsilon = 0.1$ and a slight drag-increase for $\epsilon = 0.2$, confirming our intuitions.

RMS of the velocity fluctuations In fig. 4.1.9, RMS of the velocity fluctuations is presented also for this streamwise case. Similar consideration about the general amplitude of the fluctuations can be made. Moreover, we observe that for the drag-reducing case streamwise fluctuation is higher while normal and spanwise ones are lower with respect to the smooth case, while for the drag-increasing case the *viceversa* is true.

Reynolds stresses In fig. 4.1.10, xy-Reynolds stress is presented. This time, the deviation from smooth channel is less than for spanwise cylinders, with the drag-reducing case very close to it, although difference at the lower

wall is still present (here not distinguishable for the drag-reducing case), thus increasing the total stress at it.

Drag curve Finally, we are able to reconstruct the drag curve (fig. 4.2.2). We should mention that with only the points for $\epsilon = 0, 0.1, 0.2$ we can only give a basic idea of the phenomenon, having in mind to thicken the graph with more simulations. However, we find very interesting results: for $\epsilon = 0.2$ we are about the turning point from drag-reduction to drag-increase, while for $\epsilon = 0.1$ we find drag reduction and have just passed the corresponding ϵ value for drag-optimum point (by interpolating the data, we guess $\epsilon_{\mathrm{opt}} \approx 0.08$). Obviously, in the limit of $\epsilon \to 0$ we recover smooth wall's results. Hence, data are graphically compatible with a drag-curve similar to the riblet's one, with a linear relationship for $\epsilon \in [0, 0.1]$ to be investigated. This confirms our intuitions: cylindrical streamwise-directed porous inclusions behave like riblets as far as drag reduction is concerned, with the ϵ (or ϵRe_τ) parameter playing the same role of the (dimensionless) riblets' spacing s^+. This enables us to quickly implement a surface with the desired drag-reducing or drag-increasing factor, just by playing with geometrical and dynamical quantities in the proper way.
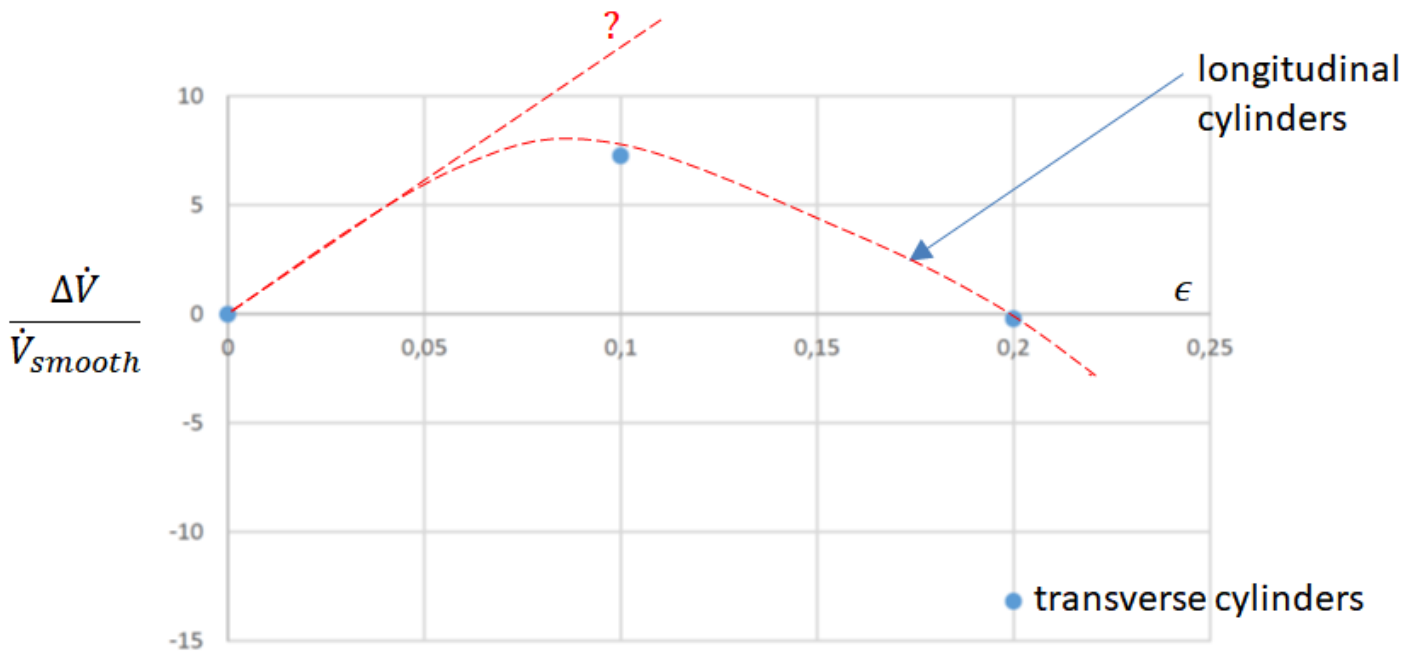
Figure 4.2.2: Drag curve for longitudinal cylinders against ϵ. The point for spanwise cylinders at $\epsilon = 0.2$ is reported as well ((DNS performed with Stokes' coefficients)). The red dashed lines are drawn only to guide the eye.

Conclusion

In the present work, we have used homogenisation theory to study the inter-action between a fluid and a porous medium. Thanks to this technique, we have been able to model the interaction via effective coefficients directly avail-able from the solution of microscopic problems, so that one does not need to set them *ad hoc*. This is an important result, since one is allowed to substi-tute the permeable surface with a smooth one, provided that our effective boundary conditions are applied, thus saving computational time. In this way, one may study more complicated cases, for which a fully-feature DNS is prohibitive or not desired. Hence, homogenisation theory (and, as a con-sequence, our effective boundary condition) is a powerful tool to treat such cases. Moreover, we tried to extend previous works by taking turbulence into account (as well as a 3D description) already at microscopic level, going be-yond the lower transitionally rough regime, via an Oseen approximation.

In 3, we calculated microscopic coefficients for a variety of cases, so that they are already available for any future work of anybody. We remark we also gave a little contribution from this point of view by proposing a fit law for micro-scopic Stokes's parameters against porosity.

In 4, in order to validate our conditions, we studied a macroscopic case (a fully developed turbulent channel flow with one permeable wall of spanwise inclusions) and compared our solutions with a recent fully-feature resolving DNS present in literature. However, we found that, in this reference, impor-tant geometrical and dynamical parameters had different numerical values with respect to the ones we prepared our computations. This fact makes a quantitative comparison ineffective, though allowing a qualitative one, which indeed was quite satisfactory. Given the above mentioned diversity of pa-rameters (in particular, ϵRe_τ), the (apparently unwanted) fact that the DNS with Stokes' coefficients, unlike the one with Oseen coefficients (which de-pend themselves on ϵRe_τ), seems to be in good agreement with the literature one makes us at least hopeful about a possible improvement by Oseen coef-ficients, since they could lead to a better agreement with respect to the real case they were constructed for. More work is need about this point: a fully-feature DNS (with the correct corresponding parameters) is actually under construction.

Furthermore, despite the ineffective validation test, we decided to use our effective conditions to independently study another macroscopic case, very similar to the previous one. This is because, in this case, we used, *de facto*, only Stokes' coefficients, which had already been widely tested (and validated) in the past. Hence, as a result, we found that, by taking longitudinal porous inclusions (we remember that in this case Oseen and Stokes' coefficients coincide), there is a drag-reduction modulated by the ϵ parameter. Hence, we were able to propose a theoretical porous surface with drag-reducing property, characterise the drag curve and find values for optimum drag-reduction, which is a highly desirable property in many industrial contexts.

Our construction may allow the rapid modeling of geometrical micro-features, to identify, e.g., the most efficient drag-reducing textures, or the most suitable structure of a porous membrane, and so on.

Possible future developments may include the following: consider a lubricant fluid within the pores, solving the problem via the VOF (volume of fluid) method in the unit cell; derive effective slip and transpiration conditions to second order in this two-phase flow case (already derived at first order by Alinovi and Bottaro 2018); perform an effective DNS for a turbulent channel flow over a LIS (lubricant impregnated surface) and compare to fully-feature resolving DNS; optimise the morphology of the porous material, impregnated with lubricant, and optimise property of lubricant fluid.

In the end, we proposed an alternative way to study and characterise the interaction of a fluid with rough (permeable) surfaces, which are the norm, not the exception, of many natural and biological systems, whose properties are sources of inspiration for many useful applications, as seen in 1.

Appendix: Tables of Microscopic Coefficients

θ	λ_x	λ_z	$\mathcal{K}_{xx} \approx \mathcal{K}_{yy}$	$\mathcal{K}_{zz}$	$\mathcal{K}_{xy}^{itf}$	$\mathcal{K}_{zy}^{itf}$
0.215	$4.103\mathrm{E}-02$	$5.883\mathrm{E}-02$	0	$1.217\mathrm{E}-03$	$1.823\mathrm{E}-03$	$3.814\mathrm{E}-03$
0.5000	$4.513\mathrm{E}-02$	$6.883\mathrm{E}-02$	$1.828\mathrm{E}-03$	$6.966\mathrm{E}-03$	$2.220\mathrm{E}-03$	$5.561\mathrm{E}-03$
0.600	$4.713\mathrm{E}-02$	$7.398\mathrm{E}-02$	$4.331\mathrm{E}-03$	$1.212\mathrm{E}-02$	$2.410\mathrm{E}-03$	$6.737\mathrm{E}-03$
0.7000	$4.992\mathrm{E}-02$	$8.167\mathrm{E}-02$	$9.587\mathrm{E}-03$	$2.222\mathrm{E}-02$	$2.657\mathrm{E}-03$	$9.042\mathrm{E}-03$
0.800	$5.385\mathrm{E}-02$	$9.347\mathrm{E}-02$	$1.990\mathrm{E}-02$	$4.179\mathrm{E}-02$	$2.965\mathrm{E}-03$	$1.410\mathrm{E}-02$
0.8500		$1.008\mathrm{E}-01$				$1.820\mathrm{E}-02$
0.9000	$6.010\mathrm{E}-02$	$1.130\mathrm{E}-01$	$3.970\mathrm{E}-02$	$8.031\mathrm{E}-02$	$4.113\mathrm{E}-03$	$2.638\mathrm{E}-02$
0.950		$1.339\mathrm{E}-01$				$4.386\mathrm{E}-02$
0.99000	$8.912\mathrm{E}-02$	$1.953\mathrm{E}-01$	$1.255\mathrm{E}-01$	$2.534\mathrm{E}-01$	$2.960\mathrm{E}-02$	$1.075\mathrm{E}-01$

$$(4.2.5)$$

Table 4.5: This table shows the numerical values of the parameters of interest against different values of porosity, for $Re_\tau = 0$ (*inline* configuration and *spanwise* inclusions). Data are plotted in 3.4.6.

θ	λ_x	λ_z	$\mathcal{K}_{yy}$	$\mathcal{K}_{zz}$	$\mathcal{K}_{xy}^{itf}$	$\mathcal{K}_{zy}^{itf}$
0.215	$4.759\mathrm{E}-02$	$7.677\mathrm{E}-02$	0	$5.056\mathrm{E}-04$	$2.469\mathrm{E}-03$	$7.871\mathrm{E}-03$
0.500	$5.168\mathrm{E}-02$	$8.677\mathrm{E}-02$	$1.008\mathrm{E}-03$	$3.693\mathrm{E}-03$	$2.866\mathrm{E}-03$	$9.618\mathrm{E}-03$
0.600	$5.378\mathrm{E}-02$	$9.305\mathrm{E}-02$	$2.435\mathrm{E}-03$	$6.591\mathrm{E}-03$	$3.160\mathrm{E}-03$	$1.169\mathrm{E}-02$
0.700	$5.618\mathrm{E}-02$	$1.003\mathrm{E}-01$	$4.314\mathrm{E}-03$	$1.128\mathrm{E}-02$	$3.618\mathrm{E}-03$	$1.457\mathrm{E}-02$
0.800	$5.998\mathrm{E}-02$	$1.122\mathrm{E}-01$	$7.358\mathrm{E}-03$	$2.180\mathrm{E}-02$	$4.699\mathrm{E}-03$	$2.051\mathrm{E}-02$
0.850		$1.233\mathrm{E}-01$	$1.050\mathrm{E}-02$	$3.392\mathrm{E}-02$		$2.740\mathrm{E}-02$
0.900	$6.656\mathrm{E}-02$	$1.323\mathrm{E}-01$	$1.342\mathrm{E}-02$	$4.448\mathrm{E}-02$	$7.806\mathrm{E}-03$	$3.376\mathrm{E}-02$
0.95000		$1.585\mathrm{E}-01$				$5.380\mathrm{E}-02$
0.99000	$1.010\mathrm{E}-01$	$2.173\mathrm{E}-01$	$4.897\mathrm{E}-02$	$1.382\mathrm{E}-01$	$3.712\mathrm{E}-02$	$1.056\mathrm{E}-01$

$$(4.2.6)$$

Table 4.6: This table shows the numerical values of the parameters of interest against different values of porosity, for $Re_\tau = 0$ (*staggered* configuration and *spanwise* inclusions). Data are plotted in 3.4.6.

ϵRe_τ	Re_τ	λ_x	λ_z	$\mathcal{K}_{yy}$	$\mathcal{K}_{xy}^{itf}$	$\mathcal{K}_{zy}^{itf}$
0	0	$4.513\mathrm{E}-02$	$6.883\mathrm{E}-02$	$1.828\mathrm{E}-03$	$2.220\mathrm{E}-03$	$5.561\mathrm{E}-03$
12	60	$4.170\mathrm{E}-02$	$6.124\mathrm{E}-02$	$1.533\mathrm{E}-03$	$1.887\mathrm{E}-03$	$4.507\mathrm{E}-03$
24	120	$3.815\mathrm{E}-02$	$5.365\mathrm{E}-02$	$1.262\mathrm{E}-03$	$1.556\mathrm{E}-03$	$3.462\mathrm{E}-03$
36	180	$3.562\mathrm{E}-02$	$4.859\mathrm{E}-02$	$9.859\mathrm{E}-04$	$1.336\mathrm{E}-03$	$2.819\mathrm{E}-03$
39	193	$3.514\mathrm{E}-02$	$4.768\mathrm{E}-02$	$9.431\mathrm{E}-04$	$1.296\mathrm{E}-03$	$2.707\mathrm{E}-03$
44	222	$3.419\mathrm{E}-02$	$4.591\mathrm{E}-02$	$8.474\mathrm{E}-04$	$1.222\mathrm{E}-03$	$2.506\mathrm{E}-03$
53	264	$3.301\mathrm{E}-02$	$4.374\mathrm{E}-02$	$7.407\mathrm{E}-04$	$1.130\mathrm{E}-03$	$2.263\mathrm{E}-03$
61	306	$3.202\mathrm{E}-02$	$4.195\mathrm{E}-02$	$6.605\mathrm{E}-04$	$1.054\mathrm{E}-03$	$2.071\mathrm{E}-03$
70	348	$3.110\mathrm{E}-02$	$4.037\mathrm{E}-02$	$5.928\mathrm{E}-04$	$9.890\mathrm{E}-04$	$1.911\mathrm{E}-03$
78	390	$3.028\mathrm{E}-02$	$3.898\mathrm{E}-02$	$5.375\mathrm{E}-04$	$9.333\mathrm{E}-04$	$1.776\mathrm{E}-03$

$$(4.2.7)$$

Table 4.7: This table shows the numerical values of the parameters of interest against different values of Re_τ, having fixed $\theta = 0.5$ and $\epsilon = 0.2$, for *inline* pattern and *spanwise* inclusions. Data are plotted in 3.2.6.

θ	λ_x	$\mathcal{K}_{xy}^{itf}$	λ_z	$\mathcal{K}_{zy}^{itf}$	$\mathcal{K}_{yy}$
0.215	$3.264\mathrm{E}-02$	$1.139\mathrm{E}-03$	$4.311\mathrm{E}-02$	$2.153\mathrm{E}-03$	0
0.5	$3.514\mathrm{E}-02$	$1.296\mathrm{E}-03$	$4.768\mathrm{E}-02$	$2.707\mathrm{E}-03$	$9.431\mathrm{E}-04$
0.8	$4.060\mathrm{E}-02$	$1.514\mathrm{E}-03$	$5.719\mathrm{E}-02$	$4.064\mathrm{E}-03$	$5.232\mathrm{E}-03$
0.9	$4.413\mathrm{E}-02$	$2.282\mathrm{E}-03$	$6.385\mathrm{E}-02$	$5.579\mathrm{E}-03$	$9.572\mathrm{E}-03$
0.99	$5.788\mathrm{E}-02$	$1.165\mathrm{E}-02$	$9.177\mathrm{E}-02$	$3.028\mathrm{E}-02$	$3.373\mathrm{E}-02$

$$(4.2.8)$$

Table 4.8: This table shows the numerical values of the parameters of interest against different values of θ, having fixed $Re_\tau = 193$ and $\epsilon = 0.2$ (*inline* configuration and *spanwise* inclusions). Data are plotted in 3.2.7.

θ	λ_x	$\mathcal{K}_{xy}^{itf}$	λ_z	$\mathcal{K}_{zy}^{itf}$	$\mathcal{K}_{yy}$
0.215	$2.832\mathrm{E}-02$	$8.416\mathrm{E}-04$	$3.580\mathrm{E}-02$	$1.480\mathrm{E}-03$	0
0.5	$3.028\mathrm{E}-02$	$9.333\mathrm{E}-04$	$3.898\mathrm{E}-02$	$1.776\mathrm{E}-03$	$5.375\mathrm{E}-04$
0.8	$3.442\mathrm{E}-02$	$1.071\mathrm{E}-03$	$4.533\mathrm{E}-02$	$2.421\mathrm{E}-03$	$2.784\mathrm{E}-03$
0.9	$3.721\mathrm{E}-02$	$1.392\mathrm{E}-03$	$4.977\mathrm{E}-02$	$2.973\mathrm{E}-03$	$5.078\mathrm{E}-03$
0.99	$4.590\mathrm{E}-02$	$5.925\mathrm{E}-03$	$6.608\mathrm{E}-02$	$1.554\mathrm{E}-02$	$1.880\mathrm{E}-02$

$$(4.2.9)$$

Table 4.9: This table shows the numerical values of the parameters of interest against different values of θ, having fixed $Re_\tau = 390$ and $\epsilon = 0.2$ (*inline* configuration and *spanwise* inclusions). Data are plotted in 3.2.7.

ϵRe_τ	Re_τ	λ_x	$\mathcal{K}_{xy}^{itf}$	λ_z	$\mathcal{K}_{zy}^{itf}$	$\mathcal{K}_{yy}$
0	0	$4.104\mathrm{E}-02$	$1.823\mathrm{E}-03$	$5.883\mathrm{E}-02$	$3.814\mathrm{E}-03$	0
39	193	$3.264\mathrm{E}-02$	$1.139\mathrm{E}-03$	$4.311\mathrm{E}-02$	$2.153\mathrm{E}-03$	0
78	390	$2.832\mathrm{E}-02$	$8.416\mathrm{E}-04$	$3.580\mathrm{E}-02$	$1.480\mathrm{E}-03$	0

$$(4.2.10)$$

Table 4.10: This table shows the numerical values of the parameters of interest against different values of Re_τ, having fixed $\theta = 0.215$ and $\epsilon = 0.2$ (*inline* configuration and *spanwise* inclusions). Data are plotted in 3.2.11.

ϵRe_τ	Re_τ	λ_x	$\mathcal{K}_{xy}^{itf}$	λ_z	$\mathcal{K}_{zy}^{itf}$	$\mathcal{K}_{yy}$
0	0	$5.385\mathrm{E}-02$	$2.965\mathrm{E}-03$	$9.347\mathrm{E}-02$	$1.410\mathrm{E}-02$	$1.990\mathrm{E}-02$
39	193	$4.060\mathrm{E}-02$	$1.514\mathrm{E}-03$	$5.719\mathrm{E}-02$	$4.064\mathrm{E}-03$	$5.232\mathrm{E}-03$
78	390	$3.442\mathrm{E}-02$	$1.071\mathrm{E}-03$	$4.533\mathrm{E}-02$	$2.421\mathrm{E}-03$	$2.784\mathrm{E}-03$

$$(4.2.11)$$

Table 4.11: This table shows the numerical values of the parameters of interest against different values of Re_τ, having fixed $\theta = 0.8$ and $\epsilon = 0.2$ (*inline* configuration and *spanwise* inclusions). Data are plotted in 3.2.11.

ϵRe_τ	Re_τ	λ_x	$\mathcal{K}_{xy}^{itf}$	λ_z	$\mathcal{K}_{zy}^{itf}$	$\mathcal{K}_{yy}$
0	0	$6.010E-02$	$4.113E-03$	$1.130E-01$	$2.638E-02$	$3.970E-02$
39	193	$4.413E-02$	$2.282E-03$	$6.385E-02$	$5.579E-03$	$9.572E-03$
78	390	$3.721E-02$	$1.392E-03$	$4.977E-02$	$2.973E-03$	$5.078E-03$

$$(4.2.12)$$

Table 4.12: This table shows the numerical values of the parameters of interest against different values of Re_τ, having fixed $\theta = 0.9$ and $\epsilon = 0.2$ (*inline* configuration and *spanwise* inclusions). Data are plotted in 3.2.11.

ϵRe_τ	Re_τ	λ_x	$\mathcal{K}_{xy}^{itf}$	λ_z	$\mathcal{K}_{zy}^{itf}$	$\mathcal{K}_{yy}$
0	0	$8.912E-02$	$2.960E-02$	$1.953E-01$	$1.075E-01$	$1.255E-01$
39	193	$5.788E-02$	$1.165E-02$	$9.177E-02$	$3.028E-02$	$3.373E-02$
78	390	$4.590E-02$	$5.925E-03$	$6.608E-02$	$1.554E-02$	$1.880E-02$

$$(4.2.13)$$

Table 4.13: This table shows the numerical values of the parameters of interest against different values of Re_τ, having fixed $\theta = 0.99$ and $\epsilon = 0.2$ (*inline* configuration and *spanwise* inclusions). Data are plotted in 3.2.11.

ϵRe_τ	Re_τ	λ_x	λ_z	$\mathcal{K}_{yy}$	$\mathcal{K}_{xy}^{itf}$	$\mathcal{K}_{zy}^{itf}$
0	0	$6.901E-02$	$4.521E-02$	$1.871E-03$	$5.588E-03$	$2.226E-03$
36	180	$6.901E-02$	$4.521E-02$	$1.871E-03$	$5.588E-03$	$2.226E-03$
44	222	$6.901E-02$	$4.521E-02$	$1.871E-03$	$5.588E-03$	$2.226E-03$
53	264	$6.901E-02$	$4.521E-02$	$1.871E-03$	$5.588E-03$	$2.226E-03$

$$(4.2.14)$$

Table 4.14: This table shows the numerical values of the parameters of interest against different values of Re_τ, having fixed $\theta = 0.5$ and $\epsilon = 0.2$ (*inline* configuration and *streamwise* inclusions). Data are plotted in 3.2.13. This table tells us that, in this streamwise configuration, the parameters are ϵRe_τ independent. Furthermore, streamwise parameters are directly available from the Stokes' spanwise ones by performing the following operations: $f_x|_{\text{stream, }\forall \epsilon Re_\tau} \approx f_z|_{\text{span, }Re_\tau=0}$ (and *viceversa* for the z component), where $f_i = \lambda_i, \mathcal{K}_{iy}^{itf}$ (for $i = x, z$), and $\mathcal{K}_{yy}|_{\text{stream, }\forall \epsilon Re_\tau} \approx \mathcal{K}_{yy}|_{\text{span, }Re_\tau=0}$.

Bibliography

[1] E. Alinovi. *Modeling the flow over superhydrophobic and liquid-impregnated surfaces.* Università degli Studi di Genova, 2018. URL: https://iris.unige.it/handle/11567/929101.

[2] E. Alinovi and A. Bottaro. "A boundary element method for Stokes flows with interfaces". In: *Journal of Computational Physics, 356, 261-281* (2018). DOI: 10.1016/j.jcp.2017.12.004.

[3] E. Alinovi, M. Gribaudo, and A. Bottaro. "Fractal riblets". In: *AIAA J. 56, 2108-2112* (2018). DOI: 10.2514/1.J056985.

[4] I. Babuska. "Homogenization and its application. Mathematical and computational problems". In: *Numerical Solution of Partial Differential Equations – III SYNSPADE 1975 (ed. B. Hubbard), pp. 89–116. Academic Press* (1976). DOI: 10.1016/B978-0-12-358503-5.50009-9.

[5] G. Beavers and D. Joseph. "Boundary conditions at a naturally permeable wall". In: *Journal of Fluid Mechanics* 30 (1967), pp. 197–207. DOI: 10.1017/S0022112067001375.

[6] D. Bechert et al. "Experiments on drag-reducing surfaces and their optimization with an adjustable geometry". In: *J. Fluid Mech. 338, 59-87* (1997). DOI: 10.1017/S0022112096004673.

[7] A. Bottaro. "Flow over natural or engineered surfaces: an adjoint homogenization perspective". In: *Journal of Fluid Mechanics* 877, P1 (2019), pp. 1–91. DOI: 10.1017/jfm.2019.607.

[8] M. Bruse et al. "Experiments with conventional and with novel adjustable drag-reducing surfaces". In: *Proceedings of the International Conference on Near-Wall Turbulent Flows pp. 719-738* (1993).

[9] A. Chavarin et al. "Resolvent-based prediction for turbulent flow over anisotropic permeable substrates". In: *Journal of Fluid Mechanics* 913, A24 (2021). DOI: 10.1017/jfm.2020.1169.

[10] X. Chu et al. "Transport of Turbulence Across Permeable Interface in a Turbulent Channel Flow: Interface-Resolved Direct Numerical Simulation". In: *Transport in Porous Media 136, 165–189* (2021). DOI: 10.1007/s11242-020-01506-w.

[11] S. Endrikat. *Effects of riblet shape on drag reduction in turbulent flow.* University of Melbourne, 2020. URL: http://hdl.handle.net/11343/258555.

[12] S. Endrikat, D. Modesti, et al. "Influence of riblet shapes on the occurrence of Kelvin–Helmholtz rollers". In: *Journal of Fluid Mechanics* 913, A37 (2021), pp. 1–34. DOI: 10.1017/jfm.2021.2.

[13] S. Endrikat, D. Modesti, et al. "Numerical Simulations of Turbulent Flow Over Various Riblet Shapes in Minimal-Span Channels". In: *Flow Turbulence Combust* (2020). DOI: 10.1007/s10494-020-00224-z.

[14] R. Garcìa-Mayoral and J. Jiménez. "Hydrodynamic stability and breakdown of the viscous regime over riblets". In: *J. Fluid Mech. 678, 317-347* (2011). DOI: 10.1017/jfm.2011.114.

[15] G. Gòmez-de-Segura and R. Garcìa-Mayoral. "Turbulent drag reduction by anisotropic permeable substrates - analysis and direct numerical simulations". In: *Journal of Fluid Mechanics, 875, 124172* (2019). DOI: 10.1017/jfm.2019.482.

[16] J. Guerrero. *Slides of the course "Turbulence and CFD Models".* University of Genoa, 2021. URL: http://www.dicat.unige.it/guerrero/turbulence2020/lectures.html.

[17] M. Kozuka, Y. Seki, and H. Kawamura. "DNS of turbulent heat transfer in a channel flow with a high spatial resolution". In: *International Journal of Heat and Fluid Flow, 30 (3), 514-524* (2009). DOI: 10.1016/j.ijheatfluidflow.2009.02.023.

[18] P. Luchini, F. Manzo, and A. Pozzi. "Resistance of a grooved surface to parallel flow and cross-flow". In: *Journal of Fluid Mechanics* 228 (1991), pp. 87–109. DOI: 10.1017/S0022112091002641.

[19] N. Luminari. *Modeling and simulation of flows over and through fibrous porous media.* Université de Toulouse, 2018. URL: https://oatao.univ-toulouse.fr/20132/.

[20] J. C. Maxwell. "On stresses in rarefied gases arising from inequalities of temperature". In: *Phil. Trans. R. Soc. Lond. A 170, 231–256* (1879). DOI: 10.1098/rstl.1879.0067.

[21] B. J. McKeon. "The engine behind (wall) turbulence: perspectives on scale interactions". In: *Journal of Fluid Mechanics 817, P1* (2017). DOI: 10.1017/jfm.2017.115.

[22] B. J. McKeon and A. S. Sharma. "A critical-layer framework for turbulent pipe flow". In: *Journal of Fluid Mechanics 658, 336382* (2010). DOI: 10.1017/S002211201000176X.

[23] S. B. Naqvi and A. Bottaro. "Interfacial conditions between a free-fluid region and a porous medium". In: *International Journal of Multiphase Flow, 144, 103585* (2021). DOI: 10.1016/j.ijmultiphaseflow.2021.103585.

[24] C. L. M. H. Navier. "Mémoire sur les lois du mouvement des fluides". In: *Mem. Acad. R. Sci. Inst. Fr.* (1823).

[25] M. Pauthenet. *Macroscopic model and numerical simulation of elastic canopy.* Université de Toulouse, 2018. URL: https://oatao.univ-toulouse.fr/21390/.

[26] P.G. Saffman. "Boundary conditions at a naturally permeable wall". In: *Studies in Applied Mathematics* 50 (1971), pp. 93–101. DOI: 10.1002/sapm197150293.

[27] G. I. Taylor. "Stability of a viscous liquid contained between two rotating cylinders". In: *Phil. Trans. R. Soc. Lond. A 223, 289–343* (1923). DOI: 10.1098/rsta.1923.0008.

[28] M. Walsh. "Turbulent boundary layer drag reduction using riblets". In: *20th Aerospace Sciences Meeting, AIAA Paper 1982-169* (1982). DOI: 10.2514/6.1982-169.

[29] G. A. Zampogna. *Homogenized-based modeling of flows over and through poroelastic media.* Università degli Studi di Genova, 2018. URL: http://www.dicat.unige.it/bottaro/Presentation%5C%20group/tesi_zampognaG5.pdf.

[30] H. Zhou et al. "Experimental Investigations of the Turbulent Boundary Layer for Biomimetic Surface with Spine-Covered Protrusion Inspired by Pufferfish Skin". In: *Arabian Journal for Science and Engineering* 46 (2021), pp. 2865–2875. DOI: 10.1007/s13369-020-05235-6.